ABSTRACT

INTEGRATION OF ELECTRONIC AND OPTICAL TECHNIQUES IN THE DESIGN AND FABRICATION OF PRESSURE SENSORS

by
Ivan Padron

Since the introduction of micro-electro-mechanical systems fabrication methods, piezoresistive pressure sensors have become the more popular pressure transducers. They dominate pressure sensor commercialization due to their high performance, stability and repeatability. However, increasing demand for harsh environment sensing devices has made sensors based on Fabry-Perot interferometry the more promising optical pressure sensors due to their high degree of sensitivity, small size, high temperature performance, versatility, and improved immunity to environmental noise and interference. The work presented in this dissertation comprises the design, fabrication, and testing of sensors that fuse these two pressure sensing technologies into one integrated unit. A key innovation is introduction of a silicon diaphragm with a center rigid body (or boss), denoted as an embossed diaphragm, that acts as the sensing element for both the electronic and optical parts of the sensor.

Physical principles of piezoresistivity and Fabry-Perot interferometry were applied in designing an integrated sensor and in determining analytic models for the respective electronic and optical outputs. Several test pressure sensors were produced and their performance was evaluated by collecting response and noise data. Diaphragm deflection under applied pressure was detected electronically using the principle of piezoresistivity and optically using Fabry-Perot interferometry. The electronic part of the sensor contained four p-type silicon piezoresistors that were set into the diaphragm. They

were connected in a Wheatstone bridge configuration for detecting strain-dependent changes in resistance induced by diaphragm deflection. In the optical part of the sensor, an optical cavity was formed between the embossed surface of the diaphragm and the end face of a single mode optical fiber. An infrared laser operating at 1.55 μm was used for optical excitation. Deflection of the diaphragm, which causes the length of the optical cavity to change, was detected by Fabry-Perot interference in the reflected light. Data collected on several sensors fabricated for this dissertation were shown to validate the theoretical models. In particular, the principle of operation of a Fabry-Perot interferometer as a mechanism for pressure sensing was demonstrated.

The physical characteristics and behavior of the embossed diaphragm facilitated the integration of the electronic and optical approaches because the embossed diaphragm remained flat under diaphragm deflection. Consequently, it made the electronic sensor respond more linearly to applied pressure. Further, it eliminated a fundamental deficiency of previous applications of Fabry-Perot methods, which suffered from non-parallelism between the two cavity surfaces (diaphragm and fiber), owing to diaphragm curvature after pressure was applied. It also permitted the sensor to be less sensitive to lateral misalignment during the fabrication process and considerably reduced back pressure, which otherwise reduced the sensitivity of the sensor. As an integrated sensor, it offered two independent outputs in one sensor and therefore the capability for measurements of: (a) static and dynamic pressures simultaneously, and (b) two different physical quantities such as temperature and pressure.

INTEGRATION OF ELECTRONIC AND OPTICAL TECHNIQUES IN THE DESIGN AND FABRICATION OF PRESSURE SENSORS

by
Ivan Padron

A Dissertation
Submitted to the Faculty of
New Jersey Institute of Technology and Rutgers,
The State University of New Jersey–Newark
in Partial Fulfillment of the Requirements for the Degree of
Doctor of Philosophy in Applied Physics
Federated Physics Department

January 2010

APROVAL PAGE

INTEGRATION OF ELECTRONIC AND OPTICAL TECHNIQUES IN THE DESIGN AND FABRICATION OF PRESSURE SENSORS

Ivan Padron

Dr. N.M. Ravindra, Dissertation Co-Advisor
Professor and Chair of Physics, NJIT
Date

Dr. Anthony Fiory, Dissertation Co-Advisor
Research Professor of Physics, NJIT
Date

Dr. Michael R. Booty, Committee Member
Professor of Mathematical Sciences, NJIT
Date

Dr. Tao Zhou, Committee Member
Assistant Professor of Physics, NJIT
Date

Dr. Trevor A. Tyson, Committee Member
Professor of Physics, NJIT
Date

Dr. Zhen Wu, Committee Member
Professor of Physics, Rutgers-Newark
Date

BIOGRAPHICAL SKETCH

Author: Ivan Padron

Degree: Doctor of Philosophy

Date: January 2010

Undergraduate and Graduate Education:

- Doctor of Philosophy in Applied Physics,
  New Jersey Institute of Technology and Rutgers, The State University of New
  Jersey, Newark, NJ, 2010

- Bachelor of Science in Physics
  University of Havana, Havana, Cuba, 1993

Major: Physics

Patents:

Ken Chin, Guanhua Feng, Ivan Padron, Harry Roman, "MEMS Fiber Optic Microphone"
United States Patent 7,561,277, July 14, 2009.

Ken Chin, Guanhua Feng, Ivan Padron, Harry Roman, "Aligned Embossed Diaphragm
Based Fiber Optic Sensor" United States Patent Application 20080075404, May 27,
2008. United States Patent Application 20090086214, April 2, 2009.

Ivan Padron, Anthony Fiory and Nuggehalli Ravindra, "Integrated Electronic and Optical
MEMS Based Sensor" NJIT Case number 07-068.

Ivan Padron, Anthony Fiory and Nuggehalli Ravindra, "Fabry-Perot Sensor to Measure
and detect magnetic fields" NJIT case number 10-011

N.M. Ravindra, Arun Ramadas, Ivan Padron, Rene D. Rivero, Anthony T. Fiory.
"Magnetic Wheel Energy Recycling Turbine" NJIT case number 09-041.

N.M. Ravindra, Arun Ramadas, Ivan Padron, Rene D. Rivero, Anthony T. Fiory.
"Magnetic Turbine" NJIT case number 09-068.

Presentations:

The Fifth Annual GSA Research Day. NJIT, Newark NJ. Poster Presentation. "A Novel MEMS Fabry-Perot Interferometric Pressure Sensor," *November 11, 2009.*

Materials Science & Technology 2009 Conference & Exhibition. Pittsburgh PA. Oral Presentation. "Introduction of Embossed Diaphragm as Sensing Element of an Integrated Optical and Electronic Sensor," *October 25-29, 2009.*

THERMEC 2009. International Conference on Processing Manufacturing of Advanced Materials. Technical University-Berlin, Germany. Poster Presentation. "Integrated Optical and Electronic Thin-Film Nanometric Sensors," *August 25-29, 2009.*

2009 TMS Annual Meeting & Exhibition. San Francisco, CA. Oral Presentation. "An Integrated Optical and Electronic Method to Measure Nano-deflections in a Silicon Diaphragm," *February. 15-19, 2009.*

Materials Science & Technology 2008 Conference & Exhibition. Pittsburgh PA. Oral Presentation "A Novel MEMS Fabry-Perot Interferometric Pressure Sensor," *October 7-9, 2008.*

2008 TMS Annual Meeting & Exhibition, New Orleans, LA. Oral Presentation "A Fabry-Perot Interferometric Pressure Sensor with Alignment Tolerance and High Temperature Performance," *March 9-13, 2008*

2008 APS March Meeting, New Orleans, LA. Oral Presentation "Experimental Studies of Alignment Tolerance of a Fabry-Perot Interferometric Pressure Sensor," *March 9-13, 2008.*

11th Annual CUNY Conference in Science & Engineering, CUNY, NY. Poster Presentation "A Fabry-Perot Interferometric Pressure Sensor with Alignment Tolerance and High Temperature Performance," *February 25-26, 2008.*

Publications:

Ivan Padron, Anthony T. Fiory and Nuggehalli M. Ravindra, "Novel MEMS Fabry-Perot Interferometric Pressure Sensors," Materials Science Forum, Vols. 638-642, pp. 1009-1014 (Trans Tech Publications, Switzerland, 2010).

Rene D. Rivero, Ivan Padron, Michael R. Booty, Anthony T. Fiory and N. M. Ravindra, "Indirect Template Method of Magnetic Field Assisted Assembly," Advanced Materials Research, Vols. 89-91, pp. 431-436 (Trans Tech Publications, Switzerland, 2010).

Ivan Padron, Anthony Fiory and Nuggehalli Ravindra, "Introduction of Embossed Diaphragm as Sensing Element of an Integrated Optical and Electronic Sensor," Proceedings of the Materials Science and Technology Conference. Pittsburgh, PA (2009).

N. M. Ravindra, Sushil K. Sikha and Ivan Padron, "Physics of Baseball Bats - An Analysis," International Journal of Sports Science and Engineering Vol. 3, No. 1, pp. 034-042 (2009).

Ivan Padron, Anthony T. Fiory and N. M. Ravindra, "Modeling and Design of an Embossed Diaphragm Fabry-Perot Pressure Sensor," Proceedings of the Materials Science and Technology Conference. Pittsburgh, PA (2008).

Nuggehalli M. Ravindra, Camelia Prodan, Shanmugamurthy Fnu, Ivan Padron, and Sushil K. Sikha, "Advances in the Manufacturing, Types, and Applications of biosensors," JOM – Journal of Materials, Vol. 59, No.12, pp. 37-49 (2007).

Y. Sun, G. Feng, G. Georgiou, I. Padron, E. Niver, K. Noe and K. K. Chin, "Fabry-Perot Diaphragm Fiber Optical Sensor (DFOS) for Acoustic Detection," Proceedings of the Nanotech, Vol. 3. NSIT Nanotech, The Nanotechnology Conference and Tradeshow. Santa Clara, CA (2007).

I dedicate this achievement to my lovely Family:
Jonathan, Sebastian and Elisandra Padron

Thank you for your Love and Patience
I love you.

Gracias por su Amor y Paciencia
Los Amo

ACKNOWLEDGMENTS

TABLE OF CONTENTS

LIST OF TABLES

LIST OF FIGURES

LIST OF FIGURES
(continued)

Figure   **Page**

CHAPTER 1

INTRODUCTION

As is well known, a sensor is a device that is designed to respond to a physical or chemical stimulus, such as heat, electromagnetic field, particles, smell, sound, pressure, magnetic fields, or a particular motion, and transmits a resulting impulse for interpretation or measurement or for operating a control. The main characteristic of a sensor is the conversion of energy from one form to another. The topic of this dissertation relates to sensors for measurement of pressure in partial vacuum, fluids or gasses.

1.1 Motivation

Sensors play an essential role in our lives. They have been a fundamental component in the progress of our society. One of the successful approaches for fabricating pressure sensors is the utilization of micro-electro-mechanical systems (MEMS) technology [1]. The ability to use MEMS for mass production of high performance sensors at low cost has opened a wide range of applications for pressure sensors, which include automotive, aerospace, marine, instrumentation and industrial process control, hydraulic systems, microphones, bioscience and medical applications [2].

Since the introduction of MEMS fabrication methods, piezoresistive pressure sensors have become the more common pressure transducers which dominate the pressure sensor industry due to their high performance, stability and repeatability.

Recent market trends indicate an increase in demand for pressure sensors in hazardous environments, high temperatures and biomedical applications. Many

application requirements involve small size, high performance characteristics, environmental restriction and material choices. Of the various types of sensing mechanisms used for pressure measurements, optical pressure sensors provide capability for small sizes, immunity to harsh environments, ease in remote operation and availability of integration techniques with other devices. It is particularly important that optical sensors are immune to electromagnetic wave interference, to chemical attack, and high temperatures while, at the same time, the sensors can be fabricated in small sizes.

Among the various optical techniques available for pressure sensors, Fabry-Perot interferometry [3] is selected for investigation in this dissertation, because of its advantages and attributes such as high degree of sensitivity, high accuracy, and immunity to electromagnetic interference, small size, high temperature performance, versatility, improved immunity to environmental noise, and survivability in harsh environment.

The introduction of the center rigid body diaphragm (referred to as an embossed diaphragm) in the sensor that has been developed in this dissertation gives it considerable advantages when compared with prior work on Fabry-Perot diaphragm based sensors [4, 5]. Further, significant advantages include: elimination of the non-parallelism between the two surfaces under applied external load; considerable reduction in the back pressure effects, avoidance of diaphragm-fiber optical misalignment during the fabrication process, creation of very small Fabry-Perot cavities, and integration of independent detection principles. In this dissertation, the two independent detection principles, i.e., piezoresistivity and Fabry-Perot interferometry, are combined in a single integrated device.

1.2   Dissertation Objective and Organization

The objective of this project is to combine the more established electronic (piezoresistive) method with the more promising optical (Fabry-Perot) approach in pressure sensor technology, which entails the design and fabrication of a novel integrated electronic and optical pressure sensor. The sensing element that is used for both parts of the integrated sensor is a common silicon embossed diaphragm, which deflects in the presence of an external pressure and produces an output proportional to that pressure. The embossed diaphragm is fabricated following standard MEMS processing techniques.

Chapter Two presents a historical overview of pressure measurements. It includes basic definitions related to pressure, types of pressure measurements, discussion of the influence of factors such as static and dynamic effects, as well as an historical perspective on pressure measuring instruments. Also, it includes a general description of the current practice in pressure measurement instruments, with emphasis on principles of operation and range of pressure measurements.

Chapter Three covers current diaphragm based pressure sensor technologies, and a discussion of the basic diaphragm theory with an emphasis on the mechanical behavior of the embossed diaphragm. The analysis and discussion include theoretical properties of various diaphragms fabricated in silicon. This chapter also describes the commonly used scientific terminologies in pressure sensor characterization. The concluding section is a general description of the fabrication processes and techniques for the silicon diaphragm.

Chapter Four is a review of the theory and fabrication of piezoresistive pressure sensors. A general overview of the various designs and techniques used in the fabrication

of piezoresistive sensors is presented. It includes a discussion of piezoresistivity in silicon and the use of silicon piezoresitors in silicon membrane.

Chapter Five presents an analysis of Fabry-Perot interferometry with emphasis on its application to pressure sensing devices. The theory of the working principle of a Fabry-Perot interferometer as applied to describe the response of a pressure sensor is described. An analysis of the various approaches that are utilized in the fabrication of a Fabry-Perot sensor is included, as well as the wide range of possible applications of the sensor.

Chapter Six introduces the integrated electronic and optical sensor, including the design, fabrication and the experimental data analysis. The data are shown to validate theoretical models of electronic and optical part of the sensor. The advantages of the introduction of the embossed diaphragm as well as the integration of the electronic and optical approaches are discussed.

Chapter Seven presents the conclusions and steps that are required to develop practical instrumentation based on this novel integrated piezoresistive and Fabry-Perot pressure sensor.

CHAPTER 2

PHYSICAL PRINCIPLES OF PRESSURE MEASUREMENTS

Physical movement is intrinsically related to nature, which is the result of actions and interactions of a variety of forces. No measurement has been more essential to human activity than the measurement of force in its many manifestations, including, pressure, weight, acceleration, torque, work, and energy [6].

2.1   Historical Overview

A review of the literature relating to the history of pressure and its measurements highlighting the key dates is presented [6-8]. It should be noted here that this section is primarily cited from an article by Coope [7].

1594: Galileo Galilei, of Pisa, Italy, obtained a patent for a machine to pump water from a river for the irrigation of land. The heart of the pump was a syringe. He found that 10 meters was the limit to which the water would rise in the suction pump, but had no explanation for this phenomenon. He attributed this limit to the force of the vacuum. The Galilean analysis provided the foundation from which many later philosophers (especially Berti, Magiotti, Magni and Torricelli) set off to make their discoveries of atmospheric pressure and the real possibility of producing vacuum in nature. In this sense, even though Galileo was far away from completely understanding the role of the atmospheric pressure in pneumatic phenomena, his theses provided an essential starting point, both at the strictly theoretical level and the methodology, for working out the conceptual apparatus of the modern science of vacuum.

1644: Evangelista Torricelli invented the mercury barometer. The Italian physicist filled a tube one meter long, hermetically closed at one end, with mercury and set it vertically with the open end in a basin of mercury. The column of mercury invariably fell to about 760 mm, leaving an empty space above its level. Torricelli realized that the atmosphere exerted a pressure on the earth which maintained the mercury column in equilibrium. Incidentally, by inverting the filled mercury tube, he concluded that the space on top of the tube is empty, that nothing is in there and called it a "vacuum".

1648: Blaise Pascal, a French philosopher, physicist and mathematician, heard about the experiments of Torricelli and was searching for the reasons of the findings of Galileo and Torricelli. He came to the conviction that the force, which keeps the column at 760 mm, is the weight of the air above. Thus, on a mountain, the force must be reduced by the weight of the air between the valley and the mountain. He predicted that the height of the column would decrease which he proved with his experiments at the mountain, Puy de Dome, in central France. From the decrease, he could calculate the weight of the air. Pascal also formulated that this force, he called it "pressure", is acting uniformly in all directions. He named the mercury-under-vacuum instrument that was used to sense atmospheric pressure the *barometer*.

1656: Offo von Guericke, born in Magdeburg, Germany, developed new air pumps to evacuate larger volumes and staged a dramatic experiment in Magdeburg by pumping the air out of two metal hemispheres which had been fitted together with nothing more than grease. Eight horses at each hemisphere were not strong enough to separate them.

1661: Robert Boyle, an Anglo-Irish chemist, used J-shaped tubes closed at one end to study the relationship between the pressure and volume of trapped gas and stated the relation (Boyles's Law), "The product of the measures of pressure and volume is constant for a given mass of air at fixed temperature", i.e. $P \times V = K$ (P: Pressure, V: Volume, K: Constant) which means that if the volume of a gas at a given pressure is known, the pressure can be calculated if the volume is changed, provided that neither the temperature nor the amount of gas is changed. He was the first to use the word *barometer* in print.

1738: Daniel Bernoulli, a Dutch Swiss mathematician, attempted to formulate a kinetic theory of gases that explains macroscopic properties of gases, such as pressure, temperature, or volume, by considering their molecular composition and motion, and use it to explain Boyle's law. He developed the impact theory of gas pressure to the point where Boyle's law could be deduced analytically. He also anticipated the Charles-Gay-Lussac law by stating that pressure is increased by heating a gas at constant volume.

1820: Almost 200 years later, Joseph Louis Gay-Lussac, a French physicist and chemist, detected that the pressure increase of a trapped gas at constant volume is proportional to the temperature (Gay Lussac law). Twenty years later, William Thomson (Lord Kelvin) defined the absolute temperature.

1843: Lucien Vidie, a Frenchman, invented the barograph, a recording aneroid barometer (instrument used to measure atmospheric pressure). It produces a paper or foil chart called a barogram that records the barometric pressure over time.

1847-1859: In rapid succession, James Prescott Joule, Rudolf Clausius, and James Clerk Maxwell developed the kinetic theory of gas pressure in which pressure is

viewed as a measure of the total kinetic energy of the molecules:

$$p = \frac{2KE}{3V} = \frac{1}{3}\rho C^2 = NRT \,.$$

1849: Eugène Bourdon of France, a watchmaker and an engineer, invented the Bourdon gauge, a pressure measuring instrument that is still in use today. A Bourdon gauge uses a coiled tube, which, as it expands due to pressure increase causes a rotation of an arm connected to the tube. It could measure pressures up to 100,000 psi (690 MPa), something that had previously been impossible.

1874: H. G. McLeod invented the McLeod gauge instrument to measure very low pressures, down to 10^{-6} Torr. McLeod gauges operate by taking in a sample volume of gas from a vacuum chamber, and then compressing it by tilting, and filling with mercury. The pressure in this smaller volume is then measured by a mercury manometer, and, by knowing the compression ratio, the pressure of the original vacuum can be determined.

1906: Marcelo Pirani, a German, developed a new type of vacuum gauge, the Pirani vacuum gauge. It is based on measuring the pressure dependence of heat loss from a hot wire by heat transfer to the surrounding gas and walls. In particular, it employs the change in resistivity of the heated wire (in Pirani's original work consisting of tantalum and platinum; today, tungsten, platinum or nickel is commonly used) with temperature to determine the heat loss.

1927: Fans Michel Penning, a Dutch physicist, invented a type of cold cathode vacuum gauge, known as Penning gauge. A cold cathode is an element used within some Nixie tubes, gas discharge lamps, gas filled tubes, and vacuum tubes. The term, "cold cathode", refers to the fact that the cathode is not independently heated. In spite of this, the cathode itself may still operate at temperatures as high as if the cathode were heated.

1930: The first pressure transducers were transduction mechanisms in which the movements of diaphragms, springs or Bourdon tubes are part of an electrical quantity. Pressure diaphragms are part of a capacitance. The indicator movement is the tip of a potentiometer needle.

1938: The bonded strain gauges were independently developed by E. E. Simmons of the California Institute of Technology and A.C. Ruge of Massachusetts Institute of Technology. Simmons was first to apply for a patent.

1955: The first foil strain gauges were made with an integrated full resistor bridge, which, if bonded on a diaphragm, see opposite stress in the center and at the edge.

1965: The bonding connection of the gauges to the diaphragm was always the cause for hysteresis and instability. In the 1960's, Statham introduced the first thin-film transducers with good stability and low hysteresis. Today, this technology is the one of the main used for high pressure measurements.

1967: Art R. Zias and John Egan at Honeywell Research Center, Minneapolis, Minnesota, applied for a patent for the edge-constrained silicon diaphragm. In 1969, Hans W. Keller applied for a patent for the batch-fabricated silicon sensor. This technology has profited from the enormous progresses in integrated circuit (IC) technology. A modern sensor typically weighs 0.01 grams. If all non-crystalline diaphragms have inherent hysteresis, the precision limit of this is not detectable by today's means.

1973: William R. Poyle applied for a patent for capacitive transducers on glass or quartz basis; Bob Bell of Kavlico applied for a patent based on ceramics, a few years later, in 1979. This technology filled the gap for lower pressure ranges (for which thin

film was not suited) and is today, along with resistors on ceramic diaphragms, the widely utilized technology for non-benign media.

2.2 Current Technologies

Since the introduction of MEMS, in order to satisfy the great demand for pressure sensors for innumerable applications, many groups have been working to develop high performance pressure sensors following the approaches described in this section.

Capacitor pressure sensor: This is based on the change in capacitance in a parallel plate formed between a sensing diaphragm and the substrate. Diaphragm deflection due to applied pressure changes the distance between these plates and results in the change of capacitance as a function of applied pressure. It is connected to an electrical circuit, which converts the capacitance to either a voltage signal or a frequency signal.

Piezoelectric pressure sensor: This is based on the piezoelectric effect, i.e., the ability of some materials (notably crystal and certain ceramic) to generate an electric potential in response to applied mechanical stress.

Piezoresistive pressure sensor: This is based on the change in electrical resistivity that occurs with the application of mechanical stress. It is fabricated, for example by placing sensing piezoresistors in a Wheatstone bridge configuration over silicon diaphragm. This sensor can be utilized for pressure ranges from 100 mbar to 1500 bar in the absolute and differential pressure modes.

Optical pressure sensor: Techniques such as Michelson, Mach Zehnder, and Fabry-Perot interferometry have been incorporated in the fabrication of pressure sensors to meet the demand for sensors to operate in hazardous environments, high temperature conditions and biomedical applications, which involve small size, high performance characteristics, environmental restrictions and material choices.

2.3   Basic Definitions

This section is dedicated to the definitions of the basic concepts relating to pressure sensors.

2.3.1 Pressure

Pressure is the ratio of the magnitude of the force acting perpendicular to a surface to the area of that surface.

Pressure is measured in units of force divided by area: pounds per square inch (psi) in the British system of units or, in the SI system, Newton per square meter, or Pascal. In Table 2.1, the various units for pressure and the conversion factors from one unit system to another are summarized.

Mathematically,

$$P = \frac{F}{A} \tag{2.1}$$

where, P is the pressure, F is the normal force, and A is the area.

Table 2.1 Conversion Table for Common Units of Pressure

	Pascal (Pa)	Bar (bar)	Technical atmosphere (at)	Atmosphere (atm)	Torr (Torr)	Pound per square inch (psi)
1 Pa	$\equiv N/m^2$	10^{-5}	1.0197×10^{-5}	9.8692×10^{-6}	7.5006×10^{-3}	145.04×10^{-6}
1 bar	100,000	$\equiv 10^6$ dyn/cm^2	1.0197	0.98692	750.06	14.5037744
1 at	98,066.5	0.980665	$\equiv 1$ kgf/cm^2	0.96784	735.56	14.223
1 atm	101,325	1.01325	1.0332	$\equiv 1$ atm	760	14.696
1 torr	133.322	1.3332×10^{-3}	1.3595×10^{-3}	1.3158×10^{-3}	$\equiv 1$Torr; ≈ 1 mmHg	19.337×10^{-3}
1 psi	6,894.76	68.948×10^{-3}	70.307×10^{-3}	68.046×10^{-3}	51.715	$\equiv 1$ lbf/in^2

2.3.2 Strain Gauge

Stress σ is defined as the object's internal resisting force, and strain ε is defined as the resulting displacement and deformation. It was introduced into the theory of elasticity by Cauchy around 1822 [9].

For a uniform distribution of internal resisting forces, stress can be calculated by dividing the force (F) applied by the unit area (A):

$$Stress(\sigma) = \frac{F}{A} \qquad (2.2)$$

Strain is defined as the amount of deformation per unit length of an object when a load is applied. Strain is calculated by dividing the total deformation (ΔL) of the original length by the original length (L):

$$Strain(\varepsilon) = \frac{(\Delta L)}{L} \qquad (2.3)$$

Strain may be compressive or tensile and is typically measured by strain gauges. Fundamentally, all strain gauges are designed to convert mechanical displacement into an

electronic signal. A change in capacitance, inductance, or resistance is proportional to the strain experienced by the sensor.

When a strain is introduced, the strain sensitivity, which is also called the gauge factor (GF), is given by [10]:

$$GF = \frac{\text{relative change in resistance}}{\text{applied strain}} = \frac{\Delta R/R}{\Delta L/L} = \frac{\Delta R/R}{\varepsilon} \tag{2.4}$$

where, R is the initial resistance of the strain gauge and ΔR is the change in resistance.

For all elastic materials, there is a relationship between the stress σ (N/m^2) and strain ε. They obey Hooke's law and consequently the deformation varies linearly with applied force. The constant of proportionality is the elastic modulus or Young's modulus of the material and is given by:

$$\text{Young's modulus, } E = \frac{\text{Stress}}{\text{Strain}} = \frac{\sigma}{\varepsilon}(\text{N/m}^2) \tag{2.5}$$

The earliest strain gauges were mechanical devices that measured strain by measuring the change in length and comparing it to the original length of the object.

2.3.3 Types of Pressure Measurements

One of the basic limitations of all measurement science, or metrology, is that all measurements are relative. All measurements contain a reference point against which the quantity to be measured must be compared. In terms of this reference point, pressure can be divided into four categories (Figure 2.1) [10, 11]:

1. *Absolute pressure*: It measures the pressure relative to perfect vacuum pressure (zero pressure). Atmospheric pressure is 101.325 kPa (14.7 psi) at sea level with reference to vacuum.

2. *Gauge pressure*: It can be calibrated to measure the pressure relative to a given atmospheric pressure at a given location. An alternative definition of gauge pressure is the difference between absolute pressure and local atmospheric pressure. A tire pressure gauge is an example of gauge pressure indication. When the tire pressure gauge reads 0 psi, it corresponds to 14.7 psi (atmospheric pressure) in the tire. Gauge pressure can be positive or negative, depending on whether the absolute pressure is, respectively, greater than or less than the local atmospheric pressure.

3. *Differential pressure:* It measures the difference between two or more pressures introduced as inputs to the sensing unit, for example, measuring the pressure drop across an oil filter. Differential pressure is also used to measure flow or level in pressurized vessels.

4. *Sealed pressure:* It is the same as the gauge pressure sensor except that it is previously calibrated by manufacturers to measure pressure relative to sea level pressure (14.7 psi).
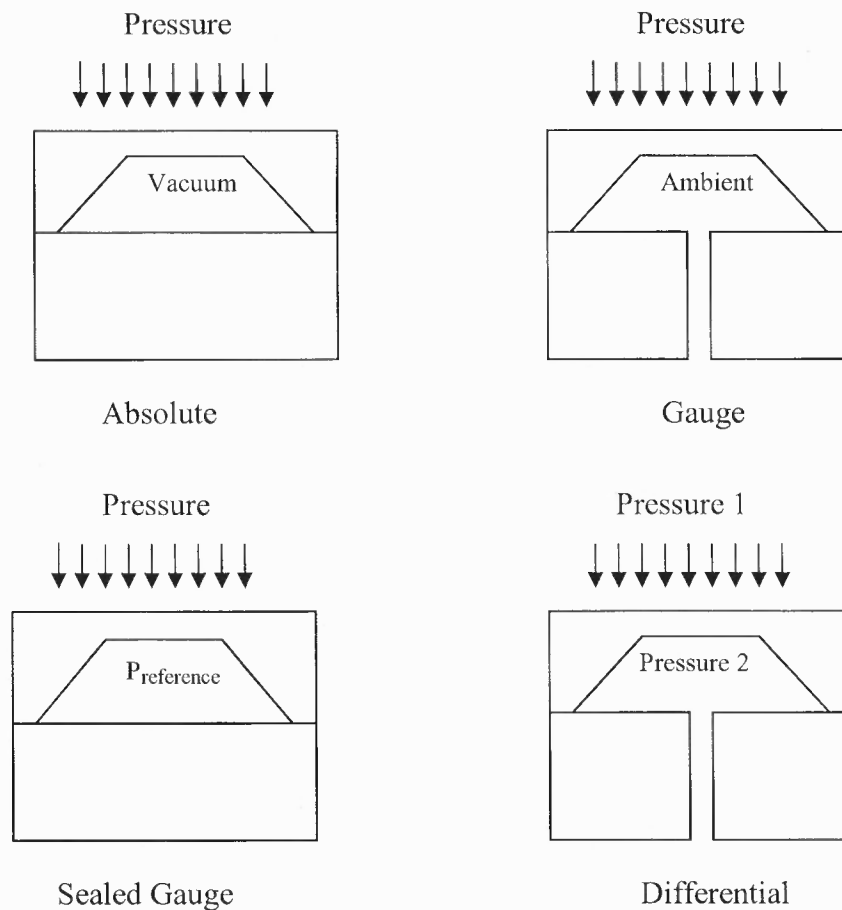
Figure 2.1 Types of pressure measurements.

Pressure is always measured relative to some reference. If the reference is absolute vacuum, the pressure is absolute pressure (e.g. psia). If the reference is local ambient pressure, the pressure is gauge pressure. If a pressure difference between two points is being measured without regard to the absolute or gauge pressure, the measurement is differential pressure (Figure 2.2) [12, 13].
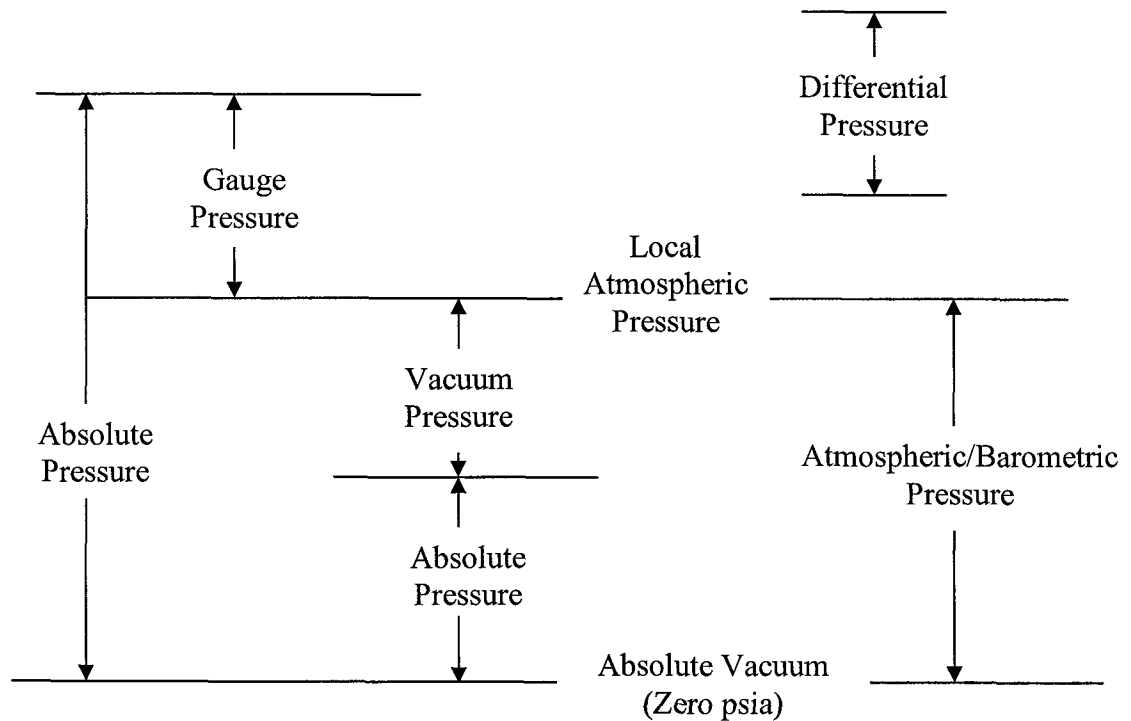
Figure 2.2 Pressure measurement relationships and definitions.

2.3.4 Static and Dynamic Pressure

The pressure measured in a static system is *static pressure*. It is uniform in all directions, so measurements are independent of direction under steady-state or equilibrium conditions.

In a dynamic system, pressure is defined using three different terms. The first pressure that can be measured is *static pressure*. This pressure is the same as the static

pressure that is measured in a static system; therefore, pressure acts equally in all directions. The second type of pressure is what is referred to as the *dynamic pressure*. This pressure term is associated with the velocity or the flow of the fluid. The third pressure is *total pressure* and is simply the sum of the static pressure and the dynamic pressure.

2.4   A Historical Perspective of Pressure Instruments

Many instruments have been invented to measure pressure, with different approaches, advantages and disadvantages [10, 14-17]. In this section, a general description of the different types of pressure measurement instruments and their principle of operation and pressure range under measurement is presented.

2.4.1 Hydrostatic Gauge

Hydrostatic gauges compare pressure to the hydrostatic force per unit area at the base of a column of fluid. Hydrostatic gauge measurements are independent of the type of gas being measured, and can be designed to have a very linear calibration. They have poor dynamic response. Simple hydrostatic gauges can measure pressures ranging from a few mm Hg (a few 100 Pa) to a few atmospheres (approximately, 10^6Pa).

Piston-type gauges

The piston-type gauges counterbalance the pressure of a fluid with a solid weight or a spring; for example, dead-weight testers that are used for calibration and tire-pressure gauges.

The gauge can be used to measure pressure in the range from 0.01 psi to upward of, 10^4 psi, in steps as small as 0.01% of range within a calibration uncertainty from 0.01 to 0.05% of the reading.

Liquid column (manometer)

Liquid column gauges consist of a vertical column of liquid in a tube whose ends are exposed to various pressures. The column will rise or fall until its weight is in equilibrium with the pressure differential between the two ends of the tube. The difference in liquid level represents the applied pressure.

The U tube manometer (Figure 2.3 [18]) consists of a transparent glass tube constructed in the form of an elongated U and partially filled with a liquid, preferably mercury for its high density (13.534 g/cm³) and low vapor pressure. The U tube manometer measures pressures in the range from 0.1 in of water to 100 psi, within a calibration uncertainty from 0.02 to 0.2 % of the reading.
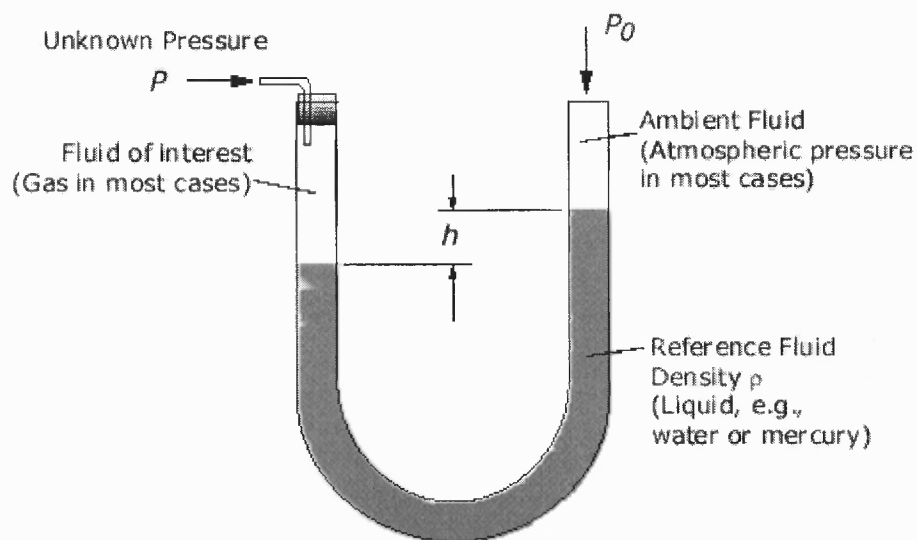
Figure 2.3 Manometers [18].

The difference in fluid height (h) in a liquid column manometer is proportional to the pressure difference. Gauge pressure $\Delta P = P - P_0 = \rho g h$.

Liquid column pressure gauges are independent of the type of gas being measured and have a highly linear calibration.
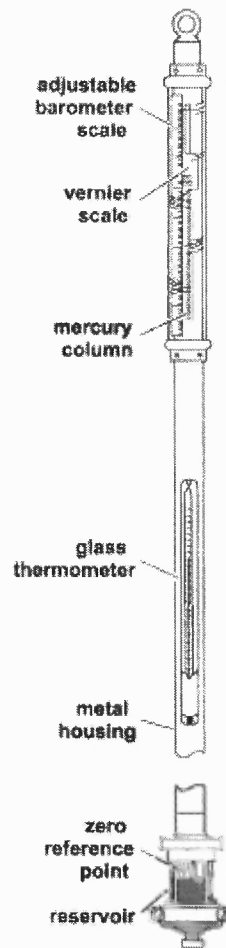
Figure 2.4 Mercury barometer [17].

A barometer is a type of monometer with one leg at zero pressure absolute. The common meteorological barometer (Figure 2.4) is a liquid-column gauge filled with mercury. The top of the column is sealed, and the bottom is open and submerged below the surface of a reservoir of mercury. The atmospheric pressure on the reservoir keeps the mercury at a height proportional to that pressure. An adjustable scale, with a vernier

scale, allows a reading of column height. Aneroid barometers using metallic diaphragm elements are usually less accurate.

McLeod gauge

A McLeod gauge isolates a sample of gas and compresses it in a modified mercury manometer until the pressure is a few mm Hg. The gas must be well-behaved during its compression (it must not condense). The technique is slow and unsuited to continuous monitoring, but is capable of good accuracy.

The McLeod gauge measures pressure in the range from 1 mm Hg above absolute Zero to about 10^{-4} mm Hg, with a calibration uncertainty of 0.5% above 10^{-3} mm Hg to about 3% at 10^{-4} mm Hg.

An important variation is the McLeod gauge which isolates a known volume of vacuum and compresses it to a height that varies with the liquid column. The McLeod gauge can measure vacuum as high as 10^{-6} mm Hg (0.1 mPa), which is the lowest direct measurement of pressure that is possible with the current technology.

2.4.2 Aneroid

Aneroid gauges are based on a pressure sensing element which flexes elastically under the effect of a pressure difference across the element. "Aneroid" means "without fluid." However, aneroid gauges can be used to measure the pressure of a liquid as well as a gas, and they are not the only type of gauge that can operate without fluid. For this reason, they are often called mechanical gauges.

The pressure sensing element may be a Bourdon tube, a diaphragm, a capsule, or a set of bellows, which will change shape in response to the pressure. The deflection of

the pressure sensing element may be read by a linkage connected to an indicating needle, or it may be read by a secondary transducer. The Secondary transducers in modern vacuum gauges commonly measure a change in capacitance with the mechanical deflection.

Bourdon

A Bourdon gauge uses as elastic element a coiled tube connected to the chamber or pipe in which pressure is to be sensed. It is fixed at one end, which is open to accept the applied pressure, but free at the other end, which is closed to allow displacement under the deforming action of the pressure difference across the tube walls.

As the gauge pressure increases, the tube will tend to uncoil, while a reduced gauge pressure will cause the tube to coil more tightly. This motion is transferred through a linkage to a gear train connected to an indicating needle. The needle is presented in front of a card face (Figure 2.5) inscribed with the pressure indications associated with particular needle deflections. In a barometer, the Bourdon tube is sealed at both ends and the absolute pressure of the ambient atmosphere is sensed.
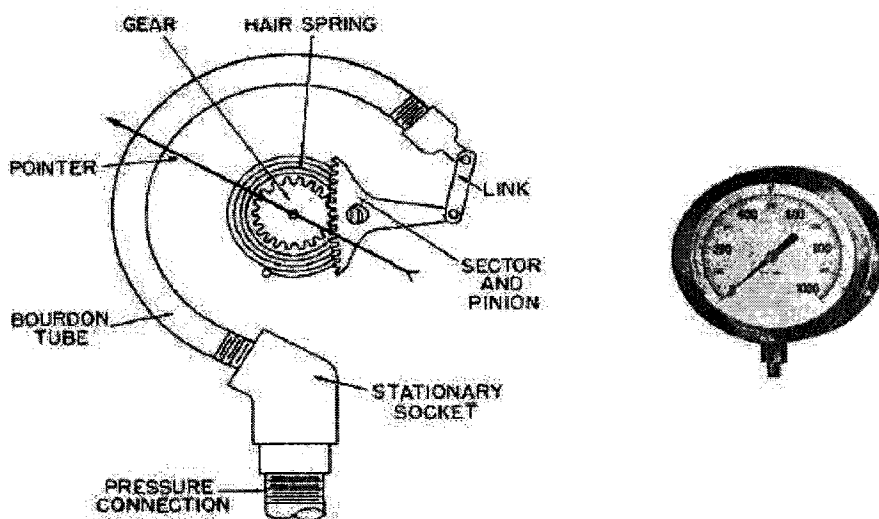
Figure 2.5 Bourdon gauge [17].

Differential Bourdon gauges use two Bourdon tubes and a mechanical linkage that compares the readings. Bourdon gauges are available for a wide range of absolute and differential pressure measurements within a calibration uncertainty of 0.1% of the reading.

Bellows

In gauges intended to sense low pressures, or require that an absolute pressure be measured, the gear train and needle may be driven by an enclosed and sealed bellows chamber. In one arrangement, pressure is applied to one side of the bellows, and the resulting deflection is partially counterbalanced by a spring. In another differential arrangement, one pressure is applied to the inside of one sealed bellows while the other pressure is conveyed to the inside of another sealed bellows.

Diaphragm

Diaphragm gauges use the deflection of a flexible membrane that separates regions of different pressure. The amount of deflection is repeatable for known pressures so that the pressure can be determined by using calibration. One side of the diaphragm is exposed to the pressure being measured, while the other side is exposed to the pressure of the atmosphere. Any increase in the pressure line moves the diaphragm upward against the spring, moving the pointer to a higher reading. When the pressure decreases, the spring moves the diaphragm downward, rotating the pointer to a lower reading. Thus, the position of the pointer is balanced between the pressure pushing the diaphragm upward and the spring action pushing down. When the gauge reads 0, the pressure in the line is equal to the outside air pressure (Figure 2.6).

Useful range: above 10^{-2} mm Hg (roughly 1 Pa)

LIGHT

CELLULOID SCALE

PIVOT BEARING

ALUMINUM POINTER

BEAD CHAIN

NEOPRENE SILK DIAPHRAGM

CALIBRATING SPRING

ZERO ADJUSTING SPRING

HOUSING

3-WAY COCK

PANEL OR BULKHEAD

ZERO ADJUSTING SCREW
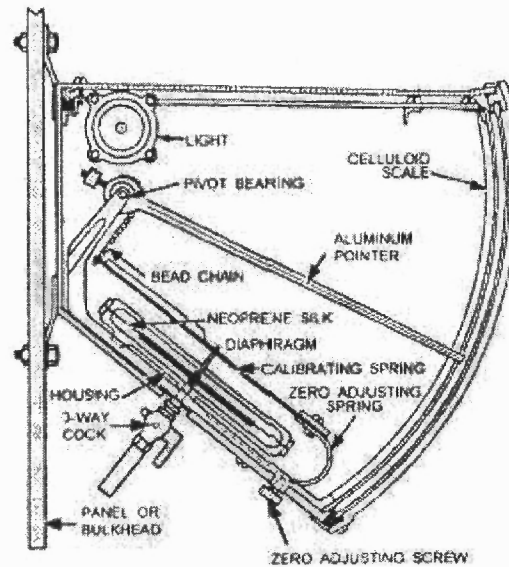
Figure 2.6 Diaphragm gauge [17].

Secondary transducer

This group includes various electronic type pressure sensors such as the resistive (strain gauge), inductive, capacitive, piezoelectric and piezoresistive. Most of them are diaphragm based sensors, which are described in detail in Chapter Three.

2.4.3   Thermal Conductivity

Thermal Conductivity gauges are based on the fact that the ability of a gas to conduct heat decreases with pressure. In this type of gauge, a wire filament is heated by running current through it. A thermocouple or Resistance Temperature Detector (RTD) can then be used to measure the temperature of the filament. This temperature is dependent on the rate at which the filament loses heat to the surrounding gas, and therefore on the thermal conductivity. A common variant is the Pirani gauge which uses a single platinum filament as both the heated element and RTD. These gauges are accurate from 10^{-3} mm

Hg to 10 mm Hg, but they are sensitive to the chemical composition of the gases being measured.

Two wire

One wire coil is used as a heater, and the other is used to measure nearby temperature due to convection.

Pirani (one wire)

A Pirani gauge consists of a metal wire open to the pressure being measured. The wire is heated by a current flowing through it and cooled by the gas surrounding it. If the gas pressure is reduced, the cooling effect will decrease; hence the equilibrium temperature of the wire will increase. The resistance of the wire is a function of its temperature: by measuring the voltage across the wire and the current flowing through it, the resistance (and so the gas pressure) can be determined.

2.4.4 Ionization Gauge

Ionization gauges are the most sensitive gauges for very low pressures (high vacuums). They sense pressure indirectly by measuring the electrically charged ions produced when the gas is bombarded with electrons. Fewer ions will be produced by lower density gases. The calibration of an ion gauge is unstable and dependent on the nature of the gases being measured, which is not always known. They can be calibrated against a McLeod gauge which is much more stable and independent of chemistry.

Thermionic emission generates electrons, which collide with gas atoms and generate positive ions. The ions are attracted to a suitably biased electrode known as the collector. The current in the collector is proportional to the rate of ionization, which is a

function of the pressure in the system. Hence, measuring the collector current gives the gas pressure. There are several sub-types of ionization gauge.

Most ion gauges come in two types: hot cathode and cold cathode. A third type exists, which is more sensitive and expensive, is known as a spinning rotor gauge. In the hot cathode version, an electrically heated filament produces an electron beam. The electrons travel through the gauge and ionize gas molecules around them. The resulting ions are collected at a negative electrode. The current depends on the number of ions, which depends on the pressure in the gauge. Hot cathode gauges are accurate from 10^{-10} mm Hg to 10^{-3} mm Hg. The principle behind cold cathode version is the same, except that electrons are produced in a discharge created by a high voltage electrical discharge. Cold cathode gauges are accurate from 10^{-2} mm Hg to 10^{-9} mm Hg.

Ionization gauge calibration is very sensitive to construction geometry, chemical composition of gases being measured, corrosion and surface deposits. Their calibration can be invalidated by activation at atmospheric pressure or low vacuum. The composition of gases at high vacuums will usually be unpredictable, so a mass spectrometer must be used in conjunction with the ionization gauge for accurate measurements.

Hot cathode

A hot cathode ionization gauge is mainly composed of three electrodes all acting as a triode, where the cathode is the filament. The three electrodes are a collector or plate, a filament, and a grid. The collector current is measured in pico-amps by an electrometer. The filament voltage to ground is usually at a potential of 30 volts while the grid voltage is 180–210 volts DC, unless there is an optional electron bombardment feature, by heating the grid which may have a high potential of approximately 565 volts. The most

common ion gauge is the hot cathode Bayard-Alpert gauge, with a small ion collector inside the grid. A glass envelope with an opening to the vacuum can surround the electrodes, but usually nude gauge is inserted in the vacuum chamber directly, the pins being fed through a ceramic plate in the wall of the chamber. Hot cathode gauges can be damaged or lose their calibration if they are exposed to atmospheric pressure or even low vacuum while hot. The measurements of a hot cathode ionization gauge are always logarithmic. Electrons emitted from the filament move several times in back and forth movements around the grid before finally entering the grid. During these movements, some electrons collide with a gaseous molecule to form a pair of an ion and an electron (electron ionization). The number of these ions is proportional to the gaseous molecule density multiplied by the electron current emitted from the filament, and these ions pour into the collector to form an ion current. Since the gaseous molecule density is proportional to the pressure, the pressure is estimated by measuring the ion current.

Cold cathode

There are two subtypes of cold cathode ionization gauges: the Penning gauge and the inverted magnetron, also called a Redhead gauge. The major difference between the two is the position of the anode with respect to the cathode. Neither has a filament, and each may require a DC potential of about 4 kV for operation. Inverted magnetrons can measure down to 10^{-12} mm Hg.

Such gauges cannot operate if the ions generated by the cathode recombine before reaching the anodes. If the mean-free path of the gas within the gauge is smaller than the gauge dimensions, then the electrode current will essentially vanish. A practical upper-bound to the detectable pressure is, for a Penning gauge, of the order of 10^{-3} mm Hg.

Similarly, cold cathode gauges may be reluctant to start at very low pressures, in that the near-absence of a gas makes it difficult to establish an electrode current. This is particularly the case in Penning gauges which use an axially symmetric magnetic field to create path lengths for ions that are of the order of meters. In ambient air, suitable ion-pairs are ubiquitously formed by cosmic radiation. In a Penning gauge, design features are used to ease the set-up of a discharge path. For example, the electrode of a Penning gauge is usually finely tapered to facilitate the field emission of electrons.

Table 2.2 summarizes the various types of pressure gauges with their respective measurement range and physical principles.

Table 2.2 Types of Pressure Gauges

Pressure Gauge Types	Measurement Range		Physical Principles
	Minimum *(order of)*	**Maximum** *(order of)*	
Hydrostatic *(Piston-Type, Manometer McLeod Gauge)*	10^{-2} Pa	10^6 Pa	Comparison of pressure to the hydrostatic force per unit area at the base of a column of fluid
Aneroid *(Bourdon, Diaphragm Bellows, Piezoelectric, Piezoresistive, Capacitive...)*	1 Pa	10^3 GPa	Sensing element which flexes elastically under the effect of a pressure difference across the element.
Thermal conductivity *(Two wire, Pirani)*	1 Pa	10^3 Pa	Based on the fact that the ability of a gas to conduct heat decreases with pressure.
Ionization gauge *(Hot and cold cathode)*	10^{-7} Pa	1 Pa	They sense pressure indirectly by measuring the ions produced when the gas is bombarded with electrons.

CHAPTER 3

DIAPHRAGM-BASED PRESSURE SENSOR

A commonly available pressure sensor is the diaphragm-based pressure transducer, in which the difference in pressure from one side of the diaphragm to the other causes diaphragm deformation. This chapter focuses on a review of the various approaches to the fabrication of diaphragm-based pressure sensors and the analysis of the diaphragm behavior. The analysis and discussions related to various types of diaphragm-based pressure sensors, presented in this chapter will be limited to silicon diaphragms. It includes the design and fabrication of the sensor.

3.1 Diaphragm-Based Pressure Sensor Technologies

Currently, the most general method of measuring pressure is to balance it against an elastic force provided by an elastic element. Diaphragms are the simplest form of mechanical structures for use as pressure sensing elements, in which the pressure is determined by the deflection of the diaphragm due to applied pressure.

Although the term MEMS, for micro-electromechanical system, is not restricted to silicon micromachining, most of today's MEMS technology is based on silicon. Silicon wafers offer a good combination of qualities such as: ideal elasticity, good heat conduction, low to intermediate electrical conductivity (depending on type and doping), low thermal expansion coefficient, and stability at high temperatures [19].

Micro-electromechanical systems technology has led to significantly new opportunities for the possibility of the fabrication of diaphragm based pressure

sensors. Low cost, low power, miniaturization, high performance and integration have been the key advantages of MEMS technology [20].

MEMS surface and bulk micromachining techniques have facilitated the fabrication of capacitive, piezoresistive and optical diaphragm based pressure sensors, which are the leading sensor types in the current pressure sensor market. These sensors have advantages and disadvantages with respect to one another as summarized in Table 3.1.

Table 3.1 Diaphragm-Based Pressure Sensors

Pressure Sensor	Advantages	Disadvantages	Physical Principles
Capacitive	- Low noise - Temperature insensitive - Environmentally robust	- Additional MEMS processing - Nonlinearity - Complex electronics - Large size	Capacitance change in a parallel plate configuration due to applied pressure
Piezoresistive	- Linearity - Stability - Repeatability - Low cost - Simple transducer circuit	-Temperature sensitive - Doping dependence of piezo coefficient - Power consumption	Change in electrical resistivity of Piezoresistors in a Wheatstone Bridge configuration placed over a diaphragm
Optical	- Small size - Immune to EMI - High sensitivity - Low cost - Temperature insensitive - Remote sensing capability	- Instability - No Repeatability - Q-point stabilization	Structures that deform under pressure and consequently produce a change in an optical signal.

3.1.1   Capacitive Pressure Sensor

Capacitance pressure sensors are based on a parallel plate configuration in which each plate is associated with an electrode with one physically fixed and the other flexible. As the distance between the two plates changes under applied pressure, the capacitance changes and it can be calibrated in relation to the applied pressure (Figure 1).
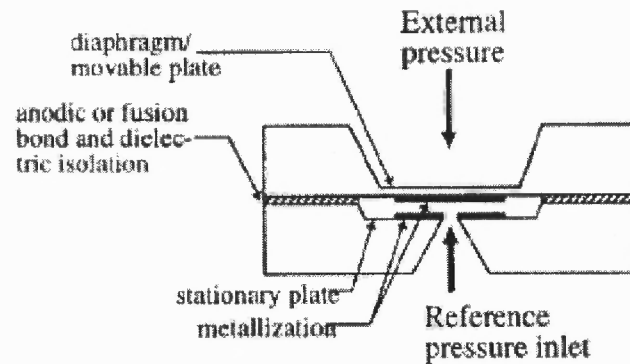
Figure 3.1 Capacitive pressure sensor [20].

Assuming parallel deflection of the diaphragm, the change in capacitance is inversely proportional to change in the gap height d, where the capacitance is given by:

$$C = \frac{\varepsilon A}{d} \tag{3.1}$$

And, where ε is the permittivity of the medium between the plates (fixed plate and diaphragm), and A is the area of overlap between the electrodes.

For a circular diaphragm sensor under deflection, the capacitance becomes:

$$C = \iint \frac{\varepsilon}{d - W(r)} r \, dr \, d\theta \tag{3.2}$$

where $W(r)$ is the deflection of the diaphragm.

Capacitance techniques are intrinsically less noisy than those based on piezoresistivity and are independent of thermal noise. However, using micromachined techniques, the values of capacitances obtained are extremely small, and additional noise from the interface electronic circuits often exceeds that of the resistance based devices. Moreover, the sensor output exhibits nonlinear behavior [10].

One of the approaches to improve linearity is to operate the capacitive sensor in contact mode using a dielectric spacer (Figure 3.2). In contact mode, the capacitance is nearly proportional to the contact area, which in turn shows good linearity with applied pressure. This is valid over a wide range of pressure. However, the linearity is gained at the expense of sensitivity [19].
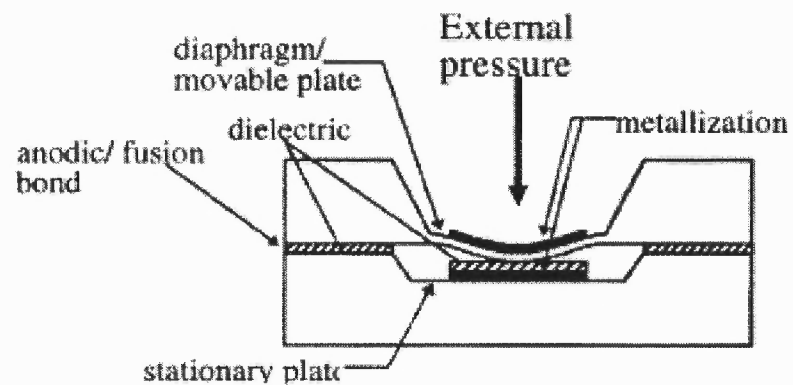
Figure 3.2 Capacitive pressure sensor operating in contact mode [19].

Another method for achieving linear response is to use a bossed diaphragm. The thicker center body (or boss) contributes to most of the capacitance of the structure and its shape does not distort considerably under applied pressure. Hence, the capacitance-pressure characteristics will be more linear.

3.1.2   Piezoresistive Pressure Sensor

The piezoresistive pressure transducers are the most commercially available pressure sensors. They are based on the piezoresistive effect, in which piezoresistors are placed over a diaphragm in a Wheatstone bridge configuration.

The use of anisotropic etching, anodic and fusion bonding, ion implanted strain gauges and micromachining techniques have led to a reduction in size and improvement in the accuracy and performance of piezoresistive silicon-based pressure sensors. Figure 3.3 illustrates an example of a piezoresistive pressure sensor.
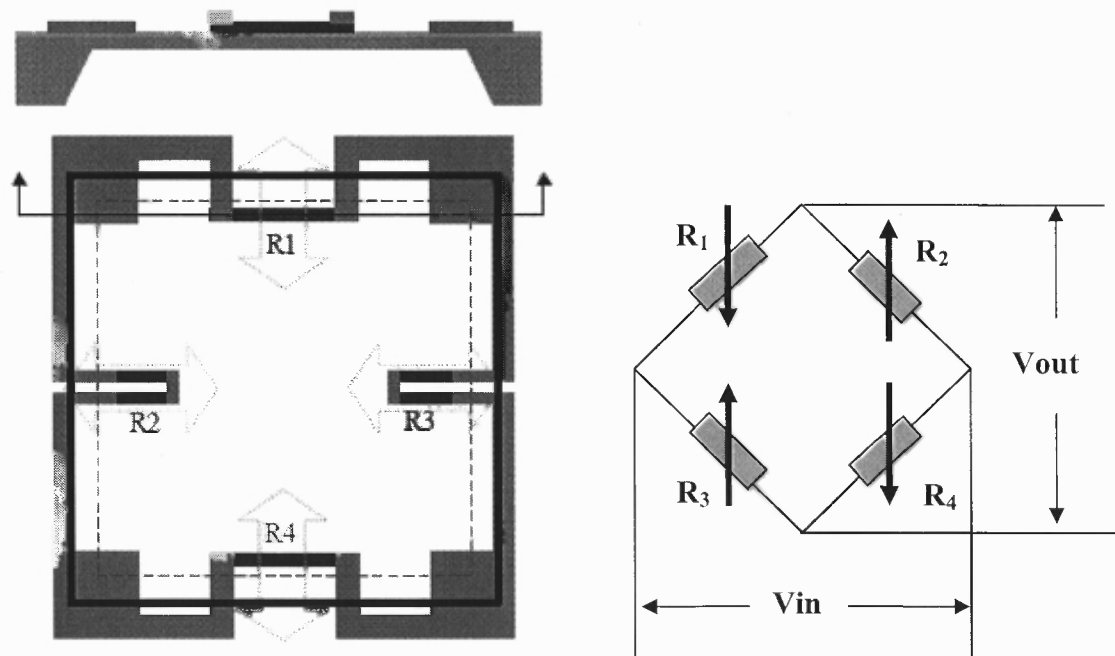
Figure 3.3 Piezoresistive pressure sensor [21].

Chapter Four is dedicated entirely to the study of the theory and application of piezoresistive pressure sensors.

3.1.3 Optical Diaphragm Based Pressure Sensors

The demand for sensors to operate in hazardous environments, high temperatures and biomedical applications has increased; as a result, there has been significant interest in the design and fabrication of optical sensors.

Optical pressure sensors typically utilize a structure that deforms under pressure and consequently produces a change in an optical signal. Diaphragm-based pressure sensors have been fabricated incorporating waveguides on the top surface. Via the elasto-optic effect, the deflections in the diaphragm alter the phase of a light wave. This is detected by having a reference waveguide that is unaffected by pressure and by arranging the waveguides in a Mach-Zehnder interferometer configuration (Figure 3.4) [22, 23].
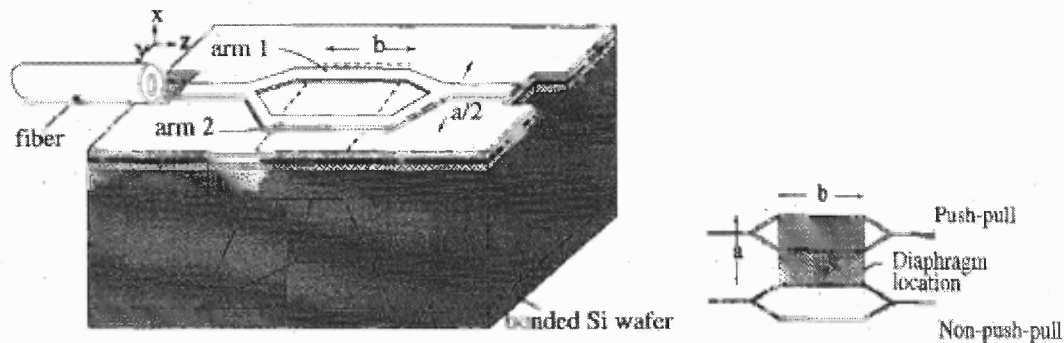
Figure 3.4 Micromachined Mach-Zehnder interferometer [22].

Another approach is the use of Fabry-Perot interferometry in which a Fabry-Perot cavity is created between a fiber tip and a silicon diaphragm. Figure 3.4 shows a cross sectional view of a Fabry-Perot diaphragm based sensor [A broad study of this technology is the subject of Chapter Five].
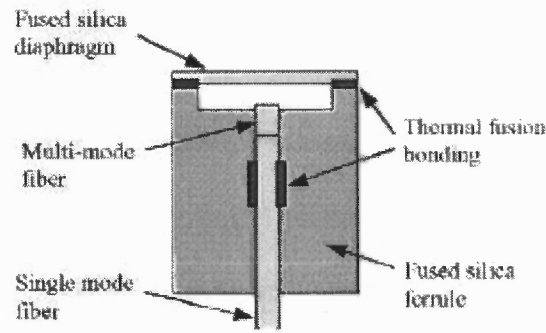
Figure 3.5 Fabry-Perot sensor [24].

3.2 Diaphragm Theory

Analysis of the static deflection of diaphragms is well documented in the classical plate bending literature. Solutions for small deflection theory and membrane theory are well known. The following is a concise summary of the plate theory extracted from several reference works [25-28].

A plate is a flat structure limited by two parallel planes, called faces. Let h be the thickness of the plate, i.e., h is the distance between the two faces. The static and dynamic loads carried by plates are predominantly perpendicular to the plate faces. The middle plane (midplane) is a plane parallel to the plate faces which divides the thickness into equal halves, i.e. $\dfrac{h}{2}$.
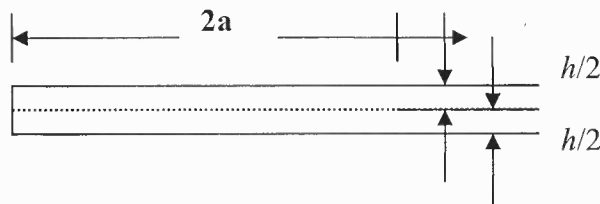
Figure 3.6 Plate midplane.

Being subject to transverse loads, an initially flat plate, with perimeter clamped, deforms and the midplane transforms into some curvilinear surface, which is referred to as the middle surface. A plate resists transverse loads by means of bending exclusively.

The flexural properties of a plane depend significantly on its thickness in comparison with other dimensions. Plates may be classified into three groups according to the ratio $(\frac{a}{h})$, where a represents the radius of the diaphragm.

1. **Thick Plate:** $(\frac{a}{h}) \leq 8...10$, the analysis of such bodies includes all the components of stresses, strain and displacement of solid bodies using the general equation of 3D elasticity.

2. **Membrane:** $(\frac{a}{h}) \geq 80...100$, these plates are devoid of flexural rigidity. Membranes carry lateral loads by axial tensile forces and shear forces acting in the middle surface of the plate. These forces are called membrane forces and they produce projection on a vertical axis and thus balance a lateral load that is applied to the plate-membrane.

3. **Thin Plates:** $8...10 \leq (\frac{a}{h}) \geq 80...100$, depending on the value of the ratio w/h, the ratio of maximum deflection (w) of the plate to its thickness, the part of flexural and membrane force here may be different. Therefore, this group may also be subdivided into two different classes:

   - **Stiff Plates:** $(\frac{w}{h}) \leq 0.2$, stiff plates are flexurally rigid thin plates. They carry loads two dimensionally, mostly by internal bending and twisting moments and by transverse shear forces. The middle plane deformation and the membrane forces are negligible. This concept introduces serious simplifications. A fundamental feature of stiff plates is that the equations of static equilibrium for a plate element may be set up for an original (undeformed) configuration of the plate.

   - **Flexible Plates:** $(\frac{w}{h}) \geq 0.3$, the lateral deflection will be accompanied by the stretching of the middle surface. These plates represent a combination of the stiff plates and membranes, and carry external loads by the combined action of internal moments, shear forces and membrane (axial) forces. When the magnitude of the maximum deflection is considerably greater than the plate thickness, the

membrane action predominates. So, if $(\frac{w}{h}) > 5$, the flexural stress can be neglected when compared with the membrane stress.

The analysis below follows the theory of **Thin Stiff Plates,** where $8...10 \leq (\frac{a}{h}) \geq 80...100$ and $(\frac{w}{h}) \leq 0.2$.

The classical differential equation of the motion for the transverse displacement w of the plate is give by:

$$D\nabla^4 w + \rho \frac{\partial^2 w}{\partial t^2} = 0 \qquad (3.3)$$

where D is the flexural rigidity and is defined by:

$$D = \frac{Eh^3}{12(1-\mu^2)} \qquad (3.4)$$

and where E is the Young's modulus, h is the thickness, μ is the Poisson's ratio, ρ is the mass density per unit area of the plate, t is time, and $\nabla^4 = \nabla^2\nabla^2$, where ∇^2 is the Laplacian operator.

3.2.1   Flat Diaphragms

The mathematical analysis will be based on a flat diaphragm with uniform thickness and composed of isotropic and homogeneous material, where the maximum deflection due to a normally applied pressure will not be more than 30% of the thickness. The deflection is due mostly to bending and the diaphragm will not be stressed beyond its elastic limit, and all loads are applied normally.

The deflection W(r) of a circular diaphragm with fixed edges loaded by pressure

P at the any radial distance r is:

$$W(r) = \frac{3(1-\mu^2)P(a^2 - r^2)^2}{16Eh^3}$$ (3.5)

a - radius of diaphragm
h - thickness
P - pressure
E - Young's Modulus (Elastic modulus which determines how much the material will compress under a given amount of external pressure E = stress/strain)
μ - Poisson's ratio (ratio of transverse contraction strain to longitudinal extension strain in the direction of stretching force)

The maximum deflection W_0 occurs at the center where r = 0 and is:

$$W_0 = \frac{3(1-\mu^2)Pa^4}{16Eh^3}$$ (3.6)

The radial stress is σ_r at any distance r from the center and may be calculated by:

$$\sigma_r = \pm\frac{3}{8}\frac{Pa^2}{h^2}[(3+\mu)\frac{r^2}{a^2} - (1+\mu)]$$ (3.7)

The maximum radial stress is at the edge (a = r) and is given by:

$$\sigma_{r_{max}} = \pm\frac{3}{4}\frac{Pa^2}{h^2}$$ (3.8)

where the inflection circle for the radial stress is located at $\left(a\sqrt{\frac{(1+\mu)}{(3+\mu)}}\right)$.

The tangential stress σ_t at any radial distance r may be calculated from:

$$\sigma_t = \pm\frac{3}{8}\frac{Pa^2}{h^2}[(3\mu+1)\frac{r^2}{a^2} - (1+\mu)]$$ (3.9)

The maximum tangential stress is at the center where r = 0 and is:

$$\sigma_{t_{max}} = \pm\frac{3}{8}(1+\mu)\frac{Pa^2}{h^2}$$

(3.10)

At the center, both the tangential and the radial stresses are equal. The tangential stress at the edge where r = a is:

$$\sigma_t = \pm\frac{3}{4}\mu\frac{Pa^2}{h^2}$$

(3.11)

where the inflection circle for the tangential stress is located at $a\sqrt{\frac{(1+\mu)}{(3\mu+1)}}$.

The natural frequency is given by:

$$f_n = \frac{10.21}{2na^2}[\frac{gD}{hw}]^{\frac{1}{2}}$$

(3.12)

where n refers to nodal diameters, w is in this case the specific weight of the material, g is the gravitational constant and D is the flexural rigidity. Substituting D and g, one obtains:

$$f_n = 9.22\frac{h}{a^2}[\frac{E}{w(1-\mu^2)}]^{\frac{1}{2}}$$

(3.13)

The natural frequency is proportional to $\frac{h}{a^2}$ and the stress is proportional to $\frac{a^2}{h^2}$;

the natural frequency can be increased by reducing the diameter of the diaphragm while keeping the stress constant, or by reducing h in the same ratio of a.

If the diaphragm is used to measure liquid pressure, the natural frequency is appreciably reduced. The equation for frequency is then given by:

$$f_n = \frac{9.22}{\sqrt{(1+\beta)}}\frac{h}{a^2}[\frac{E}{w(1-\mu^2)}]^{\frac{1}{2}}$$

(3.14)

where $\beta = 0.669\dfrac{w_1 a}{wh}$ and $\dfrac{w_1}{w}$ is the ratio of the densities of the fluid to the density of the

material of the diaphragm.

The deflection W_0 of a rectangular diaphragm of dimension a and b with fixed

edges loaded by pressure P at the center of the diaphragm is:

$$W_0 = \alpha\,(\frac{Pa^4}{Eh^3})(1-\mu^2)$$

(3.15)

The radial stress is may be calculated by:

$$\sigma = \beta\,(\frac{Pa^2}{h^2})$$

(3.16)

Table 3.2 Deflection and Stress Coefficients [26]

b/a	α	β_1	β_2	β_3	β_4
1.0	0.0151	0.3078	0.3078	0.1386	0.1386
1.1	0.0810	0.3486	0.3228	0.1584	0.1386
1.2	0.0206	0.3834	0.33748	0.1794	0.1368
1.3	0.0229	0.4122	0.3378	0.1962	0.1332
1.4	0.0248	0.4356	0.3408	0.2094	0.1272
1.5	0.0264	0.4542	0.3420	0.2208	0.1218
1.6	0.0276	0.4680	0.3426	0.2286	0.1158
1.7	0.0286	0.4794	0.3426	0.2352	0.1092
1.8	0.0294	0.4872	0.3426	0.2406	0.1044
1.9	0.0299	0.4932	0.3426	0.2442	0.0990
2.0	0.0305	0.4974	0.3426	0.2472	0.0948
∞	0.0312	0.4998	0.34260	0.2502	0.0750

Table 3.2 includes the deflection (α) and stress coefficients (β_1, β_2, β_3, β_4) for

various values of (b/a) ratio. The stress coefficient β_1 is determined at the center of the

long edge, β_2 corresponds to the stress at the center of the short edge, and β_3 and β_4 refer to the stress at the center of the plate [26].

The frequencies of the consecutive modes of vibration of a rectangular plate with sides a and b simply supported along the edges are given by:

$$f_{mn} = \frac{\pi}{2} [\frac{gD}{h\text{w}}]^{\frac{1}{2}} [\frac{m^2}{a^2} + \frac{n^2}{b^2}]$$

(3.17)

where m = 1, 2, 3,… and n = 1,2,3,…

The lowest mode of vibration will be obtained by letting m = 1 and n = 1. Introducing the value of g and the expression for D, we obtain:

$$f_{mn} = 8.91h [\frac{E}{(1-\mu^2)\text{w}}]^{\frac{1}{2}} [\frac{1}{a^2} + \frac{1}{b^2}]$$

(3.18)

In the same way as for the circular diaphragm, one introduces a correction factor in the presence of a fluid. Therefore, the frequency equation should be replaced by:

$$f_{mn} = \frac{8.91h}{\sqrt{(1+\beta)}} [\frac{E}{(1-\mu^2)\text{w}}]^{\frac{1}{2}} [\frac{1}{a^2} + \frac{1}{b^2}]$$

(3.19)

where $\beta = 0.669 \frac{\text{w}_1 a}{\text{wh}}$; and $\frac{\text{w}_1}{\text{w}}$ is the ratio of the density of the fluid to the density of the material of the diaphragm.

3.2.2 Embossed Diaphragm Analysis

In order for the small deflection theory to be effective, the thickness of the rigid center (Figure 3.7) should be at least 6 times the thickness of the diaphragm (H > 6h). The solidity ratio (b/a) is a very important parameter in the performance characteristics of the

diaphragm with rigid center. A (b/a) ratio of less than 0.15 will have little effect on the stiffness of the diaphragm [27].
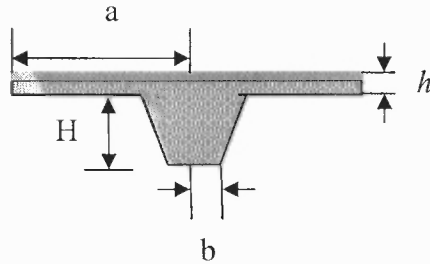
Figure 3.7 Silicon embossed diaphragm.

The deflection W_0 of a rigid center or embossed diaphragm (Figure 3.7) under pressure at small deflections may be expressed by the equation:

$$W_0 = A_p \frac{P}{E} \frac{a^4}{h^3}$$ (3.20)

a - radius of diaphragm
b- radius of the boss
h - Thickness
P - Pressure
E - Young's Modulus
μ - Poisson's ratio

where $\dfrac{1}{A_p}$ is a stiffness coefficient which depends on the solidity ratio (a/b):

$$A_p = \frac{3(1-\mu^2)}{16} * \left[1 - \frac{b^4}{a^4} - 4 * \frac{b^2}{a^2} \ln \frac{a}{b}\right]$$ (3.21)

The stiffness contribution brought about by the rigid center over the non-rigid center diaphragm is expressed by the right-hand factor in Equation 3.21.
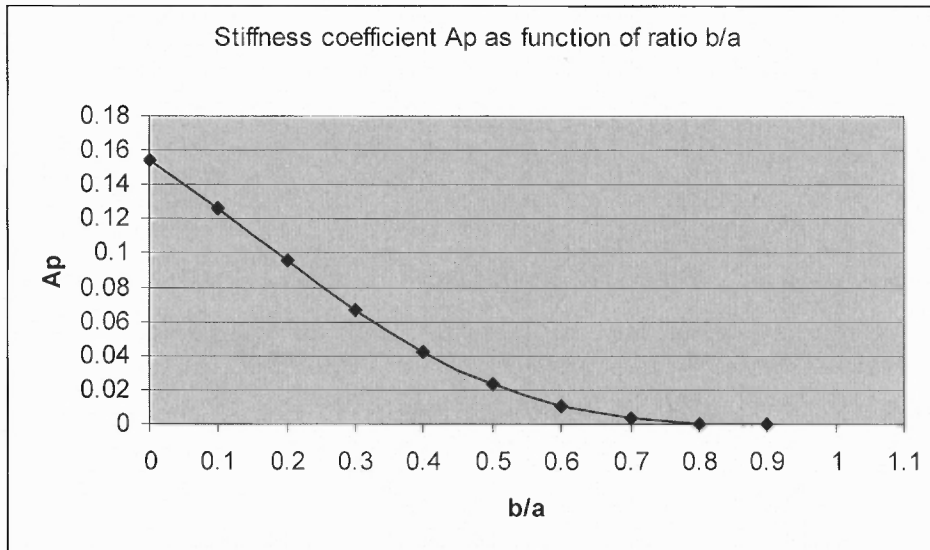
Figure 3.8 Stiffness contributions by the rigid center over flat diaphragm.

The chart in Figure 3.8 shows that increasing (b/a) ratio reduces the deflection of the diaphragm under applied pressure.

Since $A_p < 1$, the rigid center diaphragm has less sensitivity than the situation with non rigid center. However, the reduction in deflection under applied pressure makes the rigid center diaphragm more linear than the diaphragm without the rigid center.

The maximum radial bending stress occurs at the outer perimeter where the diaphragm is clamped and the inner perimeter where the boss begins.

The radial stress is given by:

$$\sigma_{router} = \sigma_{inner} = \pm \frac{3P}{4h^2}\left(a^2 - b^2\right) \tag{3.22}$$

which combining with equation (3.20) may be expressed in terms of the deflection W_0:

decreasing from full scale. The points are taken on the same continuous cycle. The deviation is expressed as a percent of full scale.

Output

Measurand

Figure 3.9 Hysteresis.

Linearity [26, 30]

Non-linearity (sometimes denoted linearity) is defined as the maximum deviation of the calibration curve (output vs. input) from a specified straight line, expressed as a percent of full scale output, and measured on increasing measurand only. It is directly related to the response of the diaphragm under applied pressure and it is defined as the closeness to which the response to pressure curve fits a straight line over the entire operation range. Performance conformity to straight-line behavior is highly desired by designers.

There are three definitions of linearity that are used in the specifications of pressure sensors:

decreasing from full scale. The points are taken on the same continuous cycle. The deviation is expressed as a percent of full scale.

Output

Measurand

Figure 3.9 Hysteresis.

Linearity [26, 30]

Non-linearity (sometimes denoted linearity) is defined as the maximum deviation of the calibration curve (output vs. input) from a specified straight line, expressed as a percent of full scale output, and measured on increasing measurand only. It is directly related to the response of the diaphragm under applied pressure and it is defined as the closeness to which the response to pressure curve fits a straight line over the entire operation range. Performance conformity to straight-line behavior is highly desired by designers.

There are three definitions of linearity that are used in the specifications of pressure sensors:

1. *Independent (or best fit straight line BFSL) linearity*: The maximum deviation of the actual output from a straight line positioned so as to minimize the maximum deviation (a best fit straight line) (Figure 3.10).
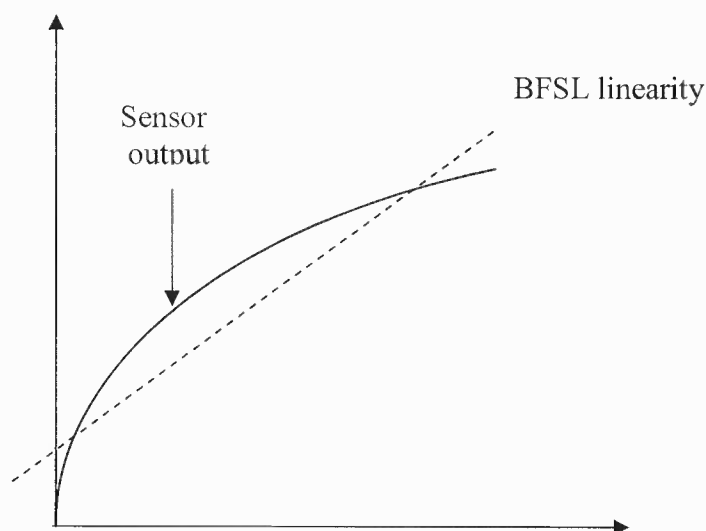
Figure 3.10 Best fit straight line linearity.

2. *Terminal base (TB) linearity:* The maximum deviation of the actual output from straight line coinciding with the actual output at upper and lower range values.
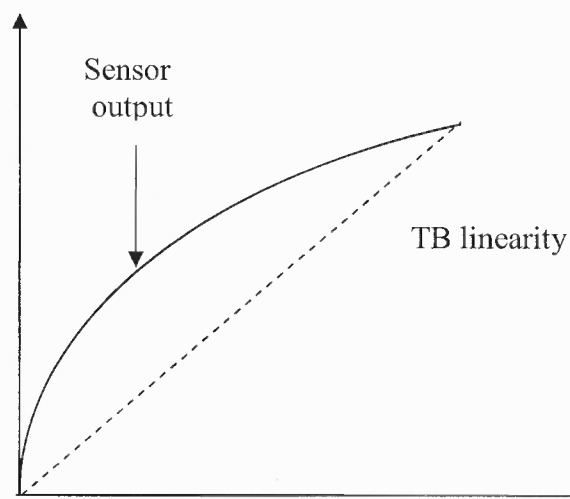
Figure 3.11 Terminal based linearity.

3. *Zero-Based(ZB) linearity:* The maximum deviation of the actual output from straight line positioned so as to coincide with the actual lower range value and to minimize the maximum deviation (Figure 3.12).
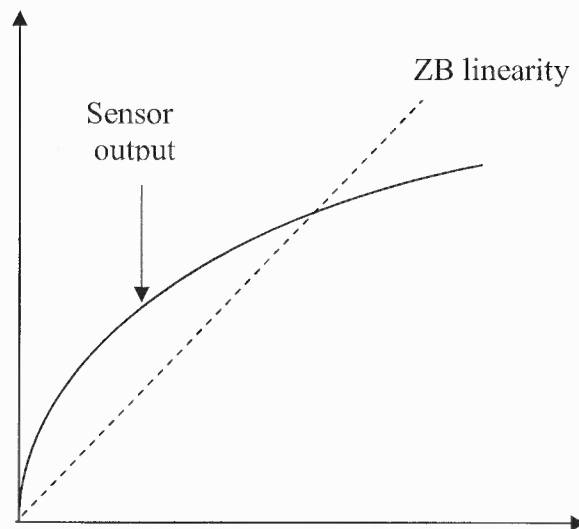
Figure 3.12 Zero based linearity.

Zero/Offset

Zero or offset is defined as the sensor output at a constant temperature with zero applied pressure.

Operating life [29]

The minimum length of time over which the sensor will operate, either continuously or over a number of on-off cycles whose duration is specified, without changing performance characteristics beyond specified tolerances, is known as operating life.

Overrange

Overrange is the maximum magnitude of measurand that can be applied to a sensor without causing a change in performance beyond a specified tolerance.

Repeatability [29, 30]

Non-repeatability (sometimes denoted repeatability) is defined as the ability of a transducer to reproduce output readings at room temperature, unless otherwise specified, when the same measurand value is applied to it consecutively, under the same conditions,

and in the same direction. It is expressed as the maximum difference between output readings as determined by two calibration cycles.

Resolution [29]

Resolution is the minimum change of the measurand value necessary to produce a detectable change at the output. When the measurand increment is from zero, it is called the threshold.

Sensitivity [26, 29]

The sensitivity is the relationship between applied load and deflection of a diaphragm. It is defined as the ratio of the change in deflection to a change in the load. The sensitivity is normally used in evaluating the diaphragm performance (Figure 3.13 and 3.14).
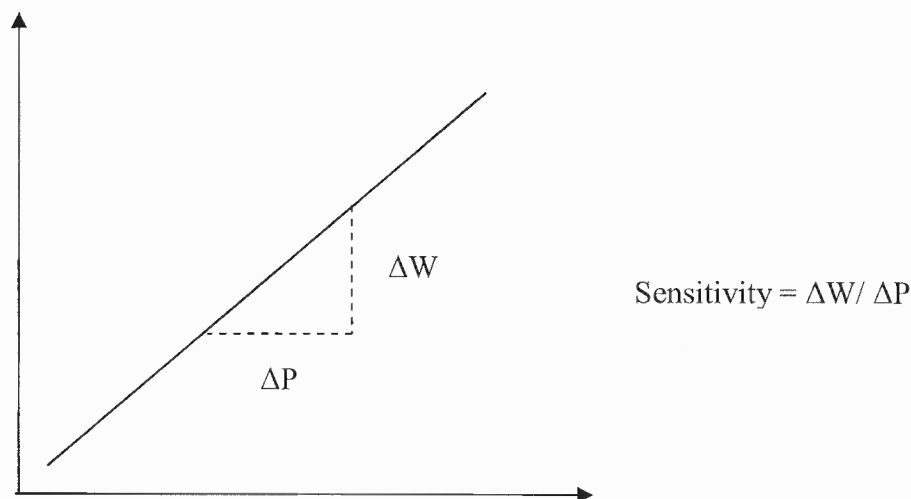
Figure 3.13 Sensitivity for linear system.
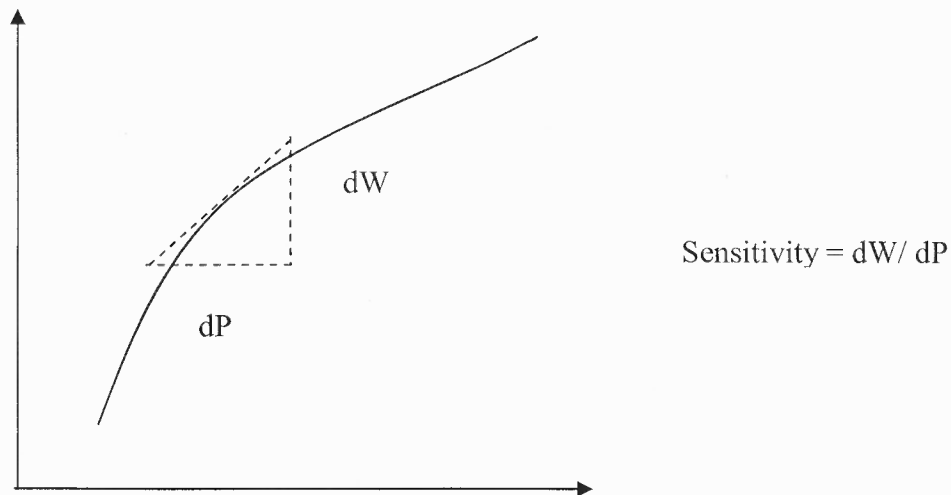
Figure 3.14 Sensitivity for nonlinear System.

Stability

Stability is the ability of a sensor to maintain its performance characteristics for a certain period of time.

Dynamic Range [30]

Dynamic range is the measured values over which a transducer is intended to operate, specified by upper and lower limits. The lower limit, when dynamically (ac coupled), is a few microvolts of noise generated by the silicon gauges and other internal components. When measuring statically (dc coupled), the lower limit will be determined by the zero measurand output and over the long term, very low frequency thermal zero drift.

3.4 Diaphragm Fabrication

A silicon embossed diaphragm can be fabricated following simple MEMS processes such as photolithography and dry and wet etching techniques (Figure 3.15). Depending on the nature of the sensor in which the embossed diaphragm will be used, these processes can be modified or combined with other MEMS processes.
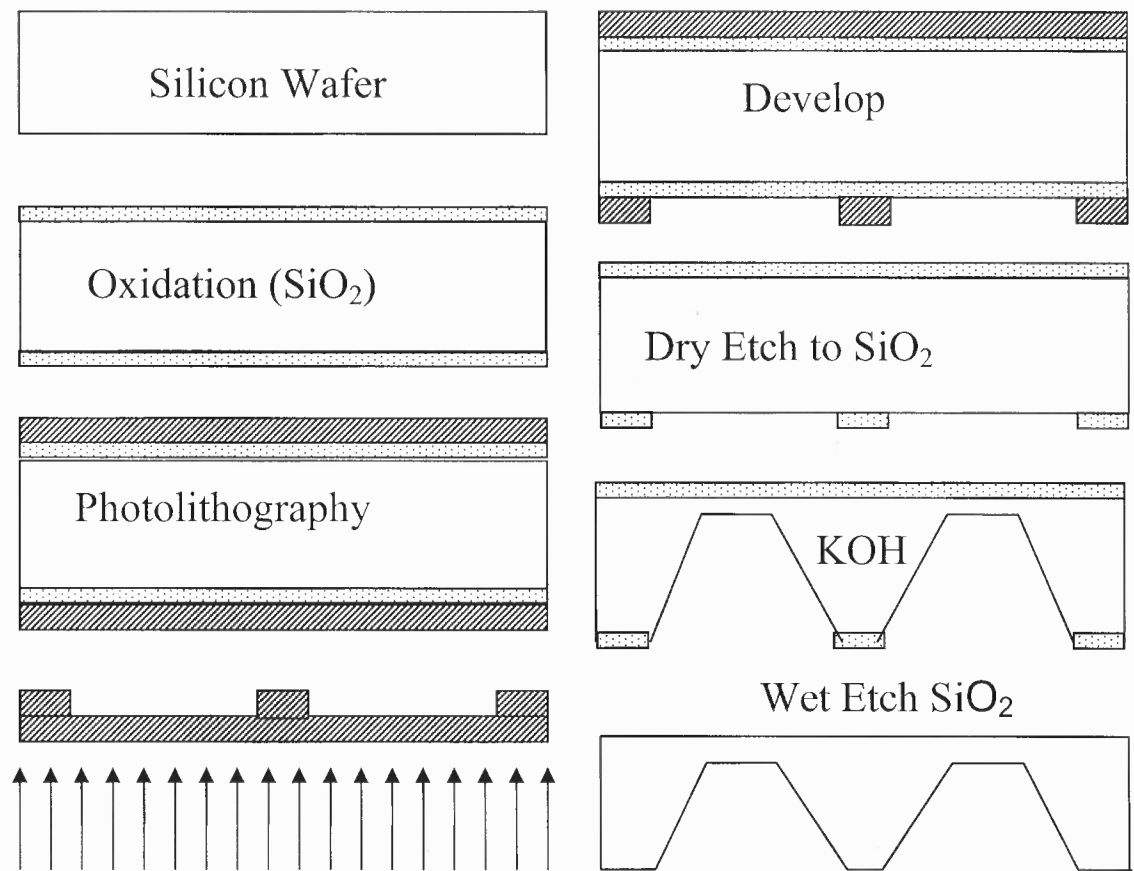
Figure 3.15 Embossed diaphragm fabrication.

CHAPTER 4

PIEZORESISTOR PRESSURE SENSORS

The piezoresistive pressure sensor elements comprise an etched diaphragm that is fabricated in single-crystal silicon and contains embedded resistors, typically four that are used in a Wheatstone bridge configuration. The resistors are located on the silicon membrane and metal paths provide electrical connections. When a differential pressure is applied, the membrane deflects, the piezoresistors change their resistances, unbalancing the bridge and developing a voltage that is proportional to the applied pressure [32].

Observations of piezoresistive effects in silicon and germanium were reported by Charles Smith in 1954 [33]. This discovery enabled the production of silicon-based pressure sensors, displacing older technology in traditional applications [34].

Initially, biomedical and aerospace applications with high-cost and low-volume were targeted [35]. Companies producing micro-sensors began to move toward higher-volume, lower cost applications in the 1970s [36-39], particularly in biomedical [40] and automotive [41] applications. From the 1980s to the present, piezoresistive based sensors are the most commonly available electronic pressure sensors with an extensive number of applications. Most common among them are applications in the automotive [42], marine [43], military systems, aerospace, oil resource and exploration [44], bioscience and medicine [45, 47] related industries.

4.1 Physical Properties of Silicon

In order to understand the piezoresistive effect in silicon, it is helpful to review a few topics in solid state physics, including atomic and crystalline structure, energy band theory, carrier transport, and carrier trapping at grain boundaries. Each of these aspects is described as they relate to the piezoresistive behavior of silicon.

4.1.1 Monocrystalline Silicon

Monocrystalline silicon has a diamond lattice crystal structure (Figure 4.1), i.e., the atoms are arranged in a periodic structure in which every atom is surrounded by four nearest neighbors. Every atom is covalently bonded to four neighboring atoms located at the corners of a tetrahedron. The smallest repeating unit of the lattice is cubic and silicon is therefore said to be a cubic material.
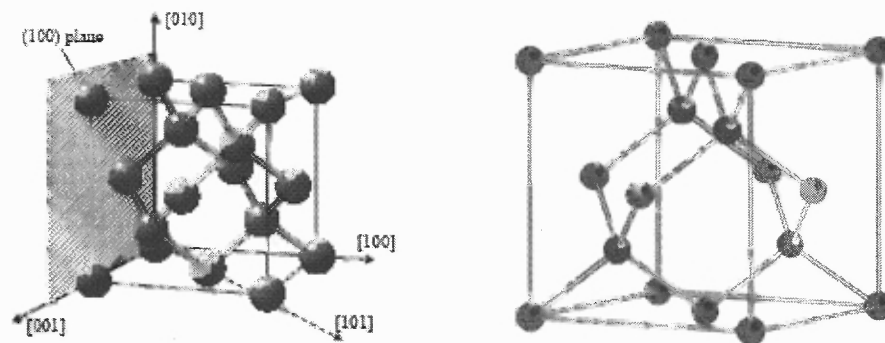
Figure 4.1 Diamond cubic crystal structure of silicon [2, 48].

Figure 4.2 shows the three crystallographic planes and their Miller indices for a simple cubic crystal. Two planes in the {110} set of planes are identified and note that (111) is the same plane as ($\overline{1}\,\overline{1}\,\overline{1}$) [49].
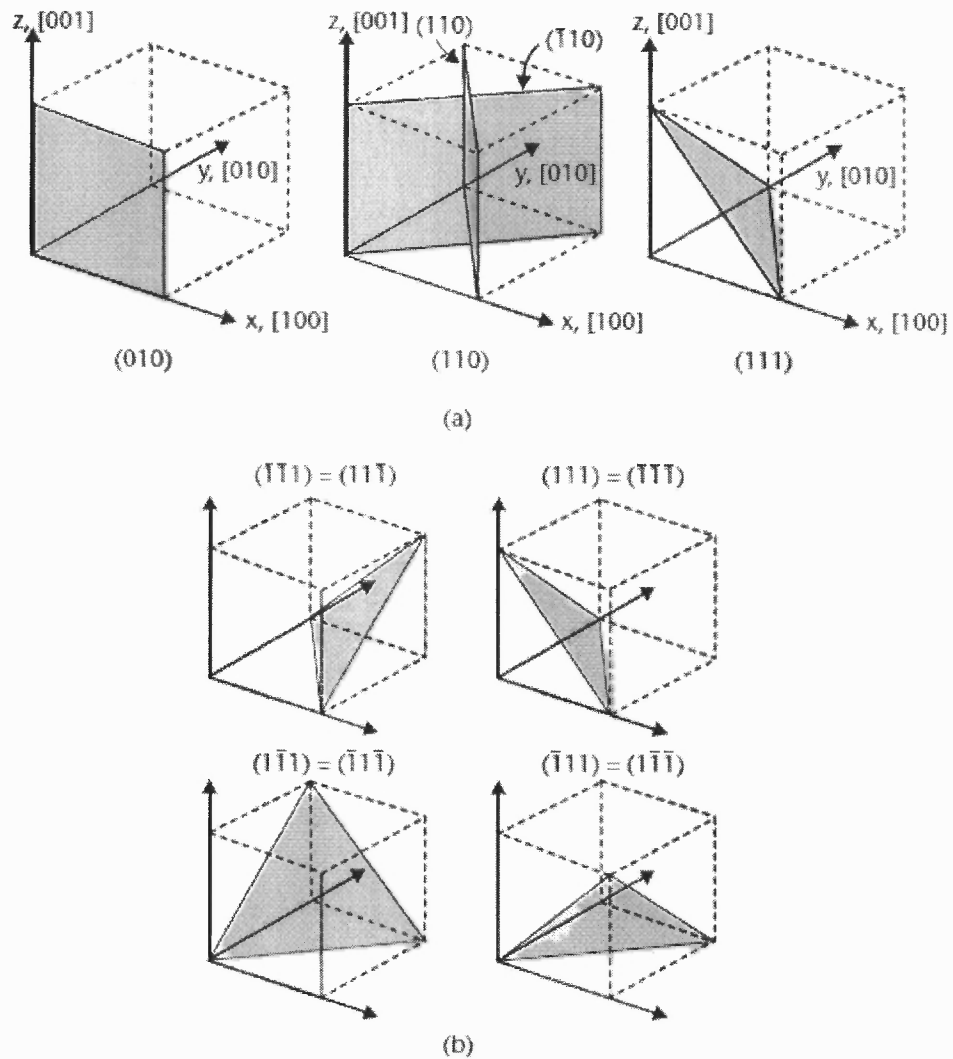
Figure 4.2 (a) Three crystallographic planes and their Miller indices for cubic crystal. Two planes in the {110} set of planes are identified. (b) The four planes in the {111} family [49].

4.1.2 Polycrystalline Silicon

In polycrystalline silicon (referred to as polysilicon or simply poly), there is no particular crystal orientation as in monocrystalline silicon. The polycrystalline structure is made up of small grains or crystallites each containing a large number of periodically arranged atoms with saturated bonds like in monocrystalline silicon. In the boundaries that separate the grains, the atoms do not have the periodic arrangement of the bulk crystal,

and the atoms have numerous incomplete or dangling bonds that affect the electrical properties. There is a close relationship between the mechanical and electrical properties of a polysilicon film and the structure. The structure describes the size of the crystallites and their preferred crystallographic orientation or texture. Polysilicon layers are in general not isotropic, i.e., there is a preferential orientation for the crystallites [50].

The mechanical properties are for the most part similar to those of monocrystalline silicon. The electrical properties of polysilicon differ substantially from those of monocrystalline silicon [51].

Several models have been proposed to explain the resistivity variation with dopant concentration in polycrystalline silicon [52-54]. The more generalized have been the dopant-segregation model and the carrier-trapping model:

- In the dopant-segregation model, the grain boundary serves as a sink for preferential segregation of impurity atoms that become inactive at the boundary. This model, however, cannot explain the mobility minimum at the critical doping level and the temperature dependence of resistivity.

- In the carrier-trapping model, the grain boundary contains trapping states caused by defects resulting from disordered or incomplete atomic bonding. These states trap a portion of the carriers from the ionized and uniformly distributed dopants. This process not only reduces the number of carriers but also creates a potential barrier from the electrically charged traps and impedes the motion of carriers from one crystallite to another. This model better explains the sharp change in resistivity versus doping level, mobility minimum, and temperature dependence. Even if the dopants do segregate, the trapping model can still be applied, based on an active-dopant concentration that can be obtained by subtracting the inactive-dopant concentration from the implanted concentration.

Polysilicon Resistivity

A complete expression for the resistivity of p-type polycrystalline is [51]:

$$\rho = \frac{1}{gq\mu_p p_0}(1 - \frac{2W}{L}) + \frac{\sqrt{2\pi m_p^* kT}}{f \, Lq^2 p_0} \exp(\frac{qV_b}{kT}) \qquad (4.1)$$

where m_p^* is the effective mass of the holes, W is the width of the depletion region, L is the grain size, k is Boltzmann's constant, T the absolute temperature, μ_p is the mobility of holes and p_0 is the equilibrium concentration of holes within the undepleted grain regions, V_b is the potential barrier, and g and f are correction factors. The first term represents the grain-boundary depletion effect and the second term is due to inter-grain transport.

The doping concentration affects the resistivity through p_0, the ratio W/L and the potential barrier V_b. At low doping concentrations ($p_0 < 3\times10^{18}$ cm^{-3}), the exponential term related to the grain-boundary resistivity is dominant; at high doping concentrations ($p_0 > 2\times10^{19}$ cm^{-3}), the exponential term decreases and the term related to the grain resistivity becomes the dominating one.

4.1.3 Energy Band Structure

When pure silicon forms the diamond cubic crystal structure, all four valence electrons are covalently bonded with neighboring silicon atoms. This crystal structure has a full valence band and an empty conduction band. These energy bands represent the energy levels in which electrons can be located. How easily electrons or holes can reach the conduction band is key to determining the conductivity or resistivity of the material.

In semiconductors, an energy band gap separates the conduction and valence energy bands. This band gap represents the energy required by the highest electron in the valence band to enter the empty conduction band.

For insulators, the band gap is large, meaning that more external energy is required for electrons in the valence band to get to the conduction band and move throughout the solid. When the band gap is reduced or the energy level of the highest valence electron is increased, the conductivity of the crystal increases. Once it has received the necessary energy (E_g) to go up the band gap, an electron is able to move throughout the crystal structure (Figure 4.3).

Electrons moving through a crystal are called charge carriers, as they are the means of transporting charge throughout a solid. Holes are also charge carriers because they have a charge equal in magnitude but opposite in sign as the charge of an electron and can be transported throughout the crystalline lattice.
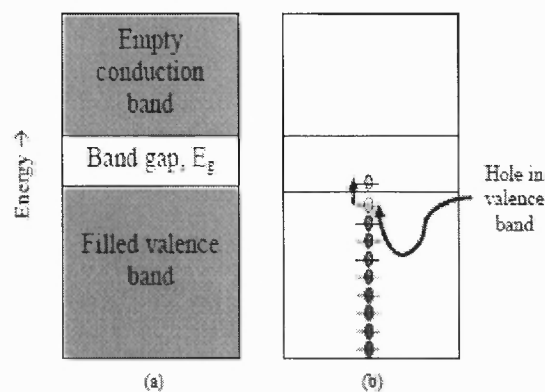
Figure 4.3 (a) Electron energy band structure for semiconductors. (b) Electron and hole location within the energy band structure for p-type silicon [48].

4.1.4 Carrier Transport

For silicon doped with boron, the outer energy level of the valence band is occupied by a hole. The impurity boron atom, which has three valence electrons, bonds to the silicon crystal and contributes a hole to the lattice. When subject to an external electric field, the hole is transferred to another crystal as it switches with the electron in that bond. The hole in motion becomes the charge carrier.

In the presence of an electric field, the holes located in p-type silicon will flow in the direction of the electric field. The actual velocity of the hole, termed the carrier drift velocity, does not follow a straight line but is scattered, since the motion of the charge carrier is impeded and redirected as it collides with other carriers, phonons, grain boundaries and dislocations.

The complex band structure of p-type silicon complicates the analysis of its piezoresistive behavior. Some physicists attribute the piezoresistive behavior of p-type silicon to the separation of heavy and light hole valence bands.

The piezoresistive behavior of phosphorous doped (n-type) silicon, on the other hand, is attributed to the creation of an extra electron energy level near the top of the energy band gap. Electrons in this energy level are more easily excited into the conduction band under an applied stress or strain.

The ability of a material to transport carriers (electrons or holes) in this manner is one way of describing the conductivity of the semiconductor. For a material to be highly conductive requires a large number of mobile charge carriers. The concentration of charge carriers in a semiconductor depends on the concentration of impurity atoms (dopant level) as well as the temperature.

The electrical conductivity, σ, of a semiconductor is a function of the number of charge carriers and their respective mobilities, as expressed by:

$$\sigma = \frac{1}{\rho} = n|e|\mu_e + p|e|\mu_h \tag{4.2}$$

where n and p are the number of electrons and holes, respectively, and μ_e and μ_h are the electron and hole mobility, respectively, and $|e|$ is the absolute charge of an electron or hole. Electrical resistivity, ρ, is the inverse of electrical conductivity. From this equation,

it is obvious that increasing the concentration of holes or electrons and/or increasing their respective mobility will increase the conductivity, and therefore decrease the resistivity of the material.

4.2   The Piezoresistivite Effect

Piezoresistivity is an effect by which electrical resistivity changes under an applied strain. Its name is derived from the Greek word "piezin", meaning to press [10].

Although the effect was first discovered by Lord Kelvin in 1856, who noted that the resistance of copper and iron wires increased when in tension, the first application appeared in the 1930's with the introduction of the metal foil strain gauge (Figure 4.4).
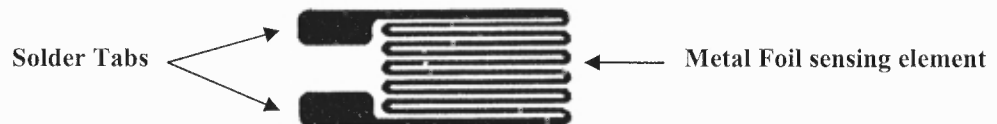
Figure 4.4 Typical metal foil strain gauge [55].

Today's research focuses on the piezoresistive behavior of silicon, because it has large piezoresistivity and when integrated with its excellent mechanical properties, it is appropriate for the conversion of mechanical deformation to an electrical signal. Silicon resistors exhibit better performance compared to classical strain gauges. Some of the practical advantages that have been recognized from the beginning are [29]:

1. The gauge factor of semiconductors is higher than that of metal (about of an order of magnitude).
2. Silicon is a very robust material.
3. Integration of the gauge and membrane eliminates the need for separate components, which eliminates hysteresis and creep.

4. The strain is transmitted perfectly from the membrane to the gauge.

5. The resistors are limited to the surface of the element in bending or torsion where the stresses are maximal.

6. Good matching of the resistors can be achieved, which is valuable if Wheatstone bridges are used.

7. The technique is very appropriate for miniaturization of the sensor.

8. Mass fabrication can profit from the available technology.

9. It is possible to integrate electronic circuitry directly on the sensor chip for signal amplification and temperature compensation.

While the mechanism for silicon piezoresistivity is not well understood, it is hypothesized that the inter-atomic spacing of the silicon crystal structure changes when the material is stressed. This change in crystal structure increases or decreases the silicon semiconductor band-gap energy, affecting the effective mass and mobility of electrons and holes, hence, modifying the resistivity [52, 53].

4.2.1 Mathematical Description

For a three-dimensional anisotropic crystal, the electric field vector $\vec{E}$ is related to the current vector $\vec{J}$ by a three-by-three resistivity tensor ρ (Ohm's law).

$$\begin{bmatrix} E_1 \\ E_2 \\ E_3 \end{bmatrix} = \begin{bmatrix} \rho_1 & \rho_6 & \rho_5 \\ \rho_6 & \rho_2 & \rho_4 \\ \rho_5 & \rho_4 & \rho_3 \end{bmatrix} \cdot \begin{bmatrix} J_1 \\ J_2 \\ J_3 \end{bmatrix} \tag{4.3}$$

The resistivity tensor always reduces to 6 coefficients due to crystal symmetry. For silicon (cubic crystal) the first three resistivity terms, ρ_1, ρ_2, ρ_3, which represent resistivity along the <100> axes, are identical ($\rho_1 = \rho_2 = \rho_3 = \rho$) and the last three terms,

ρ_4, ρ_5, ρ_6, which relate the electric field in one direction to a perpendicular current, are

zero ($\rho_4 = \rho_5 = \rho_6 = 0$).

In a piezoresitive material, these six resistivity components depend on the stress in the material, which can also be decomposed into six components: three normal stresses σ_1, σ_2, and σ_3 along the cubic crystal axes, and three shear stresses τ_1, τ_2, and τ_3 as defined in Figure 4.5 [29].
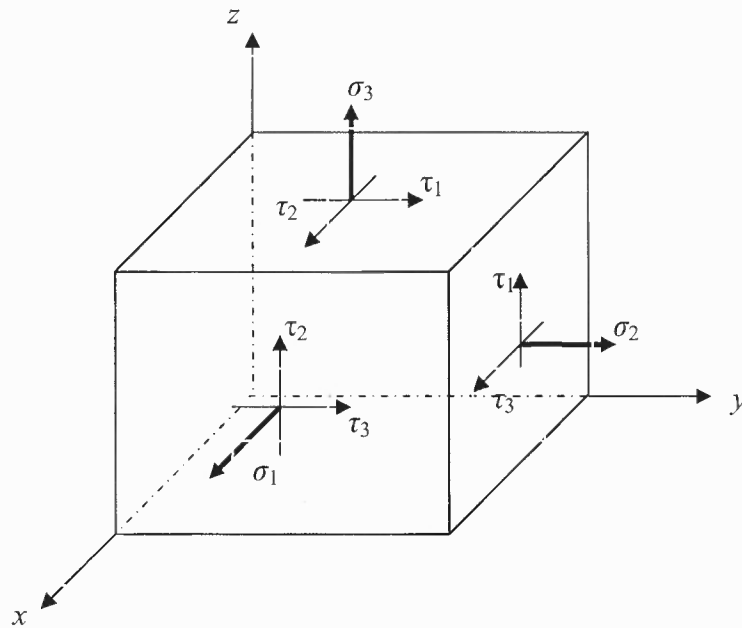
Figure 4.5 Definition of the normal stresses σ_i, and shear stresses τ_i (i=1,2,3) [29].

For a stressed crystal, these resistivity components can be expressed by:

$$\begin{bmatrix} \rho_1 \\ \rho_2 \\ \rho_3 \\ \rho_4 \\ \rho_5 \\ \rho_6 \end{bmatrix} = \begin{bmatrix} \rho \\ \rho \\ \rho \\ 0 \\ 0 \\ 0 \end{bmatrix} + \begin{bmatrix} \Delta\rho_1 \\ \Delta\rho_2 \\ \Delta\rho_3 \\ \Delta\rho_4 \\ \Delta\rho_5 \\ \Delta\rho_6 \end{bmatrix} \tag{4.4}$$

where $\Delta\rho_i$ is the resistivity change due to the stress.

The change in resistivity is related to the piezoresistance coefficients and the stress by a 6x6 tensor, which, for an isotropic material with cubic crystalline structure, reduces to three non-zero terms: π_{11}, π_{12}, and π_{44} [56]. These coefficients relate the fractional change in resistivity to the six stress components (Figure 4.5) [57].

$$\frac{1}{\rho}\begin{bmatrix} \Delta\rho_1 \\ \Delta\rho_2 \\ \Delta\rho_3 \\ \Delta\rho_4 \\ \Delta\rho_5 \\ \Delta\rho_6 \end{bmatrix} = \begin{bmatrix} \pi_{11} & \pi_{12} & \pi_{12} & 0 & 0 & 0 \\ \pi_{12} & \pi_{11} & \pi_{12} & 0 & 0 & 0 \\ \pi_{12} & \pi_{12} & \pi_{11} & 0 & 0 & 0 \\ 0 & 0 & 0 & \pi_{44} & 0 & 0 \\ 0 & 0 & 0 & 0 & \pi_{44} & 0 \\ 0 & 0 & 0 & 0 & 0 & \pi_{44} \end{bmatrix} \begin{bmatrix} \sigma_1 \\ \sigma_2 \\ \sigma_3 \\ \sigma_4 \\ \sigma_5 \\ \sigma_6 \end{bmatrix} \qquad (4.5)$$

Combining Equations 4.3, 4.4 and 4.5, we obtain an expression for the electric field under stress:

$$E_1 = \rho J_1 + \rho\pi_{11}\sigma_1 J_1 + \rho\pi_{12}(\sigma_2 + \sigma_3)J_1 + \rho\pi_{44}(J_2\tau_3 + J_3\tau_2)$$

$$E_2 = \rho J_2 + \rho\pi_{11}\sigma_2 J_2 + \rho\pi_{12}(\sigma_1 + \sigma_3)J_2 + \rho\pi_{44}(J_1\tau_3 + J_3\tau_1) \qquad (4.6)$$

$$E_3 = \rho J_3 + \rho\pi_{11}\sigma_3 J_3 + \rho\pi_{12}(\sigma_1 + \sigma_2)J_3 + \rho\pi_{44}(J_1\tau_2 + J_2\tau_1)$$

With knowledge of the value of three parameters π_{11}, π_{12}, and π_{44} (which can be measured) in reference to a coordinate system aligned to <100> axes of the silicon crystal, all the piezoresistance properties of silicon can be calculated.

Of all possible orientations that can be calculated, two of them represent the most common situation for piezoresitive sensor devices: the first is related to a uniaxial state of stress σ^*, electric field E^* and current J^*, all in the same direction, but not necessarily

along a crystal axis. In this case, the relation between stress and change of resistivity is denoted the longitudinal piezoresistance coefficient (π_l). In the second case, the electric field and current are collinear, and the uniaxial stress is perpendicular to both, and is denoted transverse piezoresistance coefficient (π_t).

In order to calculate π_l and π_t as a function of the three piezoresistance coefficients in the <100> axis system, it is necessary to apply an axis transformation to Equation 4.6 [30], resulting in:

$$E^* = \rho J^* + \rho J^*[\pi_{11} + 2(\pi_{44} + \pi_{12} - \pi_{11})(l_1^2 m_1^2 + l_1^2 n_1^2 + m_1^2 n_1^2) \qquad (4.7)$$

and hence, the longitudinal and transverse piezoresistance coefficients can be written as:

$$\pi_l = \pi_{11} + 2(\pi_{44} + \pi_{12} - \pi_{11})(l_1^2 m_1^2 + l_1^2 n_1^2 + m_1^2 n_1^2) \qquad (4.8)$$

$$\pi_t = \pi_{12} - (\pi_{44} + \pi_{12} - \pi_{11})(l_1^2 l_2^2 + m_1^2 m_2^2 + n_1^2 n_2^2) \qquad (4.9)$$

respectively, where l, m, n are the direction cosines of the crystal lattice.

The longitudinal and transverse coefficients allow the calculation of the fractional change in resistivity along the direction, of applied stress, and transverse or perpendicular to applied stress, as expressed by:

$$\frac{\Delta \rho_l}{\rho_l} = \pi_l \sigma_l \qquad (4.10)$$

and

$$\frac{\Delta \rho_t}{\rho_t} = \pi_t \sigma_t \qquad (4.11)$$

The longitudinal and transverse piezoresistance coefficients have been tabulated for various crystal directions as shown in Table 4.1 [29, 58].

Table 4.1 Longitudinal and Transverse Piezoresistance Coefficients for Various Combinations of Directions in Cubic Crystal [49]

Longitudinal Direction	π_l	Transverse Direction	π_t
(1 0 0)	π_{11}	(0 1 0)	π_{12}
(0 0 1)	π_{11}	(1 1 0)	π_{12}
(1 1 1)	$\frac{1}{3}(\pi_{11}+2\pi_{12}+2\pi_{44})$	(1 $\bar{1}$ 0)	$\frac{1}{3}(\pi_{11}+2\pi_{12}-\pi_{44})$
(1 1 $\bar{0}$)	$\frac{1}{2}(\pi_{11}+\pi_{12}+\pi_{44})$	(1 1 1)	$\frac{1}{3}(\pi_{11}+2\pi_{12}-\pi_{44})$
(1 1 $\bar{0}$)	$\frac{1}{2}(\pi_{11}+\pi_{12}+\pi_{44})$	(0 0 1)	π_{12}
(1 1 0)	$\frac{1}{2}(\pi_{11}+\pi_{12}+\pi_{44})$	(1 $\bar{1}$ 0)	$\frac{1}{2}(\pi_{11}+\pi_{12}-\pi_{44})$

Although the π_l and π_t coefficients provide a more general application of the principle piezoresistance coefficients, these should be directly applied only to single-crystal silicon. In order to apply them to a polycrystalline material, a weighted average of the piezoresistance effect in the various crystal directions must be employed. This is accomplished using a texture function, which expresses the probability of specific grain orientations. Assuming completely random grain orientations, this texture function is unity and the average longitudinal and transverse piezoresistance coefficients are calculated as:

$$<\pi_l>=\pi_{11}-0.400(\pi_{11}-\pi_{12}-\pi_{44}) \tag{4.12}$$

$$<\pi_t>=\pi_{11}+0.133(\pi_{11}-\pi_{12}-\pi_{44}) \tag{4.13}$$

For n-type polysilicon ($n = 4\times10^{14}$ cm^{-3}) with modulus of elasticity of 168 GPa and $\mu = 0.22$, the average longitudinal and transverse piezoresistance coefficients are -45.4×10^{-11} Pa^{-1} and 34.5×10^{-11} Pa^{-1}, respectively. The average longitudinal and transverse coefficients for p-type polysilicon ($p = 1.5\times10^{15}$ cm^{-3}) are 58.8×10^{-11} Pa^{-1} and -18.4×10^{-11} Pa^{-1}, respectively.

4.2.2 Gauge Factor

When a conductor is strained, its length and thickness change. Since electric current is forced to travel a longer path of smaller area when the conductor is stretched by tension, the resistance of the conductor increases.

An essential component of piezoresistance models is the gauge factor. The gauge factor, as has been defined in Chapter Two is the fractional change in resistance, $\dfrac{\Delta R}{R}$, per unit strain, ε, expressed as:

$$G = \frac{\Delta R}{\varepsilon R} \qquad (4.14)$$

where G is dimensionless. Table 4.2 summarizes values of gauge factors for various types of gauges.

Table 4.2 Different Types of Gauges Exhibit Different Gauge Factors [30]

Type of Gauge	Gauge Factor
Unbonded Wire	4
Bonded Foil	2
Thin Film	2
Bonded Discrete Semiconductor	50 to 200
Integral Diffused or Isolated Semiconductor	50 to 200

The resistance of a material is related to its resistivity and geometry by:

$$R = \frac{\rho L}{A} \qquad (4.15)$$

where ρ, L and A denote the material resistivity, the length in the direction of current flow and the cross sectional area, respectively. Implicit differentiation of Equation 4.16 results in:

$$\frac{\Delta R}{R} = \frac{\Delta \rho}{\rho} + \frac{\Delta L}{L} - \frac{\Delta A}{A}$$ (4.16)

The fractional change in area $\frac{\Delta A}{A}$ can be expressed in terms of the transverse strain by:

$$\frac{\Delta A}{A} = \frac{\Delta w}{w} + \frac{\Delta h}{h} = -\varepsilon_t - \varepsilon_z$$ (4.17)

where, $\varepsilon_t = \varepsilon_z$, including longitudinal strain ($\varepsilon_l = \frac{\Delta L}{L}$). Equation 4.17 can be expressed as:

$$\left(\frac{\Delta R}{R}\right)_l = \left(\frac{\Delta \rho}{\rho}\right)_l + \varepsilon_l - \varepsilon_t - \varepsilon_z$$ (4.18)

and, using Poisson's ratio ($\mu = -\frac{\varepsilon_t}{\varepsilon_l}$), one obtains

$$\frac{\Delta R}{R} = \frac{\Delta \rho}{\rho} + (1 + 2\mu)\varepsilon_l$$ (4.19)

Dividing both sides of Equation 4.19 by ε, one obtains another expression for the gauge factor as:

$$G = \frac{\Delta R}{\varepsilon R} = \frac{\Delta \rho}{\rho}\frac{1}{\varepsilon} + (1 + 2\mu)$$ (4.20)

For metals, the resistivity does not vary with strain; so the last term in Equation 4.20 can be ignored. The change in the resistance of metals with strain is due solely to geometric effects. However, in semiconductor materials, the strain dependency of the

first term in Equation 4.20, i.e., in the resistivity ρ, is significantly larger than the geometrical piezoresistive effect and this results in semiconductor strain gauges having large gauge factors. Thus, the gauge factor for silicon is dependent on Poisson's ratio and the fractional change in resistivity under a known strain. This fractional change in resistivity $\frac{\Delta\rho}{\rho}$ is the principle source of piezoresistive behavior in semiconductors.

Higher gauge factor means higher output for the same strain, or higher sensitivity relative to the stiffness and natural frequency of the structure. Semiconductor gauges have much higher gauge factors than those of metal gauges because, in addition to the lengthening and narrowing of the conductor, the resistivity of doped silicon changes under strain.

The change in electrical resistance of a strain gauge with the application of a physical stress is referred to as the piezoresistive effect.

4.2.3 The Piezoresistive Effect in Silicon

P-type silicon, which possesses a very large gauge factor of up to 200, in comparison with n-type silicon (gauge factor down to −140), is generally used in the fabrication of piezoresistors.

The many-valley model [59] has been very successful in describing piezoresistivity in n-type silicon.

Recently, Richter et al. [60] calculated the piezocoefficient π_{44} in p-type silicon based on a 6X6 $\mathbf{k \cdot p}$ (6X6) model as well as a state-of-the-art tight-binding (TB) model. They fabricated and characterized silicon samples in order to compare theory with experimental results. The piezoresistance was calculated using the Boltzmann transport

equation considering various models for the energy-dependent relaxation time. They found that it is vital to include all scattering mechanisms properly in the relaxation time, as also noted by Ohmura [61]. Kozlovskiy et al. [62] carried out a detailed analytical study of piezoresistance in p-type silicon using analytical valence band models of varying complexity, derived from Pikus and Bir [63], and combined with a power law model for momentum relaxation time, as was used in previous works [64-66]. Approximations to the valence band structure valid close to the top of the valence band were used by Suzuki [64], and Kleimann [65], while Toriyama and Sugiyama [66] used an approximation valid at larger hole energies.

Equation 4.20 in the previous section, shows that a change in resistance is generally dependent on a term which has to do with the geometrical piezoresistive effect and a term originating from the strain dependency of the resistivity ρ. The large gauge factor in semiconductors can only be due to the strain sensitivity of the resistivity in semiconductors. An explanation involves the theory of the electronic energy-band structure of semiconductors [30].

In classical as well as quantum mechanics, the energy E of a particle can be expressed in terms of the mass m and the momentum p. The kinetic energy is given by:

$$E = \frac{mv^2}{2}$$

(4.21)

where m is the mass and v is the velocity. The momentum is given by:

$$p = mv$$

(4.22)

where the energy E is expressed in terms of momentum p:

$$E = \frac{p^2}{2m} \qquad (4.23)$$

Figure 4.6 shows the plot of E as a function of p, which applies for free-moving electrons, as a parabola (dashed curve).
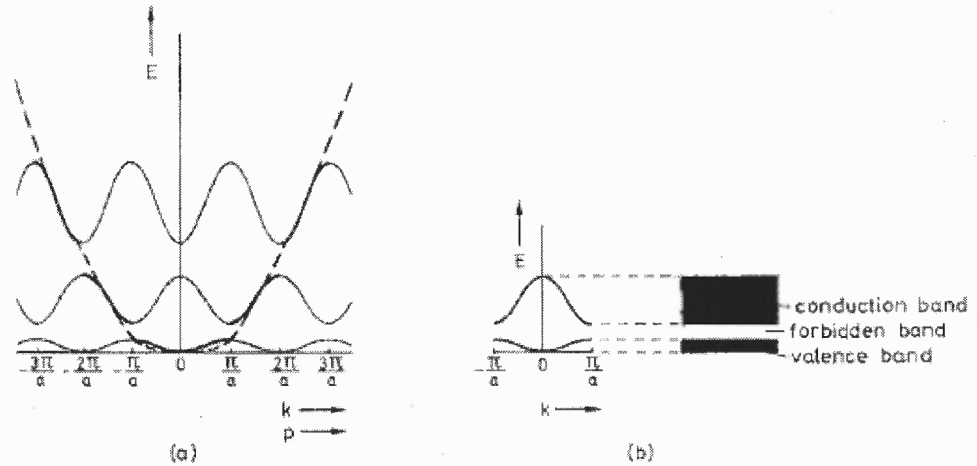
Figure 4.6 (a) Energy E as a function of the momentum p for a classical particle (dashed curve) and as a function of the wave number k for a particle with wave-like nature in interaction with a periodic crystal lattice (solid curves); (b) Part of the possible solutions indicating the conduction, forbidden and valence bands [30].

When an electron moves in a solid, an interaction of the electron with the periodic lattice of atoms in the crystal is expected. This interaction leads to the important result that the energy curve is no longer continuous as for the free electrons, but rather it shows discontinuities at certain values of momentum. The graph describing the relation between E and p is shown in Figure 4.6 as a solid curve. This result is obtained for a very simple, one dimensional lattice case. However, actual three dimensional lattices show similar discontinuities in the energy-momentum relations.

Replacing the momentum by the wave-number k, one obtains:

$$p = \frac{hk}{2\pi} \qquad (4.24)$$

where h is the Planck's constant. As indicated in Figure 4.6 (a), the discontinuities in the energy occur at:

$$k = \frac{n\pi}{a}, \text{n} = -1,-2, ..., \text{and n} = 1,+2, ...$$ (4.25)

where a is the lattice spacing. For values of k far from the discontinuity points given by Equation 4.26, the dashed and solid curves coincide, which means that the electrons behave as free electrons. However, when k is close to nπ/a, certain energy levels are forbidden, which is due to the strong interaction of the electrons with the lattice.

The periodic occurrence of forbidden energy gaps has to do with the wave-like nature of electrons moving in a periodic lattice, as in Figure 4.6 (b). For all k values, we obtain two energy levels. Two bands of allowed energy levels occur. Between these, a band is obtained for energy levels that are forbidden for the electrons. The relationship between E and k, as depicted in Figure 4.6 (b), only applies for the very simple case of a one-dimensional lattice. For real three-dimensional semiconductors like silicon, the situation is much more complex.

Detailed band-structure calculations are rather difficult in the three-dimensional case. Solutions are often found for directions of high crystalline symmetry such as the [100] and [111] directions as shown in Figure 4.7, where these parts of the band structure of silicon that are relevant for explaining the piezoresistive effect in silicon are shown.
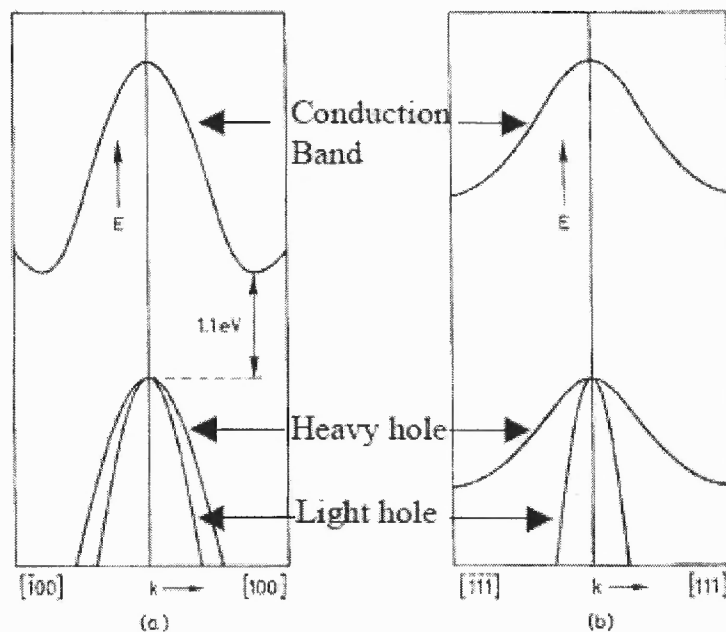
Figure 4.7 Energy band structures of silicon for (a) the [100] and (b) the [111] directions [30].

In order to understand the piezoresistive effect in p-type silicon, one must first understand the concepts of carrier effective mass and mobility. Figure 4.7 shows that near the maxima, the hole bands (lower two bands) in both the [100] and [111] directions are parabolic in shape. This can be directly compared with the case of a free electron (Equation 4.24) which is also parabolic. The hole band parabola is upside down because the hole charge is opposite to that of an electron. By making comparison with Equation 4.24, we define an effective hole mass which corresponds to the curvature of the parabola in the energy band diagram: the tighter the parabola, the lower the effective mass.

When an electric field is applied across a semiconductor, the charged carriers, which are holes in the case of p-type silicon, move in the direction of the field. When the electric field is increased, the holes move faster. The ratio between the speed of the holes and the electric field is known as the mobility. In a semiconductor with a high mobility,

the holes move faster for the same applied electric field. The mobility is related to the hole effective mass just as if the holes were actually heavier: holes with a larger effective mass move more slowly, and, therefore, have lower mobilities. Thus, the higher the mobility of the charge carriers, the higher the current resulting from the same applied electric field, and, therefore, the lower the resistivity.

Therefore, holes in a p-type semiconductor behave similarly to free electrons with the exception that their effective mass is different. Inspection of Figure 4.7 reveals that silicon has two types of holes with different effective masses, known as the heavy holes and the light holes, and it is this variation in effective mass (and hence mobility) which leads directly to the piezoresistive effect. Actually, the silicon band structure has a third hole band, known as the split-off hole band, which is not pictured in Figure 4.7 because it does not play a significant role in piezoresistance.

The average mobility of charge carriers in p-type silicon is the average mobility of the individual holes in the silicon and therefore is determined by the proportion of heavy holes to light holes. Piezoresistance in semiconductor functions by altering this proportion with the application of stress. When an anisotropic stress is applied across the semiconductor, the lattice spacing increases in one direction while the lattice spacing decreases in the perpendicular direction. As one might expect, the interaction of the charge carriers with the lattice is also affected. The stress causes the holes to move from the heavy-hole band to the light-hole band or vice versa, depending on the direction the stress is applied. Since the ratio of heavy-hole to light-holes is altered, the average effective mass of all the holes changes, and, therefore, the mobility and the resistivity changes. This is the piezoresistive effect in silicon.

Recall that the tightness of the band parabola is directly related to the hole effective mass. As is apparent in Figure 4.7, the difference in curvature and therefore the difference in effective mass is much larger in the [111] direction than in the [100] direction. Therefore, when stress is applied to the silicon, the holes redistribute themselves among the heavy-hole and light-hole bands. The effect of this redistribution on the resistivity is small in the case of the [100] directions but quite large for the [111] directions. Therefore, piezoresistors in p-type silicon are aligned in the [111] directions.

The gauge factor of p-type silicon is positive. This means that a positive strain (elongation) causes the band with the lowest mass and highest mobility to lower with respect to the low mobility band, so that the holes move to the low mobility band. As a result, more holes have a lower mobility and the resistivity increases, which leads to the experimentally observed positive piezoresistive effect.

Figure 4.8 shows how the gauge factor G depends on the temperature and the doping level. Similar to n-type material, the gauge factor decreases for increasing doping concentration and higher temperature. Both effects can be explained by the fact that when fewer holes distribute themselves over the two bands, the relative change is larger. As can be seen in Figure 4.8, the gauge factor is significantly smaller in more heavily doped material, but it is much more stable with temperature. Therefore, in industrial silicon processing, the silicon is heavily doped to produce degenerately piezoresistive sensors. A little sensitivity in the magnitude of the output of the sensor is lost in order to create a sensor whose output is much more temperature stable. The loss of sensitivity can be made up by carefully designing the diaphragm that is located below the piezoresistor to maximize the output.
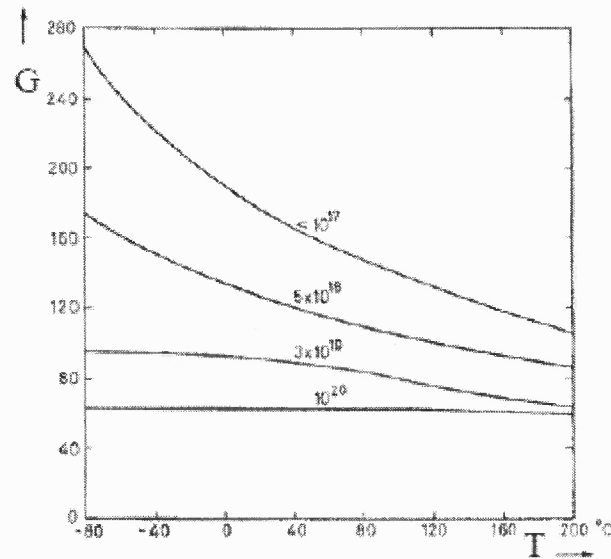
Figure 4.8 Gauge factor of p-type silicon as a function of temperature and doping concentration [30].

4.2.4 Sensing Elements and Gauge Factor Measurement

In order to measure the piezoresistance coefficients, the change in resistivity must be measured under a known applied stress or strain. Smith's original measurement of the piezoresistance of silicon involved a basic, uniaxial tension system [33].

For the measurement of strain in an object, the strain gauge is bonded to the object, which in the case of a pressure sensor, is usually a diaphragm. When a load (pressure) is applied, both the diaphragm and the strain gauge deform, causing the resistance of the strain gauge to change.

As shown in Table 4.3, the π_{11} coefficient has the largest magnitude (-102.2) for n-type silicon, meaning that n-type mono-crystalline silicon exhibits the greatest piezoresistive sensitivity in the direction of principle stress. For the same material, the shear piezoresistance factor (-13.6) is least sensitive to axial tension and would not have a significant effect on the piezoresistive output. For p-type silicon, on the other hand, the

shear coefficient is greatest (+138.1). Similar trends are observed in more heavily doped silicon.

Table 4.3 Piezoresistive coefficients of silicon, given in 10^{-11} Pa^{-1} [49]

Type	Resistivity	π_{11}	π_{21}	π_{44}
Units	(Ω. cm)	10^{-11} Pa^{-1}	10^{-11} Pa^{-1}	10^{-11} Pa^{-1}
n-type	+ 11.7	- 102.2	+ 53.4	- 13.6
p-type	+ 7.8	+6.6	-1.12	+138.1

Higher gauge factor means higher output for the same strain, or higher sensitivity relative to the stiffness and natural frequency of the structure. The change in electrical resistance of a strain gauge with the application of a physical stress is referred to as the piezoresistive effect.

An important tool for accurate measurement or application of the piezoresistive behavior of silicon is the Wheatstone bridge circuit where one, two or four piezoresistive elements can be subjected to a strain, while the remaining elements are unstrained, (Figure 4.9).
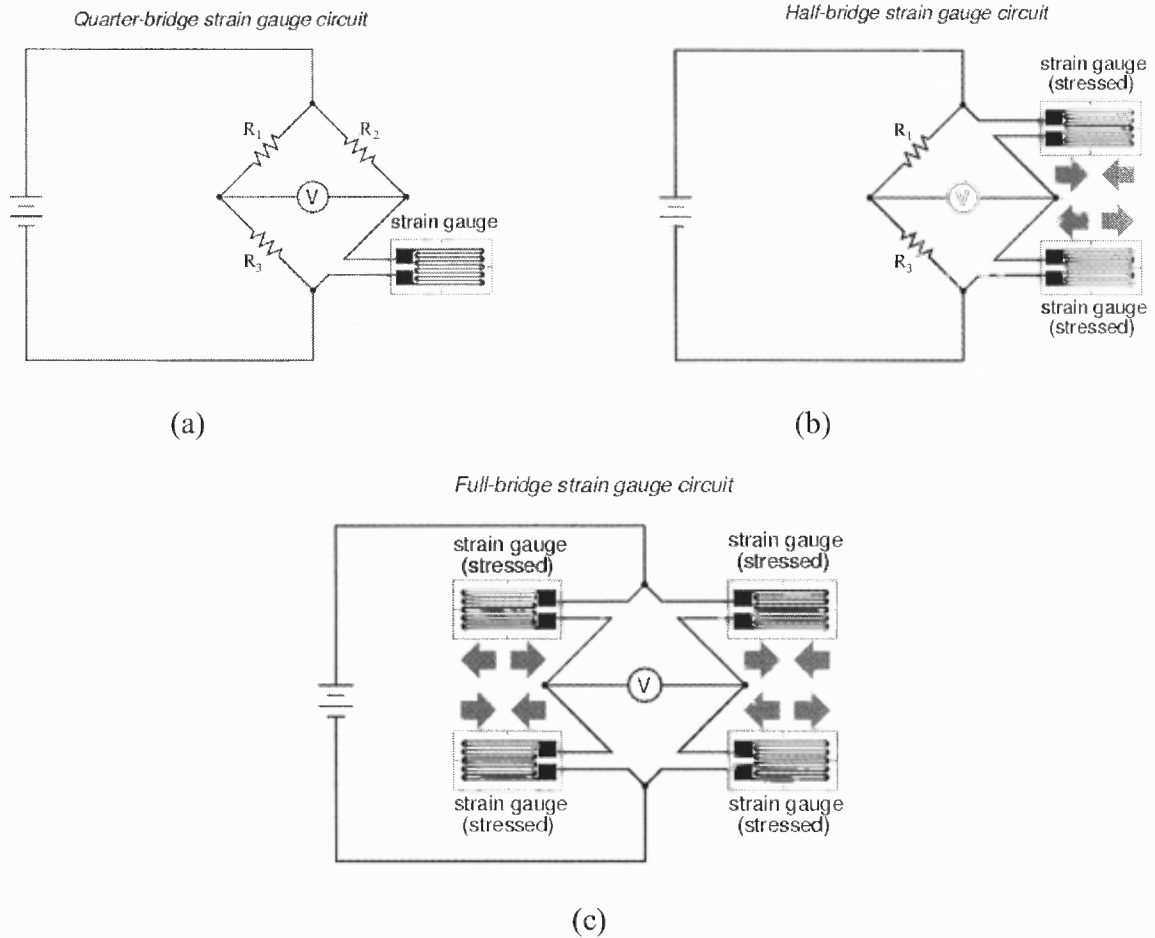
Figure 4.9 Wheatstone bridge configurations; a- Quarter bridge circuit; b- Half bridge circuit; c- Full-bridge circuit [67].

4.2.5 Wheatstone Bridge (WB) Circuit

The popularity of the WB circuit is due to the fact that it converts the strain-induced resistance of the gate to voltage change which can be measured directly and accurately with conventional instruments. Also, it has the ability to compensate for temperature variations.

The Wheatstone bridge is normally energized by applying a regulated voltage across two opposite corners. A voltage output proportional to the product of the excitation voltage and the resistance change of the strain gauge appears across the signal terminals. For conventional wire and foil gauges, the signal level is measured in terms of

a few tens of millivolts whereas semiconductor strain gauges typically produce signals of several hundreds of millivolts.

It is advantageous to make all four elements of the bridge active (changes resistance with strain) not only for its greater sensitivity, also because it is linear while the other configurations are not. A full bridge configuration uses four active gauges to make strain measurements. Whenever possible, the two adjacent arms of the bridge should change equally but in opposite directions under strain. This will eliminate temperature induced changes from the output voltage. This condition is achieved, for example, in the special case of a fully active Wheatstone bridge circuit where the tension gauges and the compression gauges, are equal.
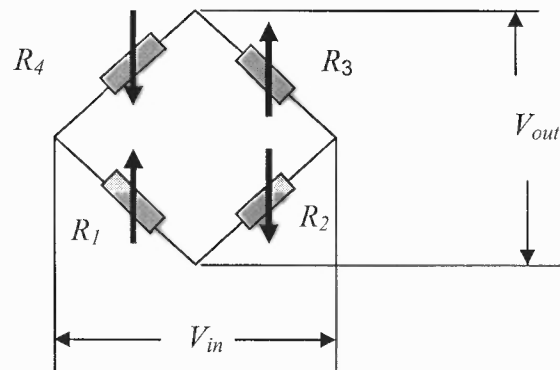
Figure 4.10 Wheatstone bridge.

The output voltage is related to the four resistors and the excitation voltage. From Kirchhoff's voltage law and Ohm's law applied to the circuit (Figure 4.10), it can be shown that $V_{out} = V_{R1} - V_{R4}$ resulting in:

$$\frac{V_{out}}{V_{in}} = \frac{R_1}{R_1 + R_2} - \frac{R_4}{R_3 + R_4} \tag{4.26}$$

Note that when the voltage output is zero, the bridge is said to be balanced. It is not required that $R_1 = R_4$ and $R_2 = R_3$ to achieve balance. Likewise, any change in resistance in any leg of the bridge will unbalance the bridge and produce a non-zero output voltage.

Figure 4.11 illustrates some of the compensation techniques applied to Wheatstone bridge circuits, which makes it possible to design the pressure sensor requirement to specific applications.
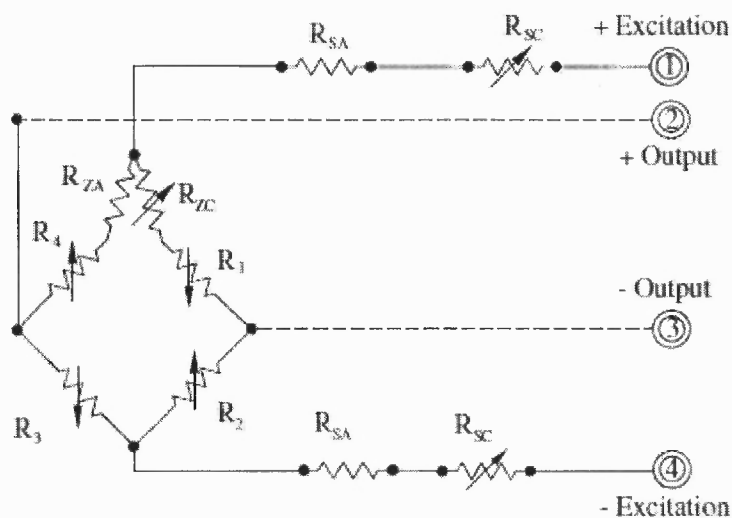
R_{ZA} Zero balance adjustment

R_{ZC} Compensation for thermal zero shift

R_{SA} Sensitivity adjustment

R_{SC} Compenstation for thermal sensitivity shift

Figure 4.11 Compensation techniques applied to Wheatstone bridge circuits [68].

4.3 Sensor Fabrication

The basic structure of a piezoresistive pressure sensor consists of four sensor elements in a Wheatstone bridge configuration that measure stress within a thin crystalline silicon membrane. The stress is a direct consequence of the membrane deflecting in response to an applied pressure differential across the front and back sides of the sensor. The stress is, to a first order approximation, linearly proportional to the applied pressure differential. The membrane deflection is typically less than one micrometer. The output, at full-scale applied pressure, is a few millivolts per volt of bridge excitation (the supply voltage to the bridge).

The thickness and geometrical dimensions of the membrane affect the sensitivity and, consequently, the pressure range of the sensor.

Piezoresistive pressure sensors are easy to fabricate and do not require any complicated electronics. There are two main elements of the current generation of devices which will be given special consideration: the production of a suitable deflecting diaphragm to convert applied pressure into displacement (described in the previous chapter) and the addition of piezoresistive strain gauge elements to the diaphragm to record the displacement.

Figure 4.12 illustrates an example of fabrication steps for a piezoresistive, gauge, or differential bulk micromachined pressure sensor [49]. The fabrication process of a typical pressure sensor relies mostly on steps standard to the integrated circuit industry, with the exception of the precise formation of the thin membrane using electrochemical etching. An n-type epitaxial layer of silicon is grown on a p-type, (100) wafer. A thin, preferably stress-free, insulating layer is deposited or grown on the front side of the

wafer, and a protective silicon nitride film is deposited on the back side. The piezoresistive sensing elements are formed by locally doping the silicon p-type using the masked implantation of boron, followed by a high-temperature diffusion cycle. Etching of the insulator on the front side provides contact openings to the underlying piezoresistors. A metal layer, typically aluminum, is then sputter deposited and patterned in the shape of electrical conductors and bond pads. A square opening is patterned and etched in the silicon nitride layer on the back side. Double-sided lithography ensures that the backside square is precisely aligned to the sense elements on the front side. At this point, electrical contacts are made to the p-type substrate and n-type epitaxial layer, and the silicon is electrochemically etched from the back side in a solution of potassium hydroxide. Naturally, the front side must be protected during the etch. One practical protection method includes coating with wax such as paraffin and clamping in a fixture. The etch stops as soon as the p-type silicon is completely removed, and the n-type layer is exposed. The process forms a membrane with precise thickness defined by the epitaxial layer. Anodic bonding in vacuum of a Pyrex glass wafer on the back side produces an absolute pressure sensor that measures the pressure on the front side in reference to the cavity pressure (often, vacuum). For differential- or gauge-type pressure sensors, previously drilled holes in the glass wafer provide vent ports.

Insulator

N-type epitaxial layer

P-type substrate

Silicon nitride

Deposit insulator

P-type diffusions

Diffuse piezoresistors

Metal

Deposit and
pattern metal

Electrochemical
etch of backside
cavity

Anodic bond
of glass

Glass
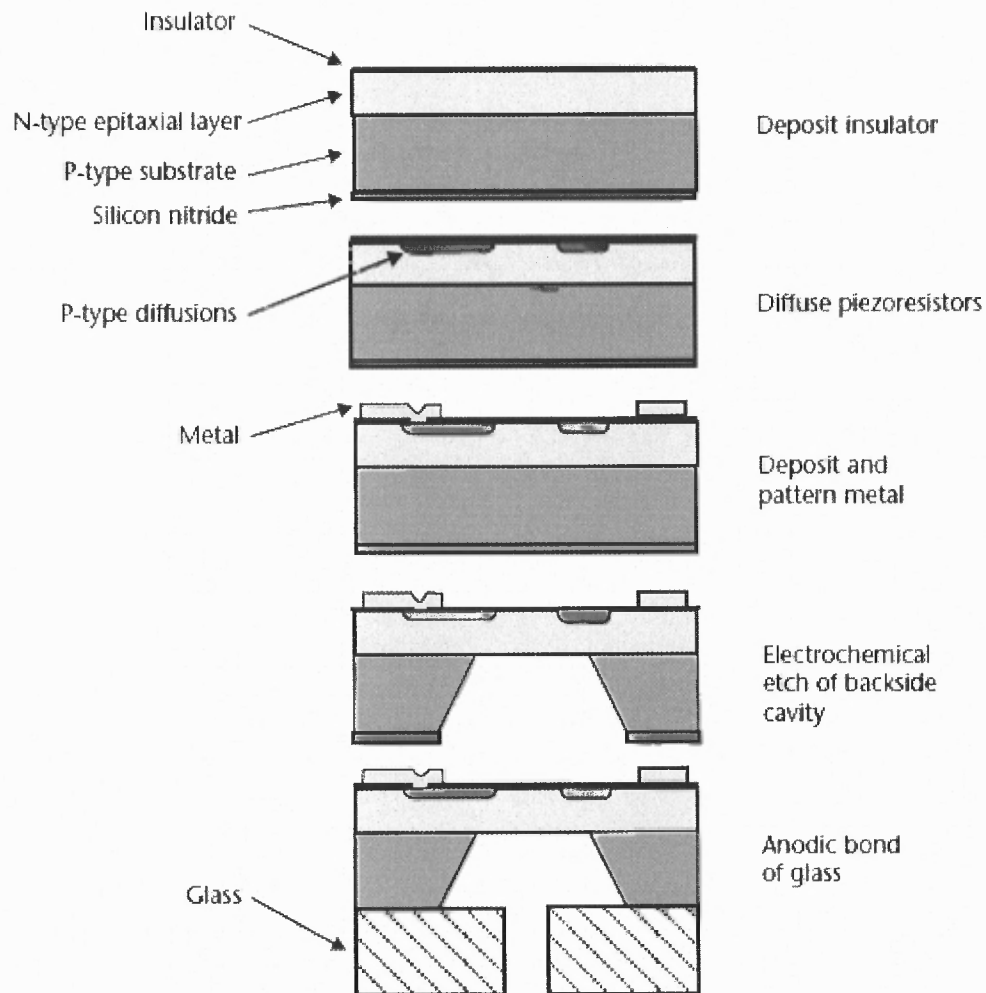
Figure 4.12 Manufacturing process for piezoresistive chip [49].

Conventional piezoresistive pressure sensors are fabricated by implanting p-type resistors on n-type membranes. This technology suffers from the disadvantage that the p-n junction isolation of piezoresistors becomes leaky at temperatures higher than 100 °C. This problem has been solved by fabricating the pressure sensors on silicon-on- insulator (SOI) wafers [69], since the oxide isolation between piezoresistors can withstand high temperatures.

Polysilicon has been used as a piezoresistive material because of the advantage that the temperature coefficient of resistivity (TCR) can be made zero by suitably adjusting the doping concentration. However, the sensitivity of polysilicon piezoresistive pressure sensors is always lower than that of single crystal silicon piezoresistive pressure sensors because of the lower gauge factor of polysilicon compared to that of single crystal silicon.

The piezoresistors are formed within the silicon diaphragm by either diffusion or implantation of atoms from the third atomic group (e.g. phosphorus which produces an n-type semiconductor) or the fifth atomic group (e.g. boron which produces a p-type semiconductor). By the use of photolithographic techniques, typically four elongated piezoresistors are created. Two of these resistors are positioned on the silicon diaphragm such that they experience a compressive strain and two are positioned where they experience a tensile strain. They are then connected together electrically to form a fully active Wheatstone bridge.

One company, Kulite Semiconductor Products [44] has developed and patented a variation to the integrated diffused sensor design (Figure 4.13) in which the four piezoresistive gauges are molecularly bonded to a micromachined silicon diaphragm with an insulating layer of silicon dioxide between. This technology is referred to as either "silicon on silicon", "silicon on insulator" or "dielectrically isolated silicon strain gauges". In diffused silicon sensors, the piezoresistors are electrically isolated from one another and the substrate by reverse-biased p-n junctions which leak current at high temperatures. Dielectric isolation, however, allows for operation at much higher temperatures. This single development has resulted in the extension of the maximum

operating temperature capability from 150°C up to 540°C, an incredible improvement in the performance in one step. Kulite's capability to design, manufacture and package ultra high temperature piezoresistive pressure transducers is still unmatched even two decades after its first implementation.
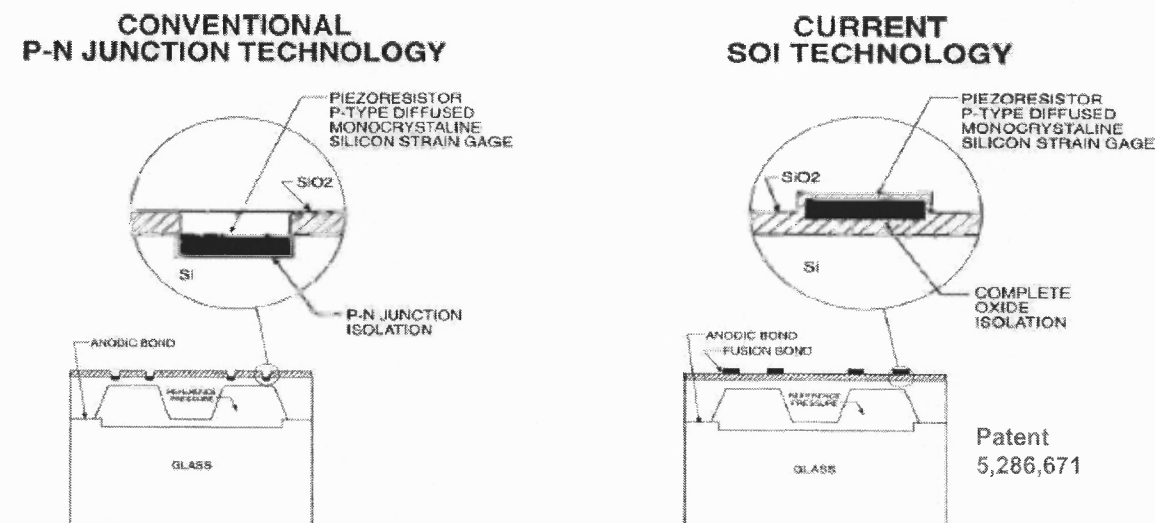
Figure 4.13 Pressure sensor technologies [70].

CHAPTER 5

FABRY-PEROT PRESSURE SENSORS

5.1 Fabry- Perot Interferometer

The Fabry-Perot interferometer is a relatively simple optical device that is based on the interference of multiple beams of coherent radiation. It consists of two parallel partially transmitting mirrors that form a reflective cavity. Incident light enters the Fabry-Perot cavity and experiences multiple reflections between the mirrors so that the light can produce multiple interferences.

5.1.1 Historical Perspective

Charles Fabry and Alfred Perot of the University of Marseilles in 1897 described a novel device named later as the Fabry-Perot interferometer or etalon, which made use of interference phenomena in waves successively reflected between two thinly silvered plane glass plates set in parallel. They developed the underlying principles, described several constructive interference instruments, introduced and evaluated experimental methods and techniques, and illustrated the potential application with methodical measurements. It should be noted that this section is a resume of the historical overviews compiled by Hernandez and Vaughan, references there in [71, 72].

Fabry and Perot measured the viscosity effects of air, and then fabricated an electrostatic voltmeter in 1898. In 1899, they published four papers on their work on interference, where they included: I. Fringes from silvered plates; II. Phenomena produced when the incident light is composed of two monochromatic radiations; III.

81

Application to spectroscopy; IV. Determination of the order of a fringe; V. Comparison of wavelength; and VI. Measurement of length.

In 1902, Fabry and Perot presented their paper, "Measurements of absolute wavelength in the solar spectrum and in the spectrum of iron", where techniques of wavelength measurement were discussed in detail.

In 1912, Buisson and Fabry made use of the Fabry–Perot interferometer to test the kinetic theory of gases by detecting the temperature broadening of the emission lines of gases, Doppler broadening, and then measuring the wavelength shift of the bulk motion of the emitters.

Further uses of Fabry-Perot interferometry include the Zeeman effect (Zeeman 1908, Nagaoka and Takamine 1915), the index of refraction of gases (Meggers and Peters, 1918), and isotropic and fine structure investigations (Nagaoka, 1917, Strutt 1919, Merton 1920).

The two reviews by Meissener (1941-1942) consolidated the spectroscopic aspect of the Fabry-Perot, coupled with the appearance of Talansky's (1947) book on high resolution instruments, their construction, alignment and care, and set the stage for the next advances in the field of high-resolution spectroscopy.

The range of the utilization of Fabry-Perot interferometry has been extended into the vacuum ultraviolet down to 138 nm (Bideau-Mehu, 1976, 1980), and X-ray operation of the device has been proposed (Steyerl and Steinhauser, 1979).

The time measurement method to determine the Fabry-Perot maxima by Pole and collaborators (1978, 1980), and the matched-etalon camera concept of Young and Clark (1980) are other examples.

Currently, the use of Fabry-Perot devices in laboratories and their applications have made possible the growth of disciplines such as geophysics, astronomy, astrophysics and laser spectroscopy.

5.1.2 Fabry-Perot Interferometer Sensors (FPIS)

The Fabry-Perot interferometry is one of the most popular amongst several optical techniques that are available for the fabrication of optical sensors, because it provides numerous advantages over conventional sensors such as high degree of sensitivity, high accuracy, capabilities for signal "amplification," immunity to electromagnetic interference, ability to respond to a wide variety of measurements, small size and survivability in harsh environment.

A Fabry-Perot interferometer sensor is a typical multiple-beam interferometer. It consists generally of a single mode fiber surface and a sensing element surface (generally the same fiber, a different fiber or a diaphragm). The spatial separation between two surfaces is called the cavity length. The reflected light is wavelength modulated in exact accordance with the cavity length. It can be used in various sensitive applications such as measurements of velocity [73], displacement [74-77], and temperature [78, 79].

5.1.3 Intrinsic (IPFI) and Extrinsic (EFPI) Sensors

Fabry-Perot interferometer sensors can be classified into two types, the intrinsic Fabry-Perot interferometer sensor, and the extrinsic Fabry-Perot interferometer sensor, In IFPI sensor, the optical waves in the fiber are affected directly by the incident perturbation, and changes in the output intensity give an indication of the magnitude of the disturbance. Usually, the Fabry-Perot cavity is formed by placing a segment of a single

mode fiber that has both end faces coated with a semi-transparent reflective coating on one of the output arms of the coupler (Figure 5.1, a) [80-82]. The signals that form the interference patterns are reflected from the two ends of this fused fiber segment. In IFPIS, the sensing element can be fabricated by several methods such as with dielectric thin-films [83], fiber Bragg gratings [84], or UV-induced mirrors [85].

In EFPI sensor, the performance of the device should be independent of the fiber and depend only on the nature of the sensing element; therefore, it offers the flexibility to design the Fabry-Perot cavity to accommodate various applications. The fiber acts just as a medium to transmit light into and out of the cavity. The cavity of an extrinsic Fabry-Perot interferometer can be formed by placing two optical fibers in an alignment tube separated by an air gap (Figure 5.1, b) [86-88], or with the introduction of Fabry-Perot diaphragm based sensor consisting of a single mode fiber surface and a diaphragm surface as the sensing element (Figure 5.1, c) [89].

cavity length

Thin film

(a)

gauge length

cavity length

airgap

lead-in fiber

target fiber

thermal fusion bonding

(b)

Optical
Fiber

Bonding Points

Light

Capillary Tubing

Diaphragm

(c)
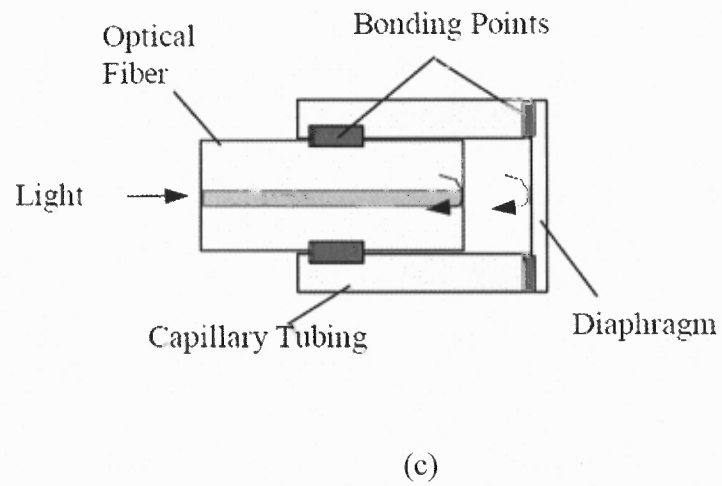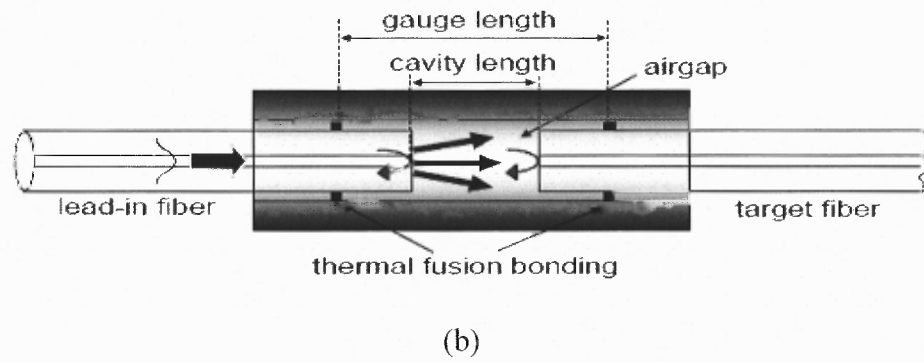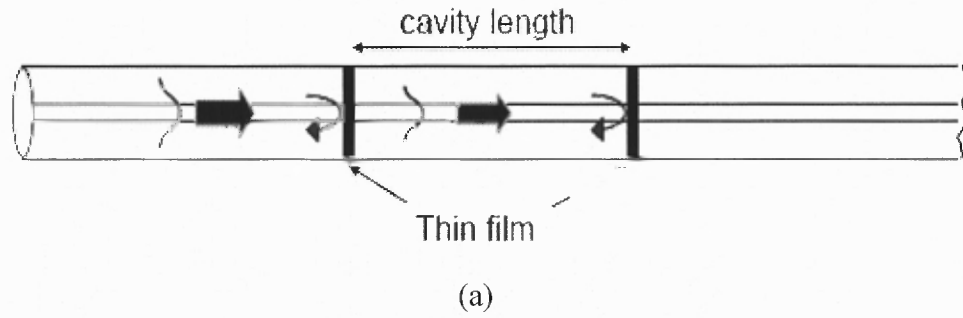
Figure 5.1 Fabry-Perot Interferometer Sensor: a- instrinsic, b- extrinsic c- diaphragm based [86-88].

5.2 EFPI Diaphragm-Based Sensor

The EFPI diaphragm based sensor cavity is the type studied in this dissertation. The cavity is created between the end face of a fiber tip and the surface of the diaphragm. When a pressure is applied on the diaphragm, the Fabry-Perot cavity length will change because of the deflection of the diaphragm. There is a direct correlation between the absolute reflectance produced by the sensor and the deflection of the silicon diaphragm. When the silicon diaphragm is deflected, the optical path difference in the Fabry-Perot cavity will change.

5.2.1 EFPI Diaphragm Based Sensor Theory

The use of Fabry-Perot as a sensor is related to the design of a Fabry-Perot cavity between the sensing element (diaphragm) and the fiber tip. The analysis is similar to a homogeneous dielectric film situated between two homogeneous media, where the media are the diaphragm material, glass and the air as a dielectric.

A thorough analysis of this case is presented by Max Born and Emil Wolf in their book "Principles of Optics" [90]. According to this reference, the reflectivity R is given by:

$$R = |r|^2 = \frac{R_1 + R_2 + 2R_1R_2 \cos(2\delta)}{1 + R_1^2 R_2^2 + 2R_1R_2 \cos(2\delta)} \tag{5.1}$$

The intensity of the reflected radiation I_r is given by:

$$I_r = I_i \left(\frac{R_1 + R_2 + 2\sqrt{R_1R_2} \cos(\delta)}{1 + R_1R_2 + 2\sqrt{R_1R_2} \cos(\delta)}\right) \tag{5.2}$$

where, δ is the phase delay between two partial waves, r is the reflection coefficient of the cavity, I_i and I_r are intensities of the incident and reflected beam from the Fabry-Perot

cavity, R_1 and R_2 are the coefficients associated with the reflection at the first and second surface respectively.
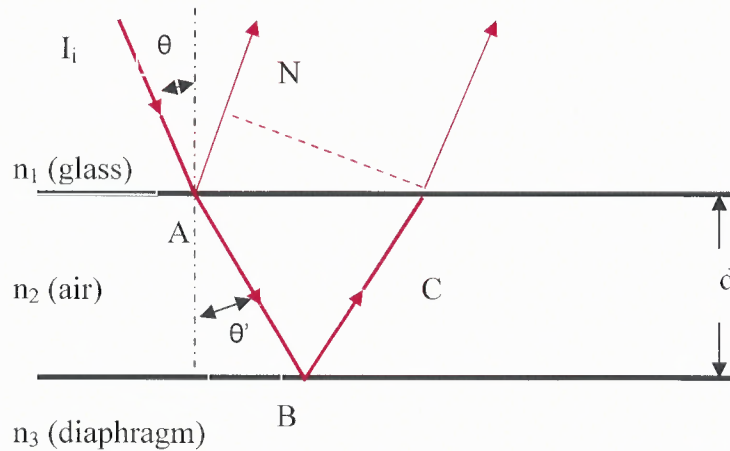
Figure 5.2 Optical path difference between two successive reflections.

The difference in the optical paths between two reflected beams is (Figure 5.2):

$$\Delta S = n_2 (AB + BC) - n_1 AN$$

$$AB = BC = \frac{d}{\cos \theta'}$$

$$AN = AC \sin(\theta) = 2d \tan \theta' \sin \theta$$

$$n_2 \sin \theta' = n_1 \sin \theta$$

Combining the above equations, $\Delta S = 2n_2 d \cos \theta'$ and the corresponding phase delay δ between two partial waves is given by [91]:

$$\delta = \frac{2\pi(\Delta S)}{\lambda} = \frac{4\pi n_2 d \cos \theta'}{\lambda} \tag{5.3}$$

where d is the separation between the two surfaces.

$R_1 = \left| r_{12} \right|^2$, $R_2 = \left| r_{23} \right|^2$ are the coefficients associated with the reflection at the first and second interface, respectively.

Assuming perpendicular incidence, $r_{12} = \dfrac{n_1 - n_2}{n_1 + n_2}$ and $r_{23} = \dfrac{n_2 - n_3}{n_2 + n_3}$ where n_1, n_2, and, n_3 are the refractive index of the glass, air and diaphragm, respectively.

An alternative derivation of Equation 5.2 will be presented following the multiple beam interference analysis. Let I_i be the amplitude of the vector of the incident wave, assumed to be linearly polarized, with the electric vector either parallel or perpendicular to the plane of incidence. Amplitude I_i is taken to be complex, with its phase equal to the constant part of the phase of the wave function. For each member of either the reflected or the transmitted set of waves, the variable part of the phase of the wave function differs from that of the preceding member by an amount which corresponds to a double transversal across the cavity gap d. This phase difference is given by Equation 5.3.

For a wave traveling from the fiber (glass) into the Fabry-Perot cavity, let r_{12} be the reflection coefficient (ratio of the reflected and incident amplitudes) and t_1 the transmission coefficient (ratio of transmitted and incident amplitudes) of the glass-air interface, and let r_{23} and t_2 be the corresponding coefficients for the air-diaphragm interface.
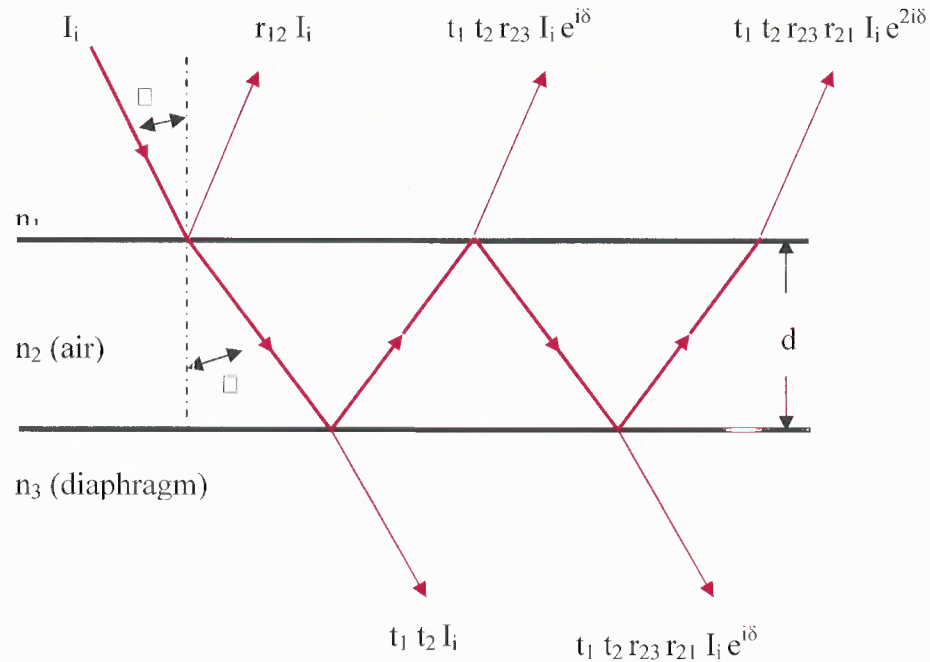
Figure 5.3 Reflection and transmission of a plane wave in Fabry-Perot cavity (plane-parallel plate).

The complex amplitudes of the waves reflected from the fiber surface are:

$r_{12} I_i,$ $t_1 t_2 r_{23} I_i e^{i\delta},$ $t_1 t_2 r^2_{23} r_{21} I_i e^{2i\delta}, \ldots$, $t_1 t_2 r^{(p-1)}_{23} r^{(p-2)}_{21} I_i e^{i(p-1)\delta}$ (Figure 5.3)

For the first p reflected waves, the amplitude $I_r (p)$ of the electric vector of the reflected light is given by the expression:

$$I_r (p) = I_i [r_{12} + t_1 t_2 r_{23} e^{i\delta} + t_1 t_2 r_{21} r^2_{23} e^{2i\delta} + \ldots t_1 t_2 r^{(p-2)}_{21} r^{(p-1)}_{23} e^{i(p-2)\delta}]$$

$$I_r (p) = I_i [r_{12} + t_1 t_2 r_{23} e^{i\delta} (1 + r_{21} r_{23} e^{i\delta} + \ldots r^{(p-2)}_{21} r^{(p-2)}_{23} e^{i(p-2)\delta})]$$

$$I_r (p) = I_i [r_{12} + t_1 t_2 r_{23} e^{i\delta} \sum_{n=0}^{(p-2)} r^{(n)}_{21} r^{(n)}_{23} e^{in\delta}]$$

$$I_r (p) = I_i [r_{12} + t_1 t_2 r_{23} e^{i\delta} (\frac{1 - r^{(p-1)}_{21} r^{(p-1)}_{23} e^{i(p-1)\delta}}{1 - r_{21} r_{23} e^{i\delta}})]$$

Substituting $r_{12} = - r_{21}$, and let $p \rightarrow \infty$, one obtains:

$$I_r = I_i \left[r_{12} + \frac{t_1 t_2 r_{23} e^{i\delta}}{1 + r_{12} r_{23} e^{i\delta}} \right] = I_i \left[\frac{r_{12} + r_{12}^2 r_{23} e^{i\delta} + t_1 t_2 r_{23} e^{i\delta}}{1 + r_{12} r_{23} e^{i\delta}} \right]$$

$$I_r = I_i \left[\frac{r_{12} + r_{23} e^{i\delta} (r_{12}^2 + t_1 t_2)}{1 + r_{12} r_{23} e^{i\delta}} \right]$$

Since there is no absorption, $r_{12}^2 + t_1 t_2 = 1$. Also $r_{12} = \sqrt{R_1}$ and $r_{23} = \sqrt{R_2}$

$$I_r = I_i \left(\frac{\sqrt{R_1} + \sqrt{R_2} e^{i\delta}}{1 + \sqrt{R_1} \sqrt{R_2} e^{i\delta}} \right)$$

$$I_r = I_i \left(\frac{R_1 + R_2 + 2\sqrt{R_1 R_2} \cos(\delta)}{1 + R_1 R_2 + 2\sqrt{R_1 R_2} \cos(\delta)} \right)$$

which is the same as Equation 5.2. But, $\cos(\delta) = 1 - 2\sin^2\left(\frac{\delta}{2}\right)$, so one has

$$I_r = I_i \left(\frac{R_1 + R_2 + 2\sqrt{R_1 R_2} - 4\sqrt{R_1 R_2} \sin^2\left(\frac{\delta}{2}\right)}{1 + R_1 R_2 + 2\sqrt{R_1 R_2} - 4\sqrt{R_1 R_2} \sin^2\left(\frac{\delta}{2}\right)} \right)$$

$$I_r = I_i \left[\frac{(\sqrt{R_1} + \sqrt{R_2})^2 - 4\sqrt{R_1 R_2} \sin^2\left(\frac{\delta}{2}\right)}{(1 + \sqrt{R_1 R_2})^2 - 4\sqrt{R_1 R_2} \sin^2\left(\frac{\delta}{2}\right)} \right]$$

Finally, for perpendicular incidence one has $\delta = \dfrac{4\pi n_2 d}{\lambda}$ and

$$I_r = I_i \left[\frac{(\sqrt{R_1} + \sqrt{R_2})^2 - 4\sqrt{R_1 R_2} \sin^2\left(\frac{2\pi n_2 d}{\lambda}\right)}{(1 + \sqrt{R_1 R_2})^2 - 4\sqrt{R_1 R_2} \sin^2\left(\frac{2\pi n_2 d}{\lambda}\right)} \right] \qquad (5.4)$$

5.2.2 EFPI Sensor Applications

In an extrinsic Fabry-Perot interferometeric sensor, the detected intensity is modulated by the parameter under measurement. These sensors have been implemented for the measurement of strain [77, 92, 93], temperature [94, 95], magnetic field [96], chemical composition [97-99], biological parameters [100], medical applications [101, 102], acoustic detection [103-106], vibration mode analysis in smart structures [107, 108], and pressure, which will be analyzed in the following section.

5.3   EFPI as a Pressure Sensor

The Fabry-Perot optical pressure sensor has recently been introduced as an alternative to conventional piezoresistive and capacitive pressure sensors to eliminate signal degradation in harsh environments. In addition, piezoresistive pressure sensors show non-linear sensitivity at elevated temperatures, and capacitive pressure sensors produce fairly small output capacitance. While a micromachined Fabry-Perot pressure sensor enjoys advantages over counterparts, its commercialization is still in an early stage of maturity.

Fabry-Perot optical pressure sensors have been the most heavily studied transduction method for optical sensing. The device requires two partially reflective surfaces, one of which deflects with applied pressure. The deflection causes a modulation of the distance, d, between the two reflective surfaces. When optical waves of a single wavelength are incident upon the first surface, a fraction will reflect and the rest will pass through to the second surface. At the second interface, a portion of the light will reflect again. If the distance, d, is such that $2d \sin \theta = n\lambda$, the waves reflected from the second surface will be in phase with the first reflected waves and the returning light will have a

maximum intensity. If the membrane deflects by $\lambda/4$, the two reflected waves will be π radians out of phase and a corresponding minimum in intensity will be detected.

5.3.1 EFPI Diaphragm Based Pressure Sensor System.

An EFPI sensor system (Figure 5.4) is formed by a laser as a source, a three-way directional optical coupler (circulator) to allow the light to go in/out of the sensor, a photodiode to convert the optical output into an electrical output and to be processed. The EFPI sensor components are interconnected by optical fiber light guides, which can be multimode or single mode fiber.
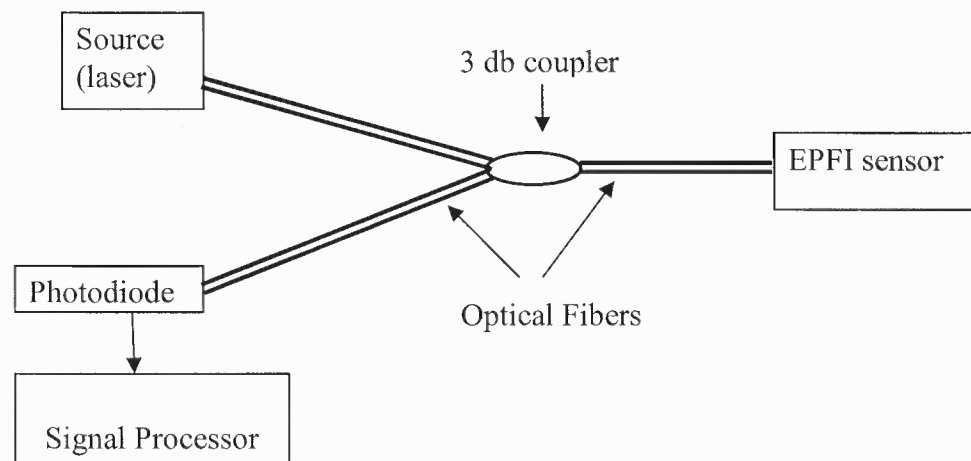
Figure 5.4 EFPI diaphragm based pressure sensor.

5.3.2 Review of EFPI Diaphragm-Based Pressure Sensor Designs

EFPI diaphragm-based pressure sensors configurations are more suitable for pressure measurements requiring high sensitivity when compared to the other types of FPI sensors.

The classic configuration (Figure 5.5) of EFPI diaphragm based pressure sensor is the use of a flat diaphragm as the sensing element and one of the two parallel surfaces of the Fabry-Perot cavity [98, 105, 109, 110].
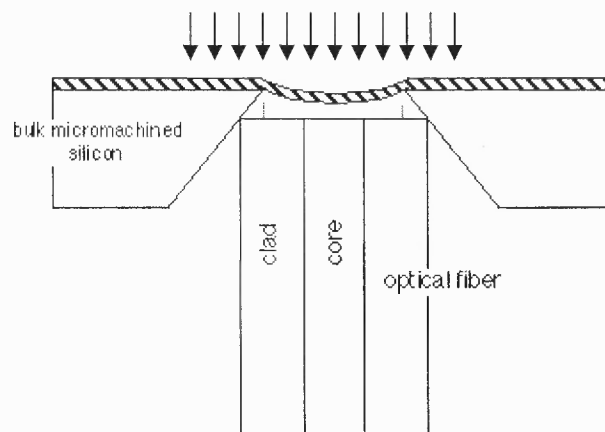
Figure 5.5 Classical configuration of an EFPI diaphragm based pressure sensor [111].

The major obstacles of classical configurations of EFPI diaphragm-based pressure sensor is the so-called signal averaging effect arising from non-flatness of the diaphragm under applied pressure [112]. Therefore, it is important to develop a performance-enhanced diaphragm structure to minimize the non-flatness of the deflected diaphragm. On the other hand, temperature dependence has been a weakness of Fabry-Perot cavity-based pressure sensors with a conventional flat diaphragm since stresses are caused by the mismatch in coefficients of thermal expansion of materials.

One of the proposed solutions is the introduction of a single deeply corrugated diaphragm (SDCD), which consists of a flat bottom-region that is suspended all around with free-sidewalls (Figure 5.6) [105]. This produces a miniature FP cavity-based pressure sensor that enhances the flatness of the diaphragm under pressurized deflection. The signal averaging effect is reduced by the flat bottom and the free-space sidewalls [105]. It has also been suggested that a corrugated diaphragm is capable of reducing the influence of packaging and thermally induced stress of a mechanical sensor.
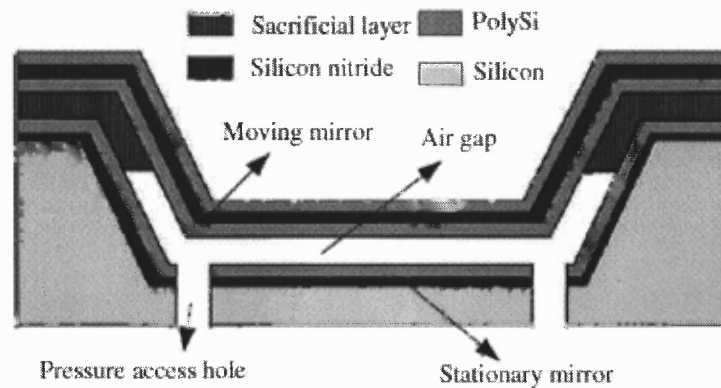
Figure 5.6 Single deeply corrugated diaphragm Fabry-Perot microcavity [113].

Although the proposed design has some advantages compared to the flat diaphragm, a few problems remain which are related to the EFPI diaphragm based pressure sensor, particularly in the alignment of an optical fiber at the center of the deflecting diaphragm. In Chapter Six, a novel design of an EFPI diaphragm based pressure sensor with the introduction of the embossed diaphragm or rigid body is shown to solve all the deficiencies that exist in previous EFPI diaphragm based sensors.

CHAPTER 6

INTEGRATED ELECTRONIC AND OPTICAL PRESSURE SENSOR

The integrated electronic and optical pressure sensor (IEOPS) combines two principles of measurements into one integrated unit with optical and electronic parts to detect movement of the sensing element, which is an embossed (or rigid body) diaphragm used as the sensing element of both integrated parts (Figure 6.1). The optical part of the sensor is based on a Fabry-Perot cavity and the electronic part of the sensor is based on the piezoresistive effect [114, 115].

In the application of Fabry-Perot interferometry, the sensing element utilizes an optical cavity where interference of multiple reflections change with movement of cavity surfaces caused by pressure, sound, chemical reaction or biological activities.

In the application of the piezoresistive effect, a change in the electrical resistivity of a sensor material is caused by the application of mechanical stress, which is detected, for example, by a Wheatstone bridge circuit.

The electronic part of the sensor, which is a piezoresistive based sensor, is fabricated with silicon piezoresistors connected in a Wheatstone bridge configuration. The optical part of the sensor, which is a Fabry-Perot based sensor, contains an optical cavity formed by the center rigid body and a single mode fiber.

The embossed diaphragm together with MEMS technology allows minimizing the Fabry-Perot gap between the diaphragm and the fiber, and thus avoiding misalignment between the fiber and the diaphragm as well as minimizing the back pressure within the cavity (See Section 6.3).

Fiber

Si Diaphragm

Glass

Pressure
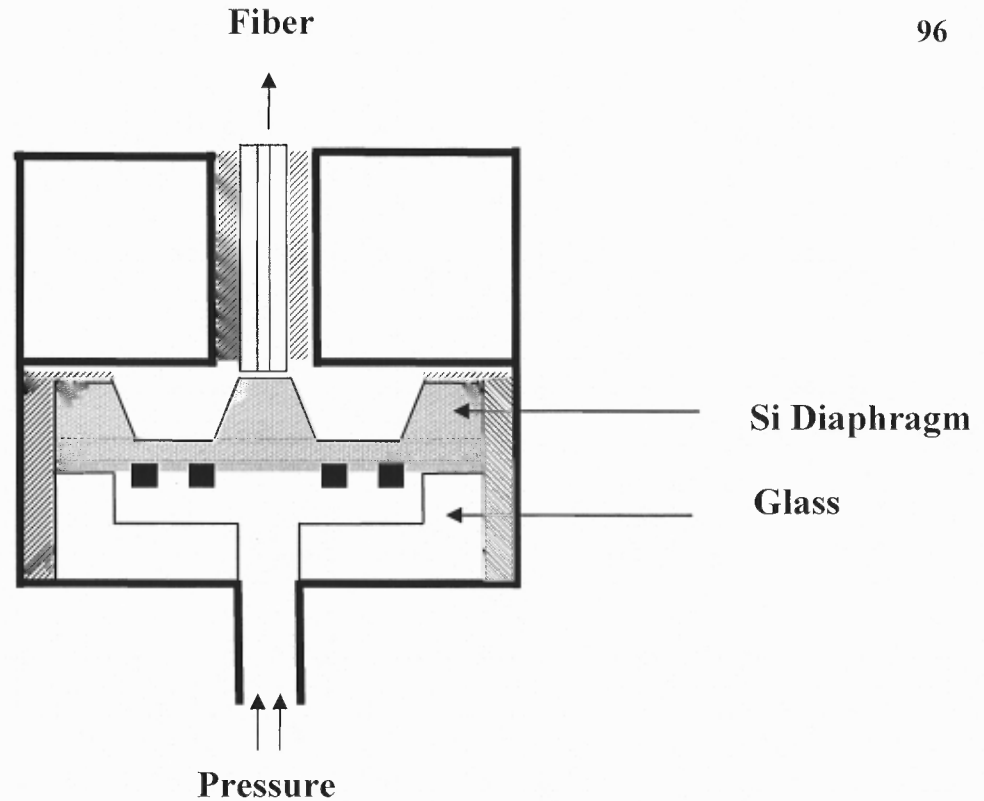
Figure 6.1 Sensor configuration of an IEOPS.

The output signals from both parts of the sensor can be used independently of each other, as verification of the measured magnitude, and as a mechanism of back-up in continuous monitoring systems.

The signal output obtained from the electronic part of the sensor can be used as a reference to establish the quiescence point (Q-point) of the signal output from the optical part of the sensor. A method of making Fabry-Perot cavities, to be used in the Fabry-Perot interferometer diaphragm-based pressure sensor in conjunction with the assistance of the piezoresistive part of the sensor, is described in sub-section 6.4.1.

6.1 Piezoresistive Sensor Design

The electronic part of the sensor, which is a piezoresistive based sensor, is designed with p-type doped silicon piezoresistors in a Wheatstone bridge (Figure 6.2). It is used to convert mechanical stress of the bossed diaphragm into an electrical output signal [10].
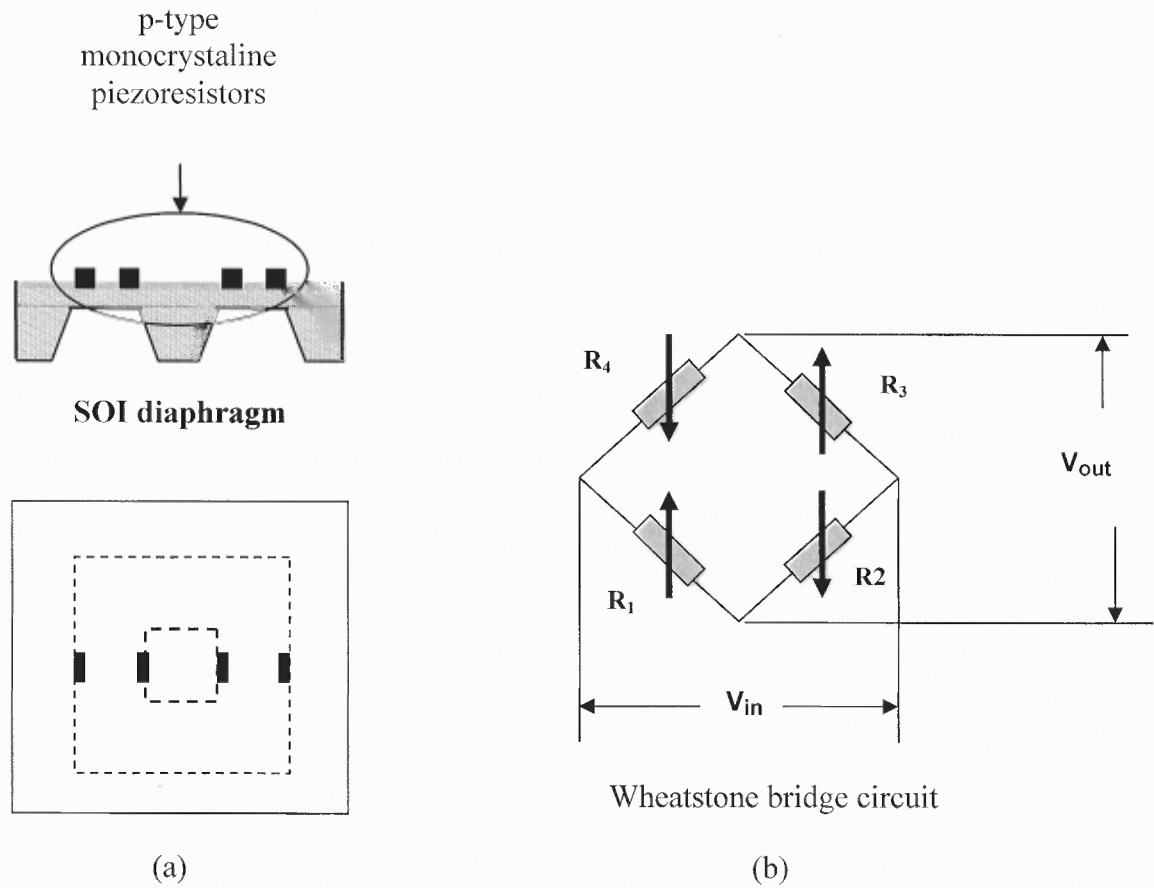
Figure 6.2 a- Piezoresistive sensor, b- Piezoresistors in a Wheatstone bridge.

The output is proportional to the input voltage and the resistance change due to the applied pressure is directly proportional to the stress of the diaphragm as a result of the external applied pressure.

Figure 6.2 (a) shows the cross section and the top view of a silicon diaphragm with four piezoresistors in a Wheatstone bridge configuration; part (b) shows details of the Wheatstone bridge configuration.

6.2 Fabry-Perot Sensor Design

The Fabry-Perot part of the sensor is designed with an optical cavity (Fabry-Perot cavity) formed between the center rigid body surface and a single mode fiber tip (Figure 6.3).
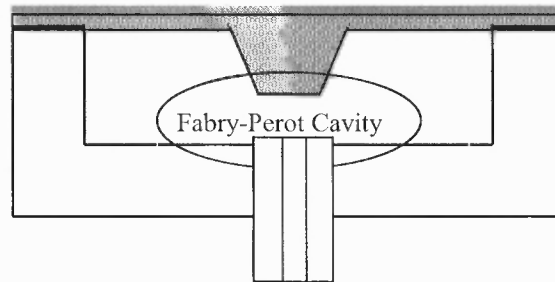
Figure 6.3 Fabry-Perot cavity.

The movement of the boss surface due to applied pressure produces a change in the dimension of the Fabry-Perot gap and produces multiple reflection of the light inside the cavity resulting in interference between reflected beams on the first surface interface (glass-air) and the second surface interface (air-boss surface), respectively.

As discussed in Chapter Five, the reflected intensity from the Fabry-Perot is given by:

$$I_r = I_i \left(\frac{R_1 + R_2 + 2\sqrt{R_1 R_2} \cos(\delta)}{1 + R_1 R_2 + 2\sqrt{R_1 R_2} \cos(\delta)} \right) \tag{6.1}$$

6.3 Advantages of Application of Embossed Diaphragm in the Design and Fabrication of Fabry-Perot sensor

This section is dedicated to a discussion of the advantages of the application of embossed diaphragms in the fabrication of Fabry-Perot sensors [4, 5, 116, 117].

6.3.1 Parallelism Between the Fabry-Perot Cavities

By definition, the Fabry-Perot interferometer is established between two parallel surfaces. However, during the fabrication of the Fabry-Perot sensor, it is difficult to maintain this parallelism due to the non-planar deflection of the diaphragm under applied pressure.

Figure 6.4 illustrates how the introduction of a rigid center eliminates the fundamental deficiency related to the non-parallelism between the two surfaces (diaphragm and fiber) because the embossment (boss) remains flat after the diaphragm is deflected by the applied pressure.
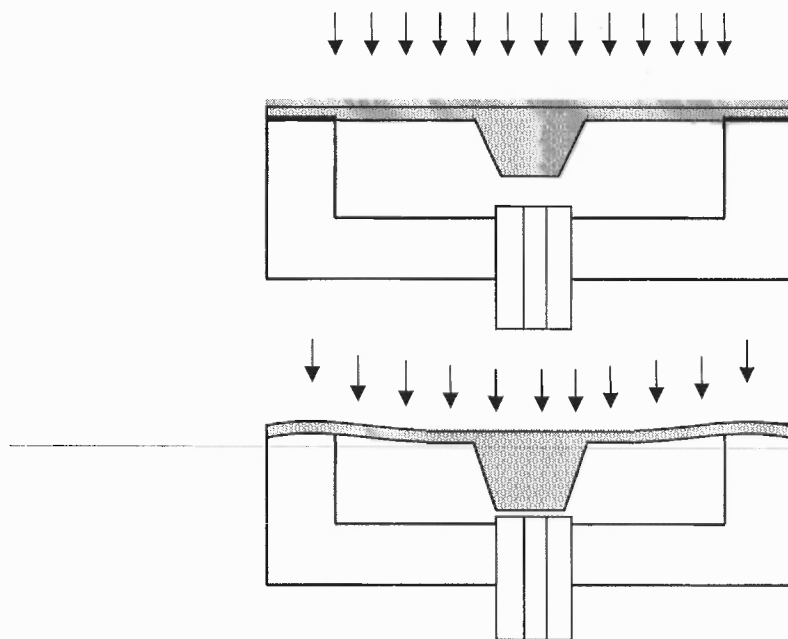
Figure 6.4 The flatness of the rigid body surface under applied pressure maintains the parallelism between the two surfaces.

6.3.2 Alignment Tolerance

The introduction of the flat diaphragm with a rigid center permits the sensor to be less sensitive to the lateral misalignment during the fabrication process, because the core diameter of the fiber is much smaller than the width of the embossement (Figure 6.5).
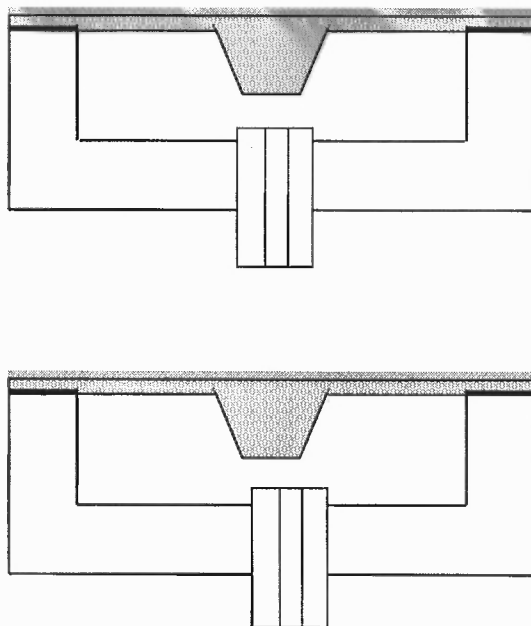
Figure 6.5 The flatness of the rigid body surface reduces the lateral misalignment during the fabrication process.

6.3.3 Well Defined Cavity

The introduction of the rigid body combined with the use of MEMS technology permits fabricating a well defined and very small cavity gap, which contributes to maximizing the amount of light returning to the fiber, thereby, increasing the efficiency of the sensor (cavity gap exaggerated for clarity)(Figure 6.6).
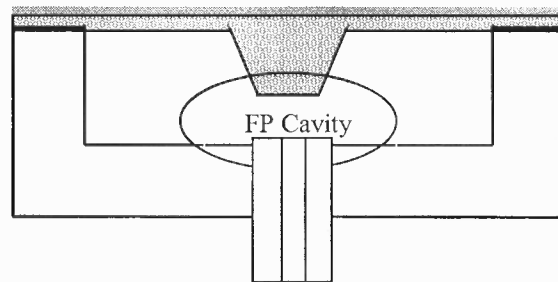
Figure 6.6 Well defined and small Fabry-Perot cavity.

6.3.4 Reduction of the Back Pressure

The introduction of the new design also reduces considerably the back pressure from the glass or silicon surface, which is related to the sensitivity of the sensor.

Back pressure relief
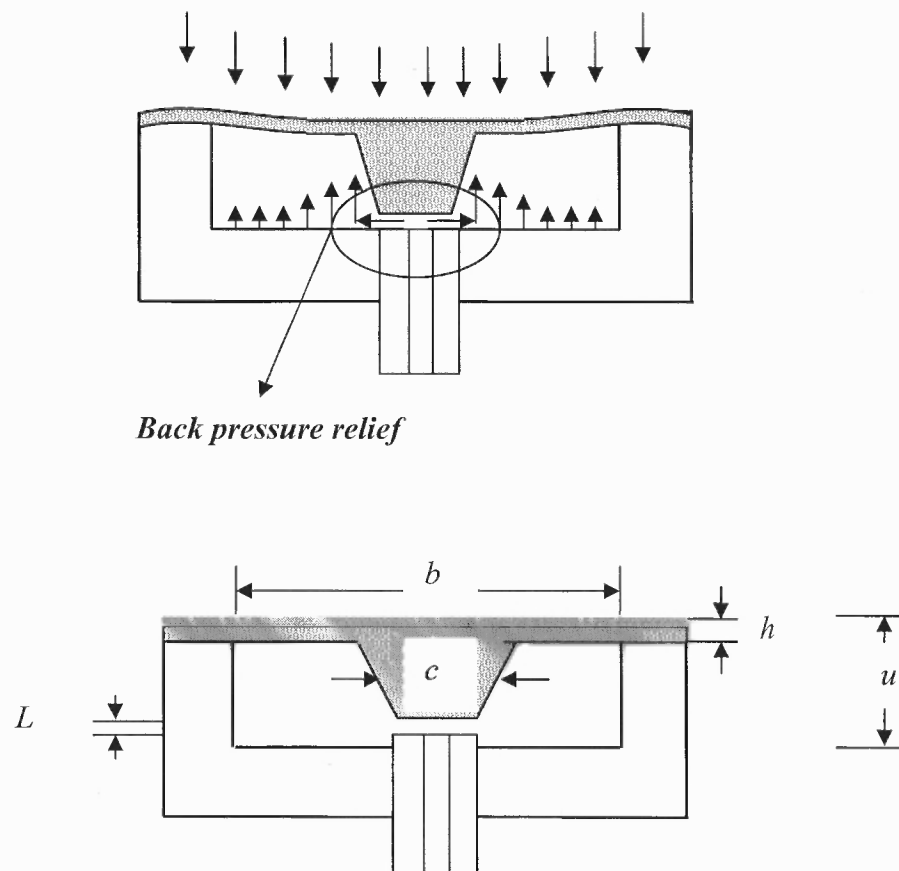
Figure 6.7 Back pressure relief with the introduction of the embossed diaphragm.

Backpressure is defined as the pressure change in the sensor cavity, which is bound by the back surface of the diaphragm, the glass surface, and the surface of the fiber including the interference gap, due to the pressure variation at the front of the diaphragm (Figure 6.7).

From ideal gas laws, we have

$$\Delta P_b = -\frac{\Delta V_b}{V_b} P_b \tag{6.2}$$

where P_b is the equilibrium back pressure, V_b is the equilibrium back volume, and ΔP_b, the back pressure increase due to diaphragm bending and change in cavity length ΔL, which decreases the back volume ΔV_b. Under the condition for small bending, where the displacement of the diaphragm, $\Delta L = L_o\text{-}L$ is much smaller than the thickness h of the diaphragm, the displacement is proportional to the pressure acting on the diaphragm:

$$L_o - L = \frac{b^4(1-\mu^2)}{16\eta E h^3} P \tag{6.3}$$

where b denotes the size of the clamped or rigidly supported diaphragm, h is the thickness of the diaphragm, η is a constant that depends on the shape of the diaphragm, μ and E are the Poisson ratio and Young's modulus of the diaphragm material, respectively.

By using Equation 6.2, one has

$$\Delta V_b = \alpha b^2 \Delta L = -\alpha \frac{b^6(1-\mu^2)}{16\eta E h^3} \Delta P_f \tag{6.4}$$

where ΔP_f is the pressure increase at the front of the diaphragm, and $\alpha \approx 0.5$ if the diaphragm surface remains flat during bending, and $\alpha > 0.5$ for curved diaphragm bending.

As shown in Figure 6.7, we have:

$$V_b = (b^2 - c^2)(u - h - L) + b^2 L \qquad (6.5)$$

Substituting Equation 6.4 and 6.5 in Equation 6.2, we have

$$\frac{\Delta P_b}{\Delta P_f} = \alpha \frac{16\eta E h^3 P_b}{b^6 (1 - \mu^2)} \frac{1}{(b^2 - c^2)(u - h - L) + b^2 L} \qquad (6.6)$$

In the sensor with a rigid embossed center diaphragm, u-h-L is a few orders of magnitude greater than L, while in the sensor without an embossed center, diaphragm u - $h = L$. Therefore,

$$\left(\frac{\Delta P_b}{\Delta P_f} \right)_{u-h \gg L} \ll \left(\frac{\Delta P_b}{\Delta P_f} \right)_{u-h=L} \qquad (6.7)$$

Since the sensitivity of the extrinsic Fabry-Perot interferometer sensor is proportional to the pressure difference of the front side and the back side of the diaphragm,

$$\frac{\Delta P_f - \Delta P_b}{\Delta P_f} = 1 - \frac{\Delta P_b}{\Delta P_f} \qquad (6.8)$$

Thus, the sensitivity of the extrinsic Fabry-Perot interferometer sensor with an embossed center is greater than that without it.

Although, with the introduction of the embossed diaphragm, the back pressure or pressure generated by the surface around the fiber tip can be reduced, a small time delay

will be able to balance the applied pressure inside the cavity that is created between the diaphragm and the surface around fiber tip.

6.4 Integrated Electronic and Optical Pressure Sensor System

This novel design presents a method of combining two principles of measurements into one integrated unit with optical (Fabry-Perot) and electronic (piezoresistive) sensors, to detect movement of the sensing element (embossed diaphragm) under applied external pressure.

Changes in the Fabry-Perot gap are detected with a fiber-optic system interconnecting a laser, optical fibers, a three-dimensional optical coupler, and an optical detector that yields the optical output signal. Changes in the resistances of the piezoresistors are detected by a Wheatstone bridge circuit which yields an electronic output signal. The optical and electronic signals are analyzed in a signal processor to produce a measurement quantity, which is useful for detecting acoustical vibration, mechanical vibration, and pressure. Temperature and magnetic fields can be detected with a modified sensor design.

6.4.1 Fabrication

The embossed diaphragm and the electronic part (piezoresistors) are fabricated using standard MEMS processing techniques for piezoresitive pressure sensors, delivering an embossed diaphragm with four piezoresistors of p-type silicon interconnected in a Whitestone bridge configuration. The diaphragm also serves as part of the Fabry-Perot cavity .

The piezoresistive sensor including the embossed diaphragm used in this project was adapted from commercially available parts [30].

The optical part of the sensor is formed between the tip of the single mode fiber and the boss surface following the assembly procedure shown in Figure 6.8. The tip of the fiber was prepared by cutting the optical fiber with a diamond cutting tool.
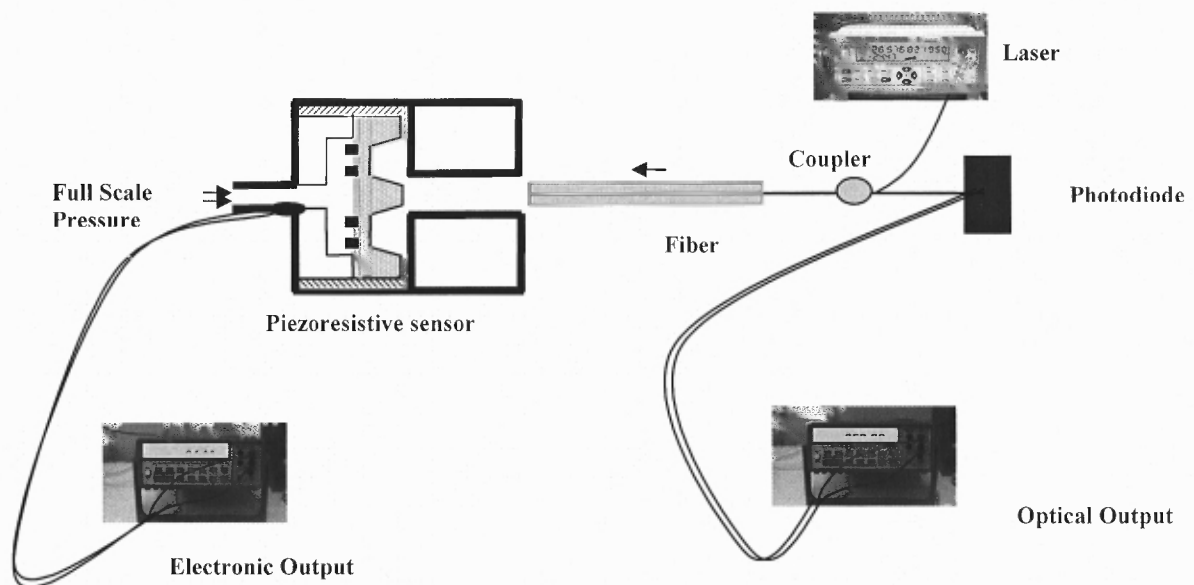
Figure 6.8 Fabry-Perot sensor assembly.

For a desired dimension for the gap in the Fabry-Perot cavity, a corresponding pressure is applied to deflect the diaphragm by that dimension. The value of that pressure is determined by monitoring the output of the electronic part of the sensor. The fiber is then introduced through the port facing the boss surface. When the tip of the fiber reaches the boss surface and is in contact with it, the electronic output begins to decrease in magnitude as a result of the back pressure from the fiber tip on the diaphragm. At this

point, the position of the fiber can be fixed. When setup pressure is released, the Fabry-Perot part of the sensor has the well defined cavity. Figure 6.9 shows a photograph of the fabricated pressure sensor. The pressure sensor system is shown in Figure 6.10.
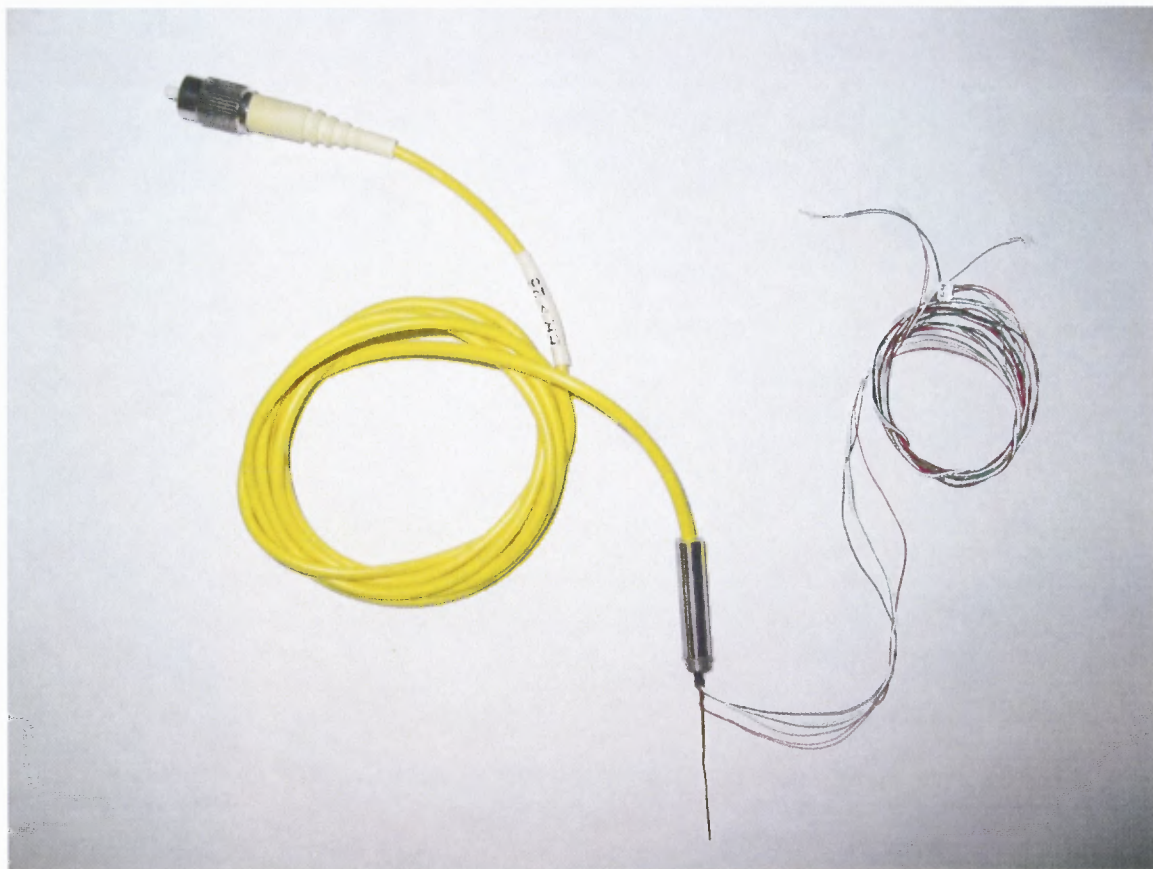
Figure 6.9 Integrated Piezoresistive/ Fabry-Perot pressure sensor.
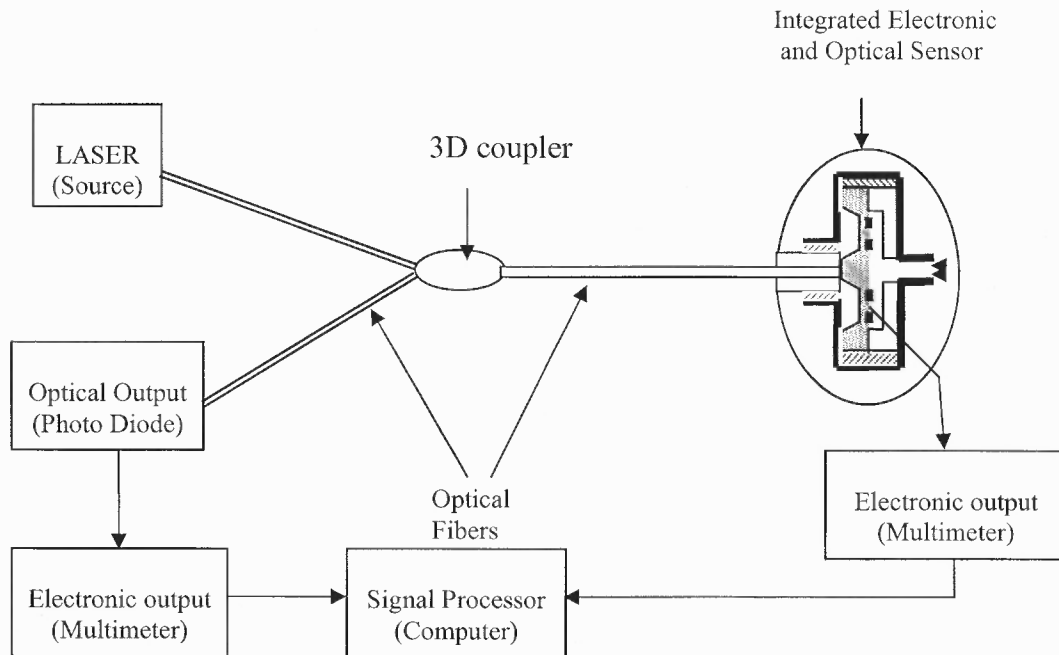
Figure 6.10 Integrated Piezoresistive/ Fabry-Perot sensor system.

6.4.2 Theoretical Analysis

Electronic Output

The basic structure of a piezoresistive pressure sensor consists of four resistor sensing elements in a Wheatstone bridge configuration that measure stress within a thin crystalline silicon membrane. The stress is a direct consequence of the membrane deflecting in response to an applied pressure differential across the front and back sides of the sensor.

The stress is, to a first order approximation, linearly proportional to the applied pressure differential. The output at full-scale applied pressure is a few millivolts per volt of bridge excitation (the supply voltage to the bridge). The output normalized to input applied pressure is known as sensitivity.

The output from the Wheatstone bridge is given by:

$$V_{out} = (\frac{\Delta R}{R} + const.)V_{in}$$

(6.9)

where $(\frac{\Delta R}{R} + const.)$ is proportional to the stress:

$$(\frac{\Delta R}{R} + const.) \approx c\sigma$$

(6.10)

where c represents a constant of proportionality. The stress σ for the embossed diaphragm

is given by (see Chapter Three):

$$\sigma = \frac{3P}{4h^2}\left(a^2 - b^2\right)$$

(6.11)

Combining Equations 6.9, 6.10 and 6.11, one obtains:

$$V_{out} = \frac{3cV_{in}(a^2 - b^2)}{4h^2}P$$

(6.12)

where the factor $m = \frac{3cV_{in}(a^2 - b^2)}{4h^2}$ represents the slope of $V_{out} = mP$ and corresponds to

the sensitivity of the device .

Optical Output

Combining Equations 3.20 and 3.21 from Chapter Three with Equations 5.2 and 5.3 from

Chapter Five, and redefining the Fabry-Perot cavity separation $d = d_0 - W_0$ for static

pressure or $d = d_0 \pm W_0$ for dynamic measurements, the expression that describes the

behavior of the Fabry-Perot sensor investigated in the present study is obtained:

$$I_r = I_i \frac{R_1 + R_2 + 2\sqrt{R_1 R_2}\cos\left(\dfrac{4\pi n\left(d_0 + \left(\dfrac{3(1-\mu^2)}{16}*\left(1-\dfrac{b^4}{a^4}-4*\dfrac{b^2}{a^2}\ln\dfrac{a}{b}\right)\right)\dfrac{P}{E}\dfrac{a^4}{h^3}\right)}{\lambda}\right)}{1 + R_1 R_2 + 2\sqrt{R_1 R_2}\cos\left(\dfrac{4\pi n\left(d_0 + \left(\dfrac{3(1-\mu^2)}{16}*\left(1-\dfrac{b^4}{a^4}-4*\dfrac{b^2}{a^2}\ln\dfrac{a}{b}\right)\right)\dfrac{P}{E}\dfrac{a^4}{h^3}\right)}{\lambda}\right)} \quad (6.13)$$

where, I_r is the optical intensity reflected from the Fabry-Perot cavity and I_i is the laser source intensity incident on the Fabry-Perot cavity through the optical fiber. The other parameters are defined in Chapter Five.

Equation 6.13 is used to fit the experimental data. During the curve fitting, the reflectance of the air-silicon surface will be kept constant (the silicon wafer surface remains unaltered) and the variables will be the reflectance of the fiber-air surface (the fiber tip surface depends on the cutting quality) and the dimensions of the diaphragm (Table 6.1), which are determined during the fabrication process.

6.4.3 Experimental Analysis

Two of the sensors fabricated in this study were tested using a weight-tester that permits application of precise increments of pressure up to 50 psi. A laser source operating at 1.55 μm was used in connection with a 3D coupler and a photodiode. Two digital multimeters were used to collect the output from the optical and electronic parts of the sensor (Figure 6.11).
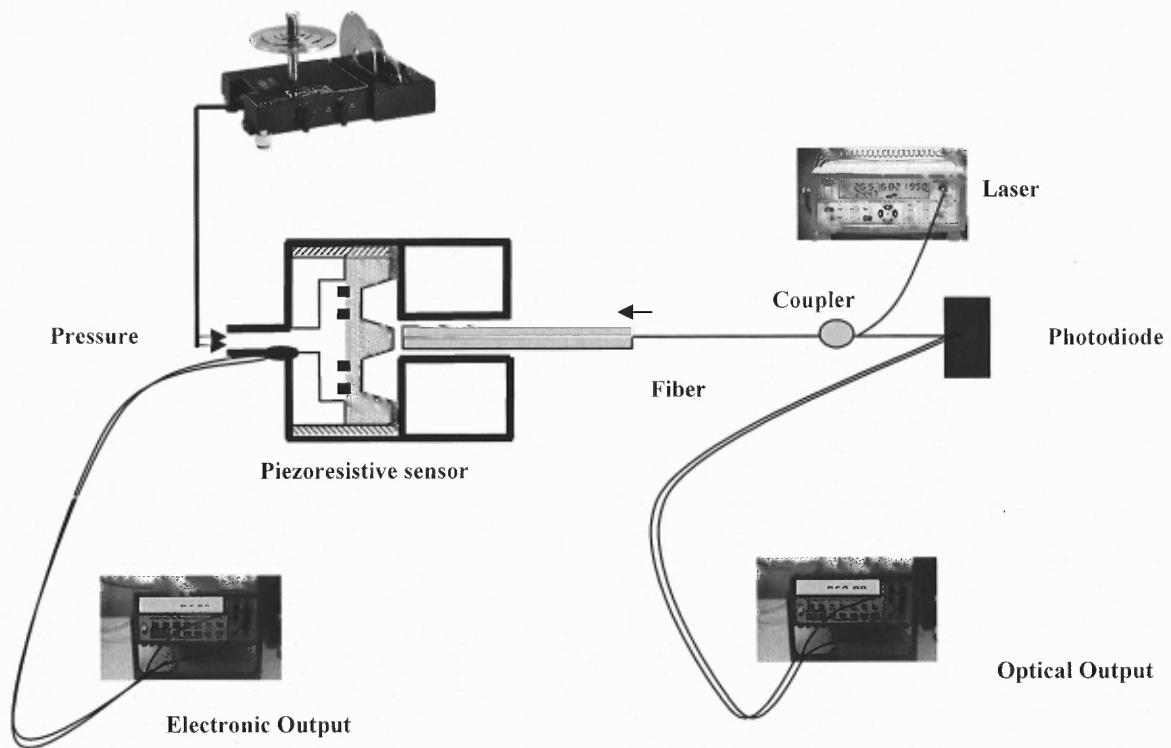
Figure 6.11 Optical and electronic measurement setup.

The diaphragm dimensions for each sensor are given in Table 6.1. They were designed to operate at 5 psi pressure with an overpressure tolerance of 10 psi.

Table 6.1 Sensor Dimensions

Diaphragm radius (μm)	533.4 +/- 5
Diaphragm thickness (μm)	11.4 +/- 5
Boss radius (μm)	368.3 +/-5
Boss height (μm)	100-105

Electronic Output

The electronic reading was collected with 5-volt input on the Wheatstone bridge. The atmospheric pressure varied within 0.2 psi from the first day to the last day of an experimental test period of twelve days. Table 6.2 shows the electronic output reading for two sensors, for the day one and day two of testing. On the first day, sensor one was tested with a pressure increment of 1 psi, and sensor two was tested with an increment of 0.5 psi. On the last day, both sensors were tested with an increment of 0.25 psi, which is the minimum increment capability of the weight-tester, to increase the number of data points.

Table 6.2 Electronic Output Readings

Pressure (psi)	Electronic Output					
	Day one (06/04/09)				Day two (06/15/09)	
	Sensor one		Sensor two		Sensor one	Sensor two
	Setup 1	Setup 2	Setup 1	Setup 2	Setup 1	Setup 1
	(V)	(V)	(V)	(V)	(V)	(V)
0	-18.80	-18.80	-38.80	-38.70	-18.60	-38.80
0.25					-14.53	-33.45
0.75					-6.60	-24.40
1	-2.80	-2.80	-20.80	-20.75	-2.48	-20.90
1.25					1.52	-15.45
1.5			-11.85	-11.70		
1.75					9.62	-6.45
2	13.15	14.05	-2.75	-2.85	13.68	-3.05
2.25					17.70	2.80
2.5			6.30	6.50		
2.75					25.84	11.80
3	29.40	29.75	15.15	15.25	30.00	15.30
3.25					34.03	20.65
3.5			24.55	24.45		
3.75					42.23	29.50
4	46.65	46.35	33.00	33.30	46.19	33.05
4.25					50.60	38.70
4.5			42.40	42.30		
4.75					58.85	47.45
5	62.35	61.45	51.00	51.45	63.20	51.15
5.25					67.30	56.55
5.5			60.05	60.02		
5.75					73.49	65.30
6	78.65	77.85	68.70	69.30	77.55	69.00

Figure 6.12 shows the electronic output vs. pressure for the data given in Table 6.2 for sensor 1.
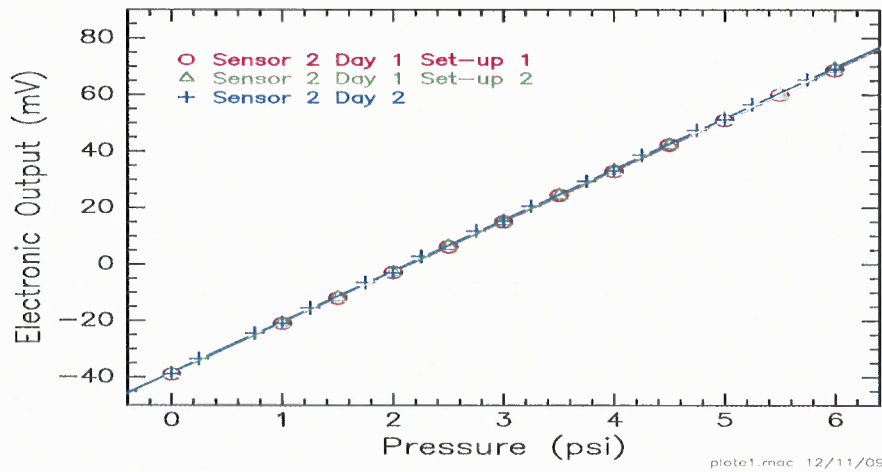
Figure 6.12 Electronic output vs. pressure for sensor 1 on days one and two.

Figure 6.13 shows the electronic output vs. pressure for the data given in table 6.2 for sensor 2. Figures 6.12 and 6.13 show the repeatability of the data for each sensor. The slope of the line in each case represents the sensor sensitivity of the sensor which corresponds to the following: for sensor 1, 16.11 mV/psi and for sensor 2, 17.96 mV/psi.
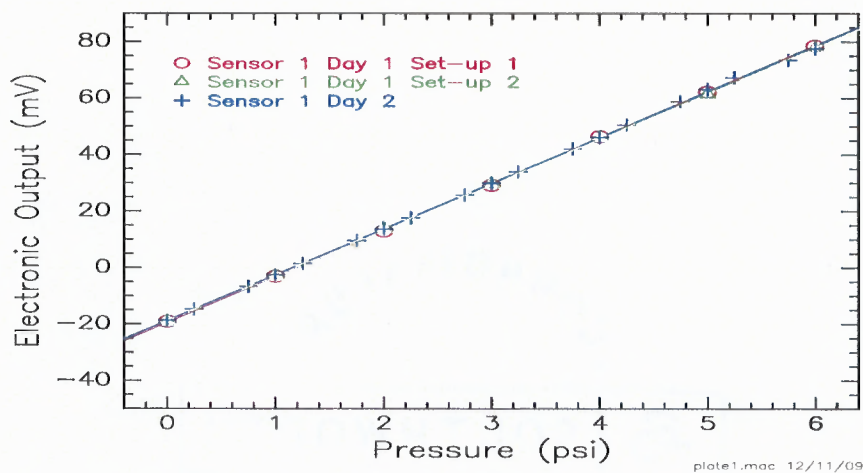
Figure 6.13 Electronic output vs. pressure for sensor 2 on days one and two.

Optical Output

The optical reading was collected with the fiber position not permanently fixed so that the sensor could be tested with various Fabry-Perot cavity lengths.

Table 6.3 Optical Output Readings

Pressure (psi)	Optical Output					
	Day one (06/04/09)				Day two (06/15/09)	
	Sensor one		Sensor two		Sensor one	Sensor two
	Setup 1	Setup 2	Setup 1	Setup 2	Setup 1	Setup 1
	(V)	(V)	(V)	(V)	(V)	(V)
0	1.42	0.51	2.04	2.03	0.61	0.21
0.25					0.60	0.17
0.75					0.55	0.25
1	1.63	0.44	2.05	1.95	0.45	0.30
1.25					0.28	0.42
1.5			1.93	1.73		
1.75					0.19	0.57
2	1.46	0.70	1.72	1.59	0.18	0.59
2.25					0.29	0.62
2.5			1.63	1.71		
2.75					0.48	0.56
3	1.00	0.88	1.76	1.91	0.55	0.51
3.25					0.60	0.38
3.5			1.96	2.02		
3.75					0.58	0.23
4	1.14	0.72	2.05	2.05	0.53	0.19
4.25					0.48	0.19
4.5			2.07	2.04		
4.75					0.29	0.28
5	1.46	0.57	2.08	1.94	0.23	0.35
5.25					0.18	0.46
5.5			1.98	1.74		
5.75					0.22	0.59
6	1.61	0.45	1.84	1.65	0.24	0.63

Also, during the test, the laser power was changed producing variation in the intensity for different testing. Table 6.3 shows the data for the optical output for the first day and the last day of testing (taken simultaneously and with the same pressure values as the electronic output data of Table 6.2).

Figure 6.14 shows the experimental optical output as a function of applied pressure for sensor two during the second day of the test. Figure 6.15 shows the sensitivity for this sensor, which is obtained by taking the numerical derivative of the data in Figure 6.14. Dashed curves in both figures are spline fits to guide the eye.
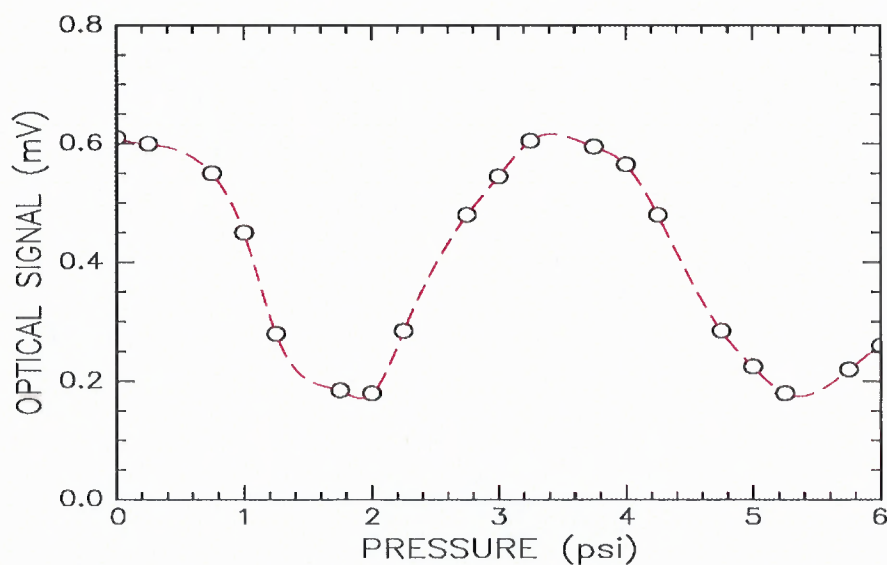
Figure 6.14 Optical signal for sensor 2 on the second day.
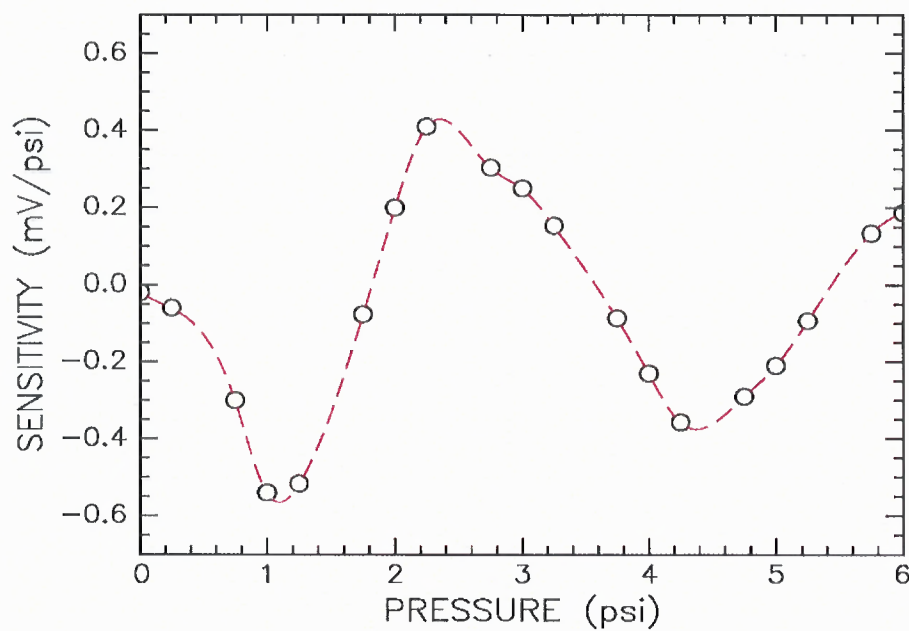
Figure 6.15 Optical sensitivity of sensor 2.

Figure 6.16 shows the output for sensor two from two different test setups (cavity lengths) taken on the same day. The solid curves show the results of fitting Equation 6.13 to the data using a non-linear least squares method (obtained from Genplot software). Table 6.4 shows the fitting parameters. This illustrates the observed effect of changing the dimension of the Fabry-Perot gap by 0.106 μm, as determined from the difference in fitting parameters d_0.
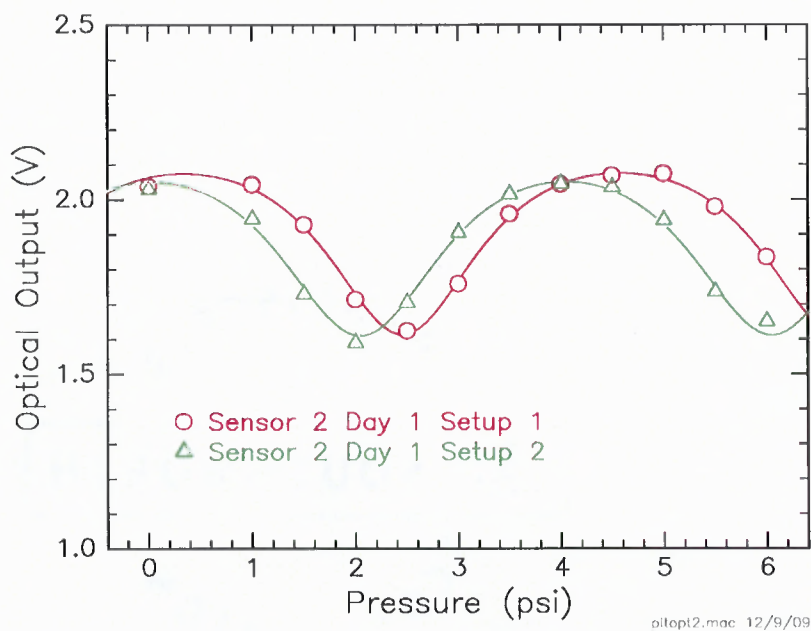
Figure 6.16 Optical output for sensor two from two different test setups.

Table 6.4 Fitting Parameters for Sensor 2 Day 1 Data

	Fitting Parameters	Values	Sigma (error)
Sensor 2 Day 1 Setup 1	Cavity gap (d_o)	0.759 µm	0.021
	Diaphragm Radius (a)	518 µm	0.7
	Fiber-Air Reflectance (R_1)	0.216	0.038
	Air- Silicon Reflectance (R_2)	0.875	0.022
	Incident Beam Intensity (I_i)	2.43 (V)	0.12
	CHISQR	0.936×10^{-3}	
Sensor 2 Day 1 Setup 2	Cavity Gap (d_o)	0.653 µm	0.018
	Diaphragm Radius (a)	515 µm	0.6
	Fiber-Air Reflectance (R_1)	0.271	0.035
	Air- Silicon Reflectance (R_2)	0.898	0.013
	Incident Beam Intensity (I_i)	2.352 (V)	0.07
	CHISQR	0.7703×10^{-3}	

As can be seen in Figure 6.16, the experimental results corroborate the analytical solution for both parts of the sensor and validate the plane wave principles of operation of a Fabry-Perot interferometer as a mechanism for pressure sensing.

The diaphragm radius (a) and the incident beam intensity (I_i) values obtained from the curve fitting are in the range of the actual values used in the test. The Fabry-Perot cavity gap (d_0) corresponds to the expected value (less than 1 μm from the deflection of the diaphragm for the corresponding dimension at 6 psi). The values of the reflectances for both interfaces do not correspond to the referenced values of 0.4 for fiber-air interface, and 0.55 for air-silicon interface. Although additional research is recommended, the fiber-air reflectance depends on fiber cutting since the final fiber tip may not be perfectly smooth and flat. In the case of the air-silicon interface, the silicon surface could be affected from the fiber tip contact during the Fabry-Perot sensor setup; as has been mentioned earlier, the fiber is not fixed and is used for more than one test.

As a further test, possible deviation from the plane wave approximation was examined by fitting a Gaussian beam spreading model [118, 119] to the data. In this model, Equation 6.13 is multiplied by the factor exp $[-\alpha d^2/\lambda^2]$, where α is a fitting constant. The result, $\alpha = 0 \pm 0.2$, shows that Gaussian beam spreading is insignificant, verifying that boss surface and fiber tip surface are parallel and closely spaced, and the embossement of the diaphragm remains flat under applied pressure.

6.4.2 Noise test

The experimental set-up for noise measurement is shown in Figure 6.17, in which the output of the photo diode is connected to a lock-in amplifier (EG&G model 124A, with a model 118 preamplifier). The coupling capacitor is of a silver-mica low noise type

(with a value of capacitance C = 4896 pF). A range of frequency between 3.2 Hz and 32

KHz was used, including 3.2, 10, 32, 100, 320, 1000, 3200, 10000, and 32000 Hz. The

lock-in detector was set-up as an AC RMS volt meter with a 10% equivalent noise band

width.
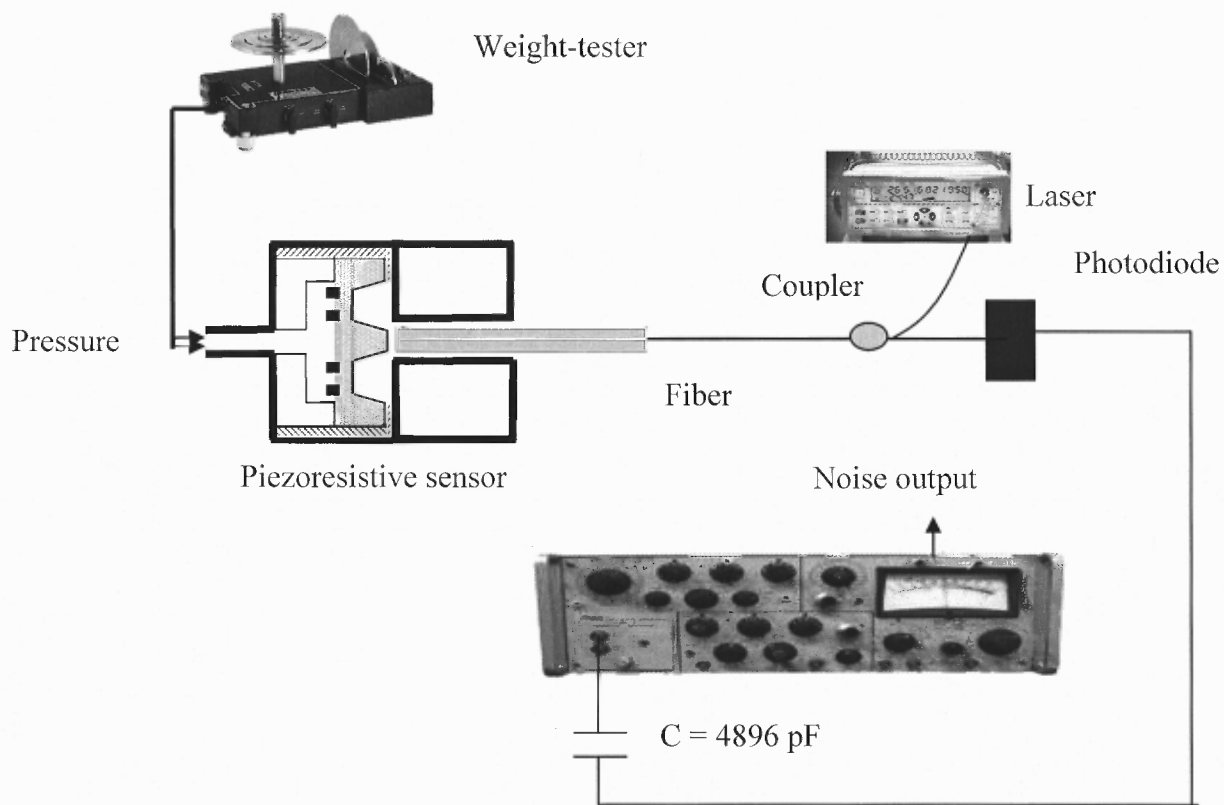
Figure 6.17 Experimental set-up for noise measurement.

The values of the pressure selected for use in the noise test were determined from

the optical output of sensor two on the second day of testing, as described in the previous

section and shown in Figure 6.14. Figure 6.14 shows the pressure vs. optical output of

this sensor, where it can be noted that the pressure values of 0, 1, 2, 2.75, 3.25, 4.25, and

5.25 psi correspond to the inflection points to the corresponding curve, which in principle

should be more sensitive to noise.

Table 6.5 shows the raw RMS noise data, and Figure 6.18 illustrates the frequency dependency at the various test pressures. The peak obtained around 32 Hz is related to the frequency dependence of the noise and the 10% band width. Data denoted "Diode" were taken with the laser turned off.

Table 6.5 Noise Test Data

Frequency	0 psi	1 psi	2 psi	2.75 psi	3.25 psi	4.25 psi	5.25 psi	Diode
(Hz)	(μV)	(μV)	(μV)	(μV)	(μV)	(μV)	(μV)	(μV)
3.2	20.0	50.00	40.00	30.00	25.00	40.00	25.00	15.00
10	80.0	100.00	50.00	40.00	110.00	100.00	50.00	10.00
32	90.0	150.00	80.00	200.00	200.00	150.00	220.00	8.00
100	30.0	60.00	30.00	40.00	60.00	70.00	40.00	5.00
320	25.0	40.00	12.00	20.00	25.00	20.00	18.00	2.80
1000	15.0	10.00	10.00	10.00	10.00	15.00	10.00	1.60
3200	20.0	40.00	15.00	25.00	18.00	20.00	20.00	1.60
10000	40.0	30.00	20.00	30.00	40.00	70.00	25.00	1.60
32000	80.0	90.00	30.00	60.00	80.00	80.00	30.00	1.60
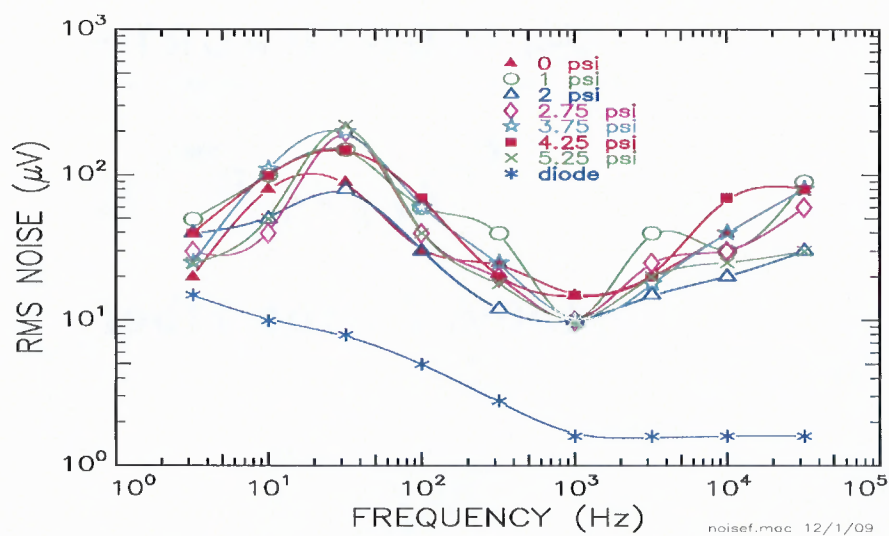
Figure 6.18 Noise test data.

Figure 6.19 shows the RMS noise vs. sensitivity for the low frequencies. All of the data show that the noise is independent of the sensitivity of the Fabry-Perot interferometer, except for the lowest frequency (3.2 Hz), as shown in Figure 6.20 on an expanded scale. Additionally, the noise is fund to be uncorrelated with the magnitude of the optical signal.
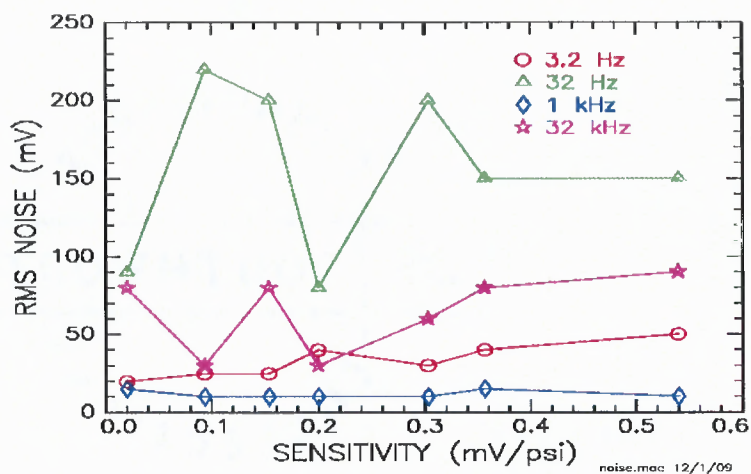
Figure 6.19 RMS noise vs. sensitivity for the low frequencies.
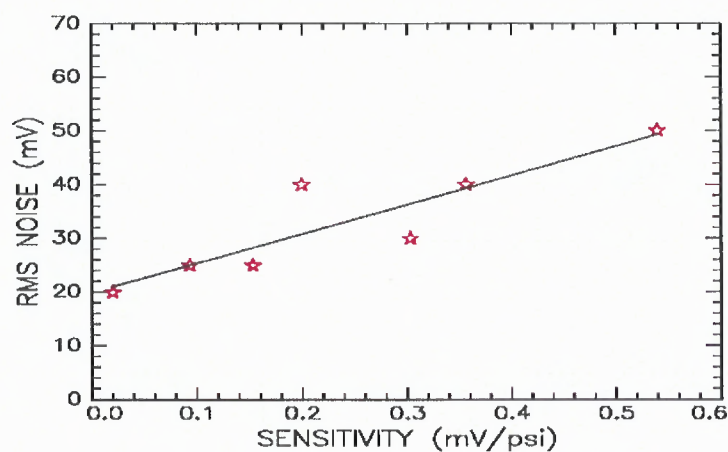
Figure 6.20 RMS noise vs. sensitivity for 3.2 Hz.

Figure 6.21 shows the noise divided by the square root of the bandwidth as a function of frequency. The data shows 1/f behavior of the noise between 32 Hz to 1 kHz (dashed line in Figure 6.21), and tendency for saturation outside that region.
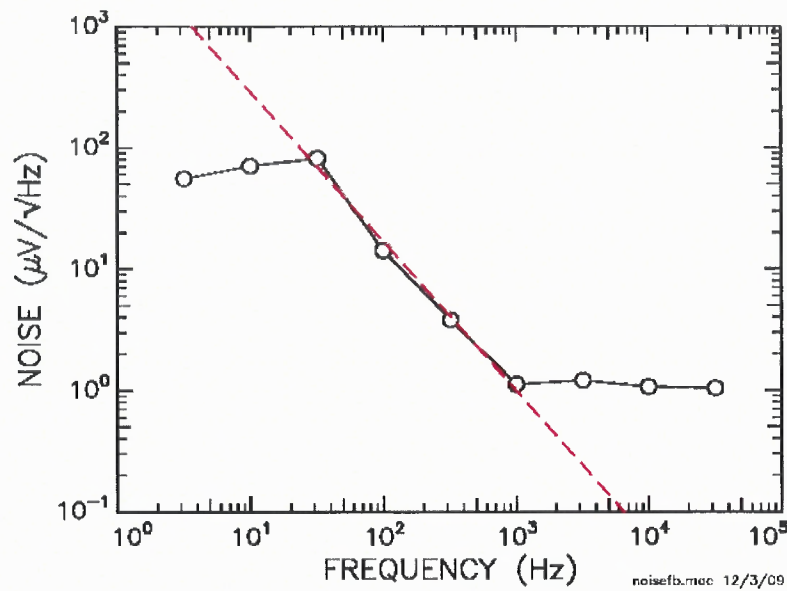
Figure 6.21 Noise vs. frequency.

From the result of this noise analysis, it appears that the system noise is caused by the external instruments (laser, photodiode) and it is not from the Fabry-Perot interferometer itself.

CHAPTER 7

CONCLUSIONS AND RECOMMENDATIONS

The purpose of this dissertation is to introduce a novel approach in the design and fabrication of Fabry-Perot diaphragm based pressure sensors and the integration of the optical and electronic techniques for the development of pressure sensors.

7.1 Conclusions

The introduction of the embossed diaphragm in the design and fabrication of piezoresistive and Fabry-Perot diaphragm based sensors offer diverse advantages over relate to the standard diaphragms without an embossment. It makes the electronic sensor more linear, and eliminates the fundamental deficiency related to non-parallelism between the two surfaces (diaphragm and fiber), after applied pressure, in the optical part of the sensor. It also permits the sensor to be less sensitive to lateral misalignment during the fabrication process and reduces considerably the back pressure, which otherwise will reduce the sensitivity of the sensor.

The physical characteristics and behavior of the embossed diaphragm facilitates the fabrication of electronic and optical integrated sensor, which introduces additional advantages such as: two independent outputs in one sensor, the possibility to measure static and dynamic pressure simultaneously, and the measurement of two different physical quantities such as temperature and pressure. The output signals from both parts of the sensor can be used independently of each other, as verification of the measured magnitude, and as a mechanism for back-up in continuous monitoring systems.

The novel design and the experimental output related to the Fabry-Perot part of the sensor demonstrate the use of Fabry-Perot interferometry technique in the fabrication of diaphragm based pressure sensors.

The measured experimental data verifies the analytical solution for the sensor, validating the presence of a true Fabry-Perot interferometer sensor.

7.2   Recommendations

Integrated techniques for the fabrication of pressure sensors have the potential to contribute to future applications as well as to improve the current pressure sensor applications.

Based on the above investigations, it is recommended that the study of the effects of the use of various optical sources to determine the appropriate source for a specific application be continued. Also, an analysis of the effect of the embossed surface coatings is suggested, as well as a study of the simulation of the performance of the sensor of various dimensions; the choice of materials and laser input parameters will be necessary to determine an optimal design to permit the sensor to have a close to linear output.

It is critical to explore the potential of this novel sensor for specific applications and to analyze the performance of the sensor with temperature.

APPENDIX

GENPLOT SOURCE CODES FOR DATA ANALYSIS

All data in this dissertation have been analyzed and plotted using the Genplot software [120]. The codes are shown in the same order as the corresponding the figure.

Figure 6.12 Electronic output vs. pressure for sensors 1 on days one and two.

```
/* plote1.mac
/* plot data and linear fit
/* Dec 11, 2009
/* USAGE:
/*   dev postscript (enter file name)
/*   x plote1
/*   dev vga
/*   quit
label left
Electronic Output (mV)
label bot
Pressure (psi)
linewidth 3
force yes
region left -50 90
region bot -.4 6.4
/* sgraph idsize .22
offset .45 .3
symsize .25
let $idsize=.15
let $idspac=1.8
read sensor11 -col 1 2
let ids='Sensor 1 Day 1 Set-up 1' arch d1
read sensor11 -col 1 3
let ids='Sensor 1 Day 1 Set-up 2' arch d2
read sensor12 -col 1 2
let ids='Sensor 1 Day 2' arch d3
autoids on let $idtskp=.5 let $idlskp=.3
ltype 0 symbol 1 pl d1 -pen 2
ltype 0 symbol 2 ov d2 -pen 3
ltype 0 symbol 3 ov d3 -pen 4
autoids off
retr d1 fit linear
fix_grid -from -.4 -to 6.4 -points 100 let y=fit(x)
let ids='fit 1'arch f1
```

```
ltype 1 ov -exclude d1 -pen 2
retr d2 fit linear
fix_grid -from -.4 -to 6.4 -points 100 let y=fit(x)
let ids='fit 2'arch f2
ltype 1 ov -exclude d2 -pen 3
retr d3 fit linear
fix_grid -from -.4 -to 6.4 -points 100 let y=fit(x)
let ids='fit 2'arch f3
ltype 1 ov -exclude d3 -pen 4
annote
size .1
linewidth 1
label 6.5 0
plote1.mac 12/11/09
quit
```

Figure 6.13 Electronic output vs. pressure for sensors 2 on days one and two.

```
/* plote2.mac
/* plot data and linear fit
/* Dec 11, 2009
/* USAGE:
/*   dev tiff (enter file name)
/*   x plote2
/*   dev vga
/*   quit
label left
Electronic Output (mV)
label bot
Pressure (psi)
linewidth 3
force yes
region left -50 90
region bot -.4 6.4
/* sgraph idsize .22
offset .45 .3
symsize .25
let $idsize=.15
let $idspac=1.8
read sensor21 -col 1 2
let ids='Sensor 2 Day 1 Set-up 1' arch d1
read sensor21 -col 1 3
let ids='Sensor 2 Day 1 Set-up 2' arch d2
read sensor22 -col 1 2
let ids='Sensor 2 Day 2' arch d3
autoids on let $idtskp=.5 let $idlskp=.3
```

```
ltype 0 symbol 1 pl d1 -pen 2
ltype 0 symbol 2 ov d2 -pen 3
ltype 0 symbol 3 ov d3 -pen 4
autoids off
retr d1 fit linear
fix_grid -from -.4 -to 6.4 -points 100 let y=fit(x)
let ids='fit 1'arch f1
ltype 1 ov -exclude d1 -pen 2
retr d2 fit linear
fix_grid -from -.4 -to 6.4 -points 100 let y=fit(x)
let ids='fit 2'arch f2
ltype 1 ov -exclude d2 -pen 3
retr d3 fit linear
fix_grid -from -.4 -to 6.4 -points 100 let y=fit(x)
let ids='fit 2'arch f3
ltype 1 ov -exclude d3 -pen 4
annote
size .1
linewidth 1
label 6.5 0
plote1.mac 12/11/09
quit
```

Figure 6.16 Optical output for sensor 2 from two different test setups.

```
/* pltopt2.mac
/* plot sensor 69A day 1 setup 1 and setup 2
/* Dec 9, 2009
/* USAGE:
/*   dev postscript (enter file name)
/*   x pltopt2
/*   dev vga
/*   quit
label left
Electronic Output (mV)
label bot
Pressure (psi)
linewidth 3
force yes
region left 1 2.5
region bot -.4 6.4
/* sgraph idsize .22
offset .45 .3
symsize .25
let $idsize=.18
let $idspac=1.8
```

```
read tab63 -col 1 2
sort transform compress 2 let y=y/2
let ids='Sensor 1 Day 1 Setup 2' arch d2
read 69aup0 read 69adn -appen
sort transform compress 2 let y=y/2
let ids='Sensor 1 Day 1 Setup 1' arch d1
autoids on let $idtskp=4 let $idlskp=.5
ltype 0 symbol 1 pl d1 -pen 2
symbol 2 ov d2 -pen 3
autoids off
read 69fit
ltype 1 ov -exclude d1 -pen 2
read 69fit2
ov -exclude d2 -pen 3
annote
/* label 6 2
/* Day One
/* Day Two
size .1
linewidth 1
label 6.5 0
pltopt2.mac 12/9/09
quit
```

Figure 6.18 Noise test data.

```
/* noisef.mac
/* plot noise vs frequency log-log scale
/* analyze noise vs pressure and frequency data
/* noise-f.dat rows are frequencies, columns are pressures
/* data from 6/15/09
/* Dec 1, 2009
read noise-f -col 1 2 let ids='0 psi' arch n0  /* noise vs frequency at 1 psi
read noise-f -col 1 3 let ids='1 psi' arch n1  /* noise vs frequency at 1 psi
read noise-f -col 1 4 let ids='2 psi' arch n2
read noise-f -col 1 5 let ids='2.75 psi' arch n3
read noise-f -col 1 6 let ids='3.75 psi' arch n4
read noise-f -col 1 7 let ids='4.25 psi' arch n5
read noise-f -col 1 8 let ids='5.25 psi' arch n6
read noise-f -col 1 9 let ids='diode' arch n7
retr n0 let x=log(x) let y=log(y) arch l0
retr n1 let x=log(x) let y=log(y) arch l1
retr n2 let x=log(x) let y=log(y) arch l2
retr n3 let x=log(x) let y=log(y) arch l3
retr n4 let x=log(x) let y=log(y) arch l4
```

```
retr n5 let x=log(x) let y=log(y) arch 15
retr n6 let x=log(x) let y=log(y) arch 16
retr n7 let x=log(x) let y=log(y) arch 17
label left
RMS NOISE (^2I^1V)
label bot
FREQUENCY (Hz)
linewidth 3
force yes
logarith left on logarith bot on
region left 0 3
region bot 0 5
/* sgraph idsize .22
offset .45 .3
symsize .25
let $idsize=.15
let $idspac=1.35
autoids on let $idtskp=.3 let $idlskp=3.5
ltype 0 symbol 1
symbol 9 pl 10 -pen 2 symbol 1 ov 11 -pen 3 symbol 2 ov 12 -pen 4
symbol 5 ov 13 -pen 5 symbol 6 ov 14 -pen 6
symbol 7 ov 15 -pen 2 symbol 4 ov 16 -pen 3 symbol 11 ov 17 -pen 4
autoids off
ltype 1
retr 10 fit spline -smooth .01 ov -fit -pen 2 -exclude 10
retr 11 fit spline -smooth .01 ov -fit -pen 3 -exclude 11
retr 12 fit spline -smooth .01 ov -fit -pen 4 -exclude 12
retr 13 fit spline -smooth .01 ov -fit -pen 5 -exclude 13
retr 14 fit spline -smooth .01 ov -fit -pen 6 -exclude 14
retr 15 fit spline -smooth .01 ov -fit -pen 2 -exclude 15
retr 16 fit spline -smooth .01 ov -fit -pen 3 -exclude 16
retr 17 fit spline -smooth .01 ov -fit -pen 4 -exclude 17
annote
size .1
linewidth 1
label 6.5 0
noisef.mac 12/1/09
quit
```

Figure 6.19 RMS noise vs. sensitivity for the low frequencies.

```
/* noise.mac
/* analyze noise vs pressure and frequency data
/* noise-p.dat rows are pressures, columns are frequencies
/* data from 6/15/09
/* Dec 2, 2009
```

read noise-p -col 1 2 let ids='3.2 Hz' arch n1   /* noise vs pressure at 3.2 Hz
read noise-p -col 1 4 let ids='32 Hz' arch n2
read noise-p -col 1 7 let ids='1 kHz' arch n3
read noise-p -col 1 10 let ids='32 kHz' arch n4
read sensor69 sort transform compress 2 let y=y/2 let ids='Optical' arch d1
transform dy/dx arch d2 fit spline   /* d2 is sensitivity which is splined, not plotted
retr n1 let y=fit(x) let y=abs(y) let x=n1:y exch sort arch f1   /* noise vs sensitivity 3.2 Hz
retr n2 let y=fit(x) let y=abs(y) let x=n2:y exch sort arch f2
retr n3 let y=fit(x) let y=abs(y) let x=n3:y exch sort arch f3
retr n4 let y=fit(x) let y=abs(y) let x=n4:y exch sort arch f4
label left
RMS NOISE (mV)
label bot
SENSITIVITY (mV/psi)
linewidth 3
force yes
region left 0 250
region bot 0 .6
/* sgraph idsize .22
offset .45 .3
symsize .25
let $idsize=.18
let $idspac=1.8
autoids on let $idtskp=.3 let $idlskp=4.5
ltype 0 symbol 1
pl f1 -pen 2 symbol 2 ov f2 -pen 3 symbol 5 ov f3 -pen 4 symbol 6 ov f4 -pen 5
autoids off
ltype 1 ov f1 -pen 2 ov f2 -pen 3 ov f3 -pen 4 ov f4 -pen 5
annote
size .1
linewidth 1
label 6.5 0
noise.mac 12/1/09
quit

Figure 6.21 Noise vs. frequency.

/* noisefb.mac
/* plot AVERAGE noise vs frequency log-log scale
/* analyze noise vs pressure and frequency data
/* noise-f.dat rows are frequencies, columns are pressures
/* data from 6/15/09
/* Dec 3, 2009
read noise-f -col 1 2 let ids='0 psi' arch n0   /* noise vs frequency at 1 psi
read noise-f -col 1 3 let ids='1 psi' arch n1   /* noise vs frequency at 1 psi
read noise-f -col 1 4 let ids='2 psi' arch n2

```
read noise-f -col 1 5 let ids='2.75 psi' arch n3
read noise-f -col 1 6 let ids='3.75 psi' arch n4
read noise-f -col 1 7 let ids='4.25 psi' arch n5
read noise-f -col 1 8 let ids='5.25 psi' arch n6
read noise-f -col 1 9 let ids='diode' arch n7
retr n0 let x=log(x) let y=log(y) arch l0
retr n1 let x=log(x) let y=log(y) arch l1
retr n2 let x=log(x) let y=log(y) arch l2
retr n3 let x=log(x) let y=log(y) arch l3
retr n4 let x=log(x) let y=log(y) arch l4
retr n5 let x=log(x) let y=log(y) arch l5
retr n6 let x=log(x) let y=log(y) arch l6
retr n7 let x=log(x) let y=log(y) arch l7
retr l0 retr l1 -append retr l2 -append retr l3 -append retr l4 -append retr l5 -append retr l6
-append
sort transform compress 7 let y=y/7 let ids='average'
let y=y-.5*x+.5*log(10.)
arch la
/* see page 3-6
label left
NOISE (^2l^1V/^0?^1Hz)
label bot
FREQUENCY (Hz)
linewidth 3
force yes
logarith left on logarith bot on
region left -1 3
region bot 0 5
/* sgraph idsize .22
offset .45 .3
symsize .25
let $idsize=.18
let $idspac=1.3
/* autoids on let $idtskp=.3 let $idlskp=3.7
ltype 0 symbol 1
pl la
autoids off
ltype 1
ov la -exclude la
cull_data keep xrange 1.2 3.1
fit linear
retr la let y=fit(x)
ltype 2
ov -fit -pen 2
annote
size .1
```

```
linewidth 1
label 6.5 0
noisefb.mac 12/3/09
quit
```

REFERENCES

1. M. Gad-el-Hak, *The MEMS Handbook. MEMS: Applications*, 2nd ed. (CRC Press, 2006).

2. V. Kaajakari. *Practical MEMS* (Small Gear Publishing, 2009).

3. S. Yin, Paul B. Ruffin, and F.T. S. Yu, *Fiber Optic Sensors*. 2nd ed. (CRC Press, 2008).

4. I. Padron, A. T. Fiory and N.M. Ravindra, *Modeling and Design of an Embossed Diaphragm Fabry-Perot Pressure Sensor*, Proceedings of the Materials Science and Technology Conference. Pittsburgh, PA. (2008) pp. 992-997.

5. K. K.Chin, G. Feng, I.Padron, H. Roman, *Aligned Embossed Diaphragm Based Fiber Optic Sensor*. United States Patent Application 20090086214 (April 2, 2009).

6. OMEGA. *Transactions in Measurement and Control. Volume 3: Force-Relate Measurements: Pressure, Strain, Weight, acceleration and Torque.* http://www.omega.com/literature/transactions/volume3/trantocvol3.html. (06/25/2009).

7. Mike Coope, "The History of Pressure Measurement," (Copidate Technical Publicity-Sensorland, Pattingham U.K., http://www.sensorland.com (06/25/2009).

8. R. P. Benedict, Fundamentals of Temperature, Pressure and Flow Measurements, 3rd ed. (Wiley-Interscience, 1984).

9. R. B. Hetnarski and Józef Ignaczak, *The Mathematical Theory of Elasticity*, 2nd ed. (CRC Press, 2004).

10. S. Beeby, Grahan Ensell, Michael Kraft, and Neil White, *MEMS Mechanical Sensors* (Artech House Publishers, 2004).

11. G. T. Kovacs, *Micromachined Transducer Sourcebook* (McGraw-Hill Education, 1998).

12. J. Wilson, *Sensor Technology Handbook* (Newnes, 2004).

13. David Heeley., "Understanding Pressure and Pressure Measurement," Application Note, Freescale Semiconductor Inc. (2005),

    http://www.freescale.com/files/sensors/doc/app_note/AN1573.pdf (06/25/2009).

14. J. Wilson, "Pressure Measurements: Principles and Practice," The Dynamic Consultant LLC, http://sensorsmag.com/sensors. (06/25/2009).

15. W. E. Knowles Middleton, *The History of the Barometer* (The Johns Hopkins Press, 1964).

16. Vacuum Generators, *Operating and Maintenance Handbook*. MH Series Mechanical Hand. Document Number UI521596

    www.vgscienta.com/_resources/File/Manuals/Transfer/UI521596.pdf. (06/25/2009).

17. Integrated Publishing Archive Service, *Basic Machines- Intro to Machines and Motion Theories*, www.tpub.com/content/engine/14037. (06/25/2009).

18. Efunda Engineering Fundamentals, Hydrostatics: Manometer Example,

    http://www.efunda.com/formulae/fluids/manometer.cfm. (06/25/2009). '

19. K. Peterson, *Silicon as a Mechanical Material*, Proceedings IEEE 70 (1982) pp 420-457.

20. W. P. Eaton and J. H. Smith, "Micromachined Pressure Sensor: review and recent developments," Smart Materials and Structures 6, 530-539 (1997).

21. L. F. Fuller. *Bulk Micromachined Pressure Sensor*, Proceedings of the 15th Biennial University/Government/Industry Microelectronics Symposium. (2003) pp 317-320.

22. K. Benaissa, A. Nathan, "IC Compatible Optomechanical Pressure Sensor Using Mach-Zehnder Interferometry," IEEE Trans. Electron Devices 43, 9, 1571-1582 (1996).

23. C. Gorecki, L. Nieradko, A. Sabac, M. Jozwik, *Optomechanical Sensor Based on the Combination of Integrated Optics and MEMS*, Proceeding of the Symposium on Photonics Technologies for 7th Framework Program (2006) pp 178-182.

24. J.Xu, G. Pickrell, X.Wang, W. Peng, K. Cooper, A. Wang, " A Novel Temperature-Insensitive Optical Fiber Pressure Sensor for Harsh Environments," IEEE Photonics Tech. Letter 4, 870-877 (2005).

25. S. Timoshenko and S. Woinowsky-Krieger, *Theory of Plates and Shells* (McGraw-Hill, 1959).

26. Mario Di Giovanni, *Flat and Corrugated Diaphragm Design Handbook* (Marcel Dekker, Inc., 1982).

27. E. Ventsel and T. Krauthammer, *Thin Plates and Shells. Theory, Analysis, and Applications* (Marcel Dekker, Inc, 2001).

28. W. P. Eaton, F. Bitsie, J. H. Smith, D.W. Plummer, *A New Analytical Solution for Diaphragm Deflection and its Application to a Surface-Micromachined Pressure Sensor*, Technical Proceedings of the International Conference on Modeling and Simulation of Microsystems (1999).

29. S. M. Sze, *Semiconductor Sensors* (John Wiley & Son, Inc., 1994).

30. Kulite Semiconductor Products, Inc., *Pressure Transducer Handbook*,

    http://www.kulite.com/techinfo.asp (07/10/2009)

31. W. Altmann, Practical Process Control for Engineers and Technicians (Newnes, 2005).

32. S. Sugiyama, M. Takigawa, and I. Igarashi, "Integrated Piezoresistive Pressure Sensor with Both Voltage and Frequency Output," Sensors and Actuators A 4, 113-120. (1983).

33. C. S. Smith, "Piesoresistance Effect in Germanium and Silicon," Physical Review 94, 1, 42-49 (1954).

34. J. Bryzek , K. Petersen, J.R. Mallon, L. Christel and F. Pourahmadi , *Silicon Sensors and Microstructures,* Proceedings of Electro International Conference (1990) pp 661-665.

35. E.R. Peake , A.R. Zias and J.V. Egan," Solid-State digital pressure transducer," IEEE Trans. Electron Devices 16, 870–6 (1969).

36. K. D. Wise, and J. B. Angell, "An IC Piezoresistive Pressure Sensor for Biomedical Instrumentation," IEEE Transaction on Biomedical Engineering BME-20, 2, 101–109 (1973).

37. A. C. M. Gieles and G. H. J. Somers, "Miniature Pressure Transducers with a Silicon Diaphragm," Philips Tech. Rev. 33 14–20 (1973).

38. J. M. Borky and K. D Wise, "Integrated Signal Conditioning for Silicon Pressure Sensors," IEEE Trans. Electron Devices 26, 1906–10 (1979).

39. S. K Clark. and K. D. Wise, "Pressure Sensitivity in Anisotropically Etched Thin-Diaphragm Pressure Sensors," IEEE Trans. Electron Devices 26, 1887–1896 (1979).

40. W. H. Ko, J. Hynecek and S. F. Boettcher, "Development of a Miniature Pressure Transducer for Biomediclal Applications," IEEE Trans. Electron Devices 26, 1896–1905 (1979).

41. R. B. Hood. *Sensors, Displays, and Signal Conditioning,* Conference on Automotive Electronics (Detroit, MI, Feb.1974).

42. D. S. Eddy and D. R. Sparks. *Application of MEMS Technology in Automotive Sensors and Actuators.,* Proceeding of the IEEE 86, 8, 1747-1755 (1998).

43. S. Aravamudhan, S. Bhansali, "Reinforced Piezoresistive Pressure Sensor for Ocean Depth Measurements," Sensors and Actuators A: Physical 142, 1, 111-117 (2008).

44. Kulite Semiconductor Products . Inc. Leonia NJ, 2009. http://www.kulite.com (08/02/2009).

45. S. Marco, "High-Performance Piezoresistive Pressure Sensors for Biomedical Applications Using Very Thin Structured Membranes," Meas. Sci. Technol. 7, 9, 1195-1203 (1996).

46. M. Z. Shaikh, S. F. Kodad, B.C. Jinaga, "Performance Analysis of Piezoresistive MEMS for Pressure Measurement, " Journal of Theoretical and Applied Information Technology 4, 3, 227-231 (2008).

47. B. Bae, K. Park, and M. A. Shannon, "Low-Pressure Treatment Control of Glaucoma Using an Electromagnetic Valve Actuator with a Piezoresistive Pressure Sensor," Microtechnology in Medicine and Biology, 3rd IEEE/EMBS, 126-129 (2005).

48. W. D. Callister, Jr, *Materials Science and Engineering: An Introduction. USA* (John Wiley and Sons, 1985).

49. N. Maluf and K. Willians, *An Introduction to Microelectromechanical System Engineering*, 2nd ed. (Artech House, Inc, 2004), pp 15-92.

50. M. Hendriks, R. Delhez, T. H. de Keijser, S. Radelaar, F. H. P. M. Habraken, A. E. T. Kuiper and P. R. Boudewijn, "X-Ray Diffraction Study and Electrical Characterization of Boron Implanted Low-Pressure Chemical Vapor Deposited Polycrystalline Silicon Layers," Journal of Applied Physics 56, 2751-2761 (1984).

51. V. Mosser, J. Suski, J. Goss and E. Obermeier, "Piezoresistive Pressure Sensors Based on Polycrystalline Silicon," Sensors and Actuators A-Physical 28, 113-132 (1991).

52. M. M. Mandurah, K. C. Saraswat, and T. I. Kamins, "Model of Conduction in Polycrystalline Silicon, Theory and Comparison of Theory and Experiment," IEEE Transactions on Electron Devices 28, 10, 1163 – 1176 (1981).

53. N. M. Ravindra, Studies of Some Applied Aspeces of Semiconductors Including Those Relevant to Solar Cells and Infra-Red Detectors. Ph. D. Dissertation, Department of Physics University of Roorkee, India, July 1981).

54. J. Y. W. Seto,"The Electrical Properties of Polycrystalline Silicon Films," Journal of Applied Physics 46, 5247-5254 (1975).

55. J. Fraden. *AIP Handbook of Modern Sensor: Physics, Design and Application* (American Institute of Physics, 1993).

56. G. K. Johns, "Modeling Piezoresistivity in Silicon and Polysilicon," Journal of Applied Engineering Mathematics 2 (2006).

57. J. F. Nye, *Physical Properties of Crystals* (Oxford University Press, 1985).

58. S. Durand and C. Tellier, "Linear and Non-Linear Piezoresistance Coefficients in Cubic Semiconductors," J. Phys. III France, 6, 237–266 (1996).

59. Conyers Herring and Erich Vogi, "Transport and Deformation-Potential Theory for Many-Valley Semiconductor with Anisotropic Scattering," Physical Review 101, 3, 944-961 (1956).

60. J. Richter, J. Pedersen, M. Brandbyge, E. V. Thomsen, and O. Hansen, "Piezoresistance in p-Type Silicon Revisited," Journal of Applied Physics 104, 023715, 1-8 (2008).

61. Y. Ohmura, "Numerical Study of the Piezoresistance Effect in p-Type Si," J. Phys. Soc. Jpn. 61, 217-226 (1992).

62. S. I. Kozlovskiy, V. V. Nedostup, and I. I. Boiko, " First-Order Piezoresistance Coefficients in Heavily Doped p-type Silicon Crystals," Sens. and Actuators A 133, Issue 1, 72-81 (2007).

63. G.L. Bir, G.E. Pikus Symmetry and Strain-Induced Effects in Semiconductors (New York, 1974) pp 9-290.

64. K. Suzuki, H. Hasegawa and Y. Kanda, "Origin of the Linear and Nonlinear Piezoresistance Effects in p-Type Silicon," Jpn. J. Appl. Phys. 23, L871-L874 (1984).

65. P. Kleimann, B. Semmache, M. L. Berre, and D. Barbier, "Stress-Dependent Hole Effective Masses and Piezoresistive Properties of p-Type Monocrystalline and Polycrystalline Silicon," Phys. Rev. B 57, 15, 8966-8971 (1998).

66. T. Toriyama, Y. Tanimoto, and S. Sugiyama, "Single Crystal Silicon Nano-Wire Piezoresistors for Mechanical Sensors," J. Microelectromech. Syst. 11, 605–611 (2002).

67. T. R. Kuphaldt, Lessons In Electric Circuits, Volume I – DC., 5th Ed. last update October 18 (2006),

http://www.allaboutcircuits.com/vol_1/chpt_9/7.html (08/01/2009).

68. USGS, Use of Submersible Pressure Transducer in Water-Resources Investigations. Chapter A of Book 8 Instruments for Measurement of Water Level. U. S. Department of the Interior/ U.S. Geological Survey, Reston, Virginia (2004).

69. K. Sivakumar, N. Dasgupta and K.N. Bhat. "Sensitivity Enhancement of Polysilicon Piezo-resistive Pressure Sensors with Phosphorous Diffused Resistors," Journal of Physics: Conference Series 34, 216–221 (2006).

70. A.D. Kurtz, A.A. Ned, and A.H. Epstein, Improved Ruggedized SOI Transducers Operational Above 600°C, Twenty-First Transducer Workshop Lexington, Maryland, June 22-23 (2004).

71. G. Hernandez, Fabry-Perot Interferometers (Cambridge University Press, 1986).

72. J. M. Vaughan, The Fabry-Perot Interferometer. History, Theory, Practice and Applications (Adan Hilger, Bristol and Philadelphia 1989).

73. J. X. Fang, H. F. Taylor, and H. S. Choi, "Fiber-Optic Fabry- Perot Flow Sensor," Microwave and Optical Technology Letters 18, 3, 209-211 (1998).

74. T. K. Gangopadhyay and P. J. Henderson, "Vibration: History and Measurement with an Fabry-Pérot Sensor with Solid-State Laser Interferometry," Appl. Opt. 38, 12, 2471-2477 (1999).

75. N. Sathitanon, and S. Pullteap, "A Fiber Optic Interferometric Sensor for Dynamic Measurement," International Journal of Computer Science and Engineering 2; (2008)

76. M. Singh, C. J. Tuck and G. F. Fernando, "Multiplexed Optical Fibre Fabry–Perot Sensors for Strain Metrology," Smart Mater. Struct. 8, 549–553 (1999).

77. N. Singh , S. C. Jain, A. K. Aggarwal and R. P. Bajpai, "Develop and Experiment Studies of Fibre Optic Extrinsic Fabry-Pérot Interferometric Sensor for Measurement of Strain in Structures, " Current Science 86, 2, 309-314 (2004).

78. H. Singh and J. S. Sirkis. "Simultaneously Measuring Temperature and Strain Using Optical Fiber Microcavities," Journal of Lightwave Technology 15, 4, 647-653 (1997).

79. Z. Huang, W. Peng, J. Xu, G. R. Pickrell, A. Wang, "Fiber Temperature Sensor for High-Pressure Environment," Optical Engineering 44, 10, 104401 (2005).

80. V. R. Machavaram, R. A. Badcock, G. F. Fernando, "Fabrication of intrinsic fibre Fabry–Perot sensors in silica fibres using hydrofluoric acid etching," Sensors and Actuators A 138 , 248–260 (2007).

81. Fabin Shen, UV-Induced Intrinsic Fabry-Perot Interferometric Fiber Sensors and Their Multiplexing for Quasi- Distributed Temperature and Strain Sensing. Ph.D. Dissertation, Virginia Polytechnic Institute and State University (2006).

82. C. E. Lee and H. F. Talyor, "Fiber-Optic Fabry-Perot Temperature Sensor Using a Low-Coherence Light Source," Journal of Lightwave Technology 9, 129 – 134 (1991).

83. C.E Lee, and H.F. Taylor, "Interferometric Optical Fiber Sensors Using Internal Mirrors," Electron. Lett. 24, 4, 193-194 (1988).

84. P. Betts, and J.A. Davis, "Bragg Grating Fabry-Perot Interferometer with Variable Finesse," Opt. Eng. 43, 5, 1258-1259 (2004).

85. F. Shen, *UV-induced intrinsic Fabry-Perot interferometric fiber sensor. Sensors for Harsh Environments.*: Proceedings of SPIE - The International Society for Optical Engineering Sensors for Harsh Environments. Philadelphia, PA, Vol. 5590 (2004).

86. W. Huo, "Contolled Fabrication System of Fabry-Perot Optical Fiber Sensor", M. S. Thesis, Virginia Polytechnic Institute and State University (2000).

87. Y. J. Rao, "Recent progress in fiber-optic extrinsic Fabry–Perot interferometric sensors," Optical Fiber Technology 12, 227–237 (2006).

88. Y. Jiang and C. Tang, "High-Finesse Micro-Lens Fiber-Optic Extrinsic Fabry–Perot Interferometric Sensors," Smart Mater. Struct. 17, 055013 (2008).

89. Z. Wang, Intrinsic Fabry-Perot Interferometric Fiber Sensor Based on Ultra-Short Bragg Gratings for Quasi-Distributed Strain and Temperature Measurements, Ph. D. Dissertation, Virginia Polytechnic Institute and State University (2006).

90. M. Born and E. Wolf, *Principles of Optics*, 7th Edition (expanded) (1999).

91. A. Yariv, *Optical Electronics*, 4th ed. (Saunders College Publishing 1991).

92. K. A. Murphy, M. S. Miller, A. M. Vengsarkar, R. O. Claus, "Elliptical-Core, Two-Mode, Optical Fiber Sensor Implementation Methods," J. Lightwave Tech. 8, 11 (1990).

93. D. Geib, Multiplexing of Extrinsic Fabry-Perot Optical Fiber Sensors for Strain Measurements, M. S. Thesis, Virginia Polytechnic Institute and State University (2003).

94. C. J. Easley, L. A. Legendre, M. G. Roper, T. A. Wavering, J. P. Ferrance, and J. P. Landers, "Extrinsic Fabry–Perot Interferometry for Noncontact Temperature Control of Nanoliter-Volume Enzymatic Reactions in Glass Microchips," Anal. Chem.77, 4, 1038-1045 (2005).

95. R. O. Claus, M. F. Gunther, A. Wang, and K. A. Murphy, "Extrinsic Fabry-Perot sensor for strain and crack opening displacement measurements from -200 to 900C," Smart Materials and Structures 1, 237-242 (1992).

96. K.D. Oh, J. Ranade, V. Arya, A. Wang, and R. O. Claus, "Optical Fiber Fabry–Perot Interferometric Sensor for Magnetic Field Measurement," IEEE Photonics Technology Letter 9, 6 (1997).

97. J. Liu, Yuze Sun, and Xudong Fan, "Highly versatile fiber-based optical Fabry-Pérot gas sensor," Optics Express 2732. Vol. 17, No. 4 (2009).

98. J. Han, D. P. Neikirk, M. Clevenger, and J. T. McDevitt, *Fabrication and characterization of a Fabry-Perot based chemical sensor*, SPIE Microelectronic Structures and MEMS for Optical Processing II, M. E. Motamedi and W. Bailey, editors, Proc. SPIE 2881, Austin, Texas, USA, 14-15, October (1996) pp. 171-178.

99. X. Chen, F. Shen, Z. Wang, Z.Huang, and A. Wang, "Micro-air-gap based intrinsic Fabry–Perot interferometric fiber-optic sensor," Applied Optics 45, 30, 20 (2006).

100. G. C. Hill, R. Melamud, F. E. Declercq, A.A. Davenport, I. H. Chan, P. G. Hartwell, B. L. Pruitt, "SU-8 MEMS Fabry-Perot Pressure Sensor," Sen. Act. A 138, 1, 52-62(2007).

101. J. S. Heo and J. J. Lee, "A micro Total Reflective Extrinsic Fabry-Perot Interferometric Fiber Optic Pressure Senor for medical application," International Journal of Modern Physics B 17, 8 &9, 1199-1204 (2003).

102. D. Towers, A. McCartney, M. Bialkowski, B. James, L. Stewart, C. Towers, W. MacPherson, and R. Reuben, Fiber Pressure Sensors Find Application in Urology, SPIE Newsroom, DOI: 10.1117/2.1200610.0445, (2006).

103. M. Han, X.Wang, J. Xu, K. L. Cooper, A. Wang, "Diaphragm-based extrinsic Fabry-Perot interferometric optical fiber sensor for acoustic wave detection under high background pressure," Optical Engineering 44, 6 (2005).

104. B. Yu, D. Woong Kin, J. Deng, H. Xiao, and A. Wang, " Fiber Fabry-Perot Sensor for Detection of Partial Discharges in Power Transformers," Applied Optics 42, 16 (2003).

105. J. Deng. Development of Novel Optical Fiber Interferometric Sensors with High Sensitivity for Acoustic Emission Detection, Ph. D. Dissertation ,Virginia Polytechnic Institute and State University (2004).

106. Y. Sun, G. Feng, G. Georgiou, E. Niver, K. Noe, and K. Chin, " Fabry-Perot Diaphragm Fiber Optic Sensor (DFOS) for Acoustic Detection," Sensor and Transducer Journal, Special Issue, 76-83 (2007).

107. P. M. Nieva1, N. E. McGruer, and G. G. Adams., "Design and characterization of a micromachined Fabry–Perot vibration sensor for high-temperature applications," Journal of Micromechanics and Microengineering. 16, 2618–2631(2006).

108. J. A. Greene, K. A. Murphy, B. R. Fogg, R. O. Claus, A. M. Vengsarkar, "Optical fiber, vibration mode filters incorporating photoinduced refractive index gratings," Smart Materials and Structures, 1 (1992).

109. J. Xu, A Novel Temperature-Insensitive Optical Fiber Pressure Sensor for Harsh Environments, Ph. D. Dissertation submitted to the Faculty of Virginia Polytechnic Institute and State University, (2004).

110. S. Prasnna, S. M. Nagaraja, P. Pandojirao-Sunkojirao, J. C. Chiao, *Modeling and Design of a Fiber Optic Pressure Senor*, VII International Conference on Micro Electro Mechanical System, Sep. 21-22, El Paso Texas. (2005).

111. Y. Kim and D. P. Neikirk, "Micromachined Fabry-Perot Cavity Pressure Transducer," IEEE Photonics Technology Letters 7, 1471-1473 (1995).

112. W.J. Wang, R.M. Lin, T.T. Sun, D.G. Guo, Y. Ren, " Performance-enhanced Fabry–Perot microcavity structure with a novel non-planar diaphragm," Microelectronic Engineering 70, 102–108 (2003).

113. W. J. Wang, D. G. Guo, R M Lin and XWWang, "A single-chip diaphragm-type miniature Fabry–Perot pressure sensor with improved cross-sensitivity to temperature," Measurement Science and Technology, 15, 905–910 (2004).

114. I. Padron, A. Fiory and N. M. Ravindra, "Integrated Electronic and Optical MEMS Based Sensors" NJIT Case number 07-068.

115. I. Padron, A.Fiory and N. M. Ravindra, *Introduction of Embossed Diaphragm as Sensing Element of an Integrated Optical and Electronic Sensor*, Proceedings of the Materials Science and Technology 2009 Conference. Pittsburgh, PA (2009).

116. I. Padron, A. T. Fiory and N. M. Ravindra, "Novel MEMS Fabry-Perot Interferometric Pressure Sensors," Materials Science Forum, Trans Tech Publications, Switzerland 638-642, 1009-1014 (2010).

117. K. K. Chin, Y. Sun, G. Feng, G. E. Georgiou, K. Guo, E. Niver, H. Roman, and K. Noe, "Fabry-Perot Diaphragm Fiber-Optic Sensor," Applied Optics 46, 31 (2007).

118. D. Guo, R. Lin, and W. Wang, "Gaussian-Optics-Based Optical Modeling and Characterization of a Fabry-Perot Microcavity for Sensing Applications," Optical Society of America A 22, 8 (2005).

119. K. K. Chin, "Interference of Fiber-Coupler Gaussian Beam Multiply Reflected Between Two Planar Interfaces," IEEE Photonics Technology Letters 19, 20 (2007).

120. Genplot, Computer Graphics Service (Lansing, NY 14882)